

**MEASUREMENT OF MULTIJET CROSS-SECTION RATIOS
IN PROTON-PROTON COLLISIONS WITH THE
CMS DETECTOR AT THE LHC**

A THESIS

Submitted to the
FACULTY OF SCIENCE
PANJAB UNIVERSITY, CHANDIGARH
for the degree of

DOCTOR OF PHILOSOPHY

2018

Anterpreet Kaur

DEPARTMENT OF PHYSICS
CENTRE OF ADVANCED STUDY IN PHYSICS
PANJAB UNIVERSITY, CHANDIGARH
INDIA

*Dedicated to
my Parents*

Acknowledgement

I would like to take this opportunity to thank the many people who helped make this dissertation possible.

In the first and foremost place, I gratefully express my sincere gratitude to my supervisor Prof.(Mrs.) Manjit Kaur for her invaluable assistance, support, guidance and blessings. She inspired me greatly to work in this project. Her willingness to motivate me contributed tremendously to this project.

I am highly obliged to Prof. C.S. Aulakh Chairperson of the Department of Physics, Panjab University, Chandigarh, for his helping hand in providing a good environment and adequate facilities to complete this project successfully.

I feel deeply indebted to my parents for their unconditional love, understanding, support, strength, blessings and for everything.

I am greatly thankful to my wellwishers, my friends Anu, Sohail, Junaid, Man-deep and my classmates for all that they meant to me during the crucial times of the completion of my project.

I owe my very special thanks to Mr. Inderpal Singh, Mrs. Prabhdeep Kaur, Mrs. Manuk Z. Mehta, Ms. Ritu Aggarwal, Ms. Ruchi Gupta, Ms. Monika Mittal and Ms. Genius, the members of high energy physics Laboratory, Dept. of Physics, P.U. for helping me out from all kinds of problems with their constant support, suggestions and encouragement.

Finally and the most importantly, I would like to pay my greatest regards to the Almighty God for His blessings and kindness, a boundless and an endless source of inspiration for me always.

Abstract

High-energy collisions in particle physics experiments produce complex events with large number of particles. An approach to the analysis of these events involves a clustering procedure known as the jet finder algorithm to identify the clusters of particles called jets. The dominant process in Quantum Chromodynamics (QCD) is jet production by scattering of the elementary quark and gluon constituents of the incoming hadron beams. These jets have a direct connection with the underlying particle physics reaction. Understanding jet structure is the motivation for the present analysis.

A measurement of inclusive multijet event cross-sections is presented from proton-proton collisions recorded at $\sqrt{s} = 8\text{ TeV}$ with the CMS detector and corresponding to an integrated luminosity of 19.7 fb^{-1} . Jets are reconstructed with the anti- k_t clustering algorithm for a jet size parameter $R = 0.7$ in a phase space region ranging up to jet transverse momenta p_T of 2.0 TeV and an absolute rapidity of $|y| = 2.5$. The inclusive 2-jet and 3-jet event cross-sections are measured as a function of the average p_T of the two leading jets. The data are well described by predictions at next-to-leading order in perturbative quantum chromodynamics and additionally are compared to several Monte Carlo event generators. The strong coupling constant at the scale of the Z boson mass is inferred from a fit of the ratio of the 3-jet over 2-jet event cross-section giving $\alpha_s(M_Z) = 0.1150 \pm 0.0010 (\text{exp}) \pm 0.0013 (\text{PDF}) \pm 0.0015 (\text{NP})^{+0.0050}_{-0.0000} (\text{scale})$.

Contents

1	Introduction	1
2	Theory	2
3	Experimental Apparatus	3
4	Measurement of the Differential Inclusive Multijet Cross-sections and their Ratio	4
4.1	Data Samples	5
4.1.1	Monte Carlo Samples	6
4.2	Event Selection	7
4.2.1	Trigger Selection	7
4.2.2	Primary Vertex Selection	9
4.2.3	Missing Transverse Energy	11
4.2.4	Jet Identification	11
4.2.4.1	Jet ID Efficiency	12
4.2.5	Jet Selection	16
4.3	Comparison with Simulation	16
4.3.1	Pile-up Reweighting	16
4.3.2	Comparison of Cross-sections and their Ratio	17

4.4	Jet Energy Resolution (JER)	19
4.5	Unfolding	25
4.5.1	Response Matrices	26
4.5.1.1	Inclusive Cross-sections	27
4.5.1.2	Cross-section Ratio, R_{32}	30
4.5.2	Closure Test	30
4.5.3	Unfolding of the Measurement	32
4.6	Experimental Uncertainties	33
4.6.1	Statistical Uncertainty	35
4.6.2	Jet Energy Corrections Uncertainty	35
4.6.3	Unfolding Uncertainty	39
4.6.4	Luminosity Measurement Uncertainty	40
4.6.5	Residual Uncertainty	40
4.6.6	Total Experimental Uncertainty	41
5	Theoretical Calculations	43
5.1	Fixed Order NLO Calculations	43
5.1.1	NLO Correction Factors	45
5.1.2	Non-Perturbative Corrections	46
5.1.3	Electroweak Corrections	48
5.2	Theoretical Uncertainties	50
5.2.1	Scale Uncertainty	50
5.2.2	PDF Uncertainty	51
5.2.3	Non-perturbative Uncertainty	52
5.2.4	Total Theoretical Uncertainty	52
5.3	Comparison of Theory to Data	54

6	Determination of the Strong Coupling Constant	59
6.1	Sensitivity of Measurements to $\alpha_s(M_Z)$	60
6.2	Determination of $\alpha_s(M_Z)$	61
6.2.1	Fitting Procedure	61
6.2.2	Fit Results	67
6.3	Running of the Strong Coupling Constant	70
7	Summary	74
	Appendix A	77
A.1	Cross-section Ratio, R_{32}	78
A.2	Individual Sources of Jet Energy Correction Uncertainties	79
A.3	Experimental Uncertainties	82
A.4	Theoretical Uncertainties	85
	Bibliography	88
	Reprints	95

Chapter 1

Introduction

[Chapter 2](#) [Chapter 3](#) [Chapter 4](#) [Chapter 5](#) [Chapter 6](#) [Chapter 7](#)

Chapter 2

Theory

Chapter 3

Experimental Apparatus

Chapter 4

Measurement of the Differential Inclusive Multijet Cross-sections and their Ratio

The inclusive differential jet event cross-sections are studied as a function of the average transverse momentum, $H_{T,2}/2 = \frac{1}{2}(p_{T,1} + p_{T,2})$, where $p_{T,1}$ and $p_{T,2}$ denote the transverse momenta of the two leading jets, and are defined by :

$$\frac{d\sigma}{d(H_{T,2}/2)} = \frac{1}{\epsilon \mathcal{L}_{\text{int,eff}}} \frac{N_{\text{event}}}{\Delta(H_{T,2}/2)} \quad (4.1)$$

where N_{event} is the number of inclusive n-jet events counted in an $H_{T,2}/2$ bin, ϵ is the product of the trigger and jet selection efficiencies, which are greater than 99%, $\mathcal{L}_{\text{int,eff}}$ is the effective integrated luminosity, and $\Delta(H_{T,2}/2)$ are the bin widths. The measurements are reported in units of (pb/GeV). The inclusive n-jet event samples include the events with number of jets $\geq n$, where $n = 2$ and 3 in the current study.

The cross-section ratio R_{32} , defined in Eq. 4.2 is obtained by dividing the differential cross-sections of inclusive 3-jet events to that of inclusive 2-jet one, for

each bin in $H_{T,2}/2$.

$$R_{32} = \frac{\frac{d\sigma_{3-jet}}{d(H_{T,2}/2)}}{\frac{d\sigma_{2-jet}}{d(H_{T,2}/2)}} \quad (4.2)$$

For inclusive 2-jet events ($n_j \geq 2$) sufficient data are available up to $H_{T,2}/2 = 2000$ GeV, while for inclusive 3-jet events ($n_j \geq 3$) and the ratio R_{32} , the accessible range in $H_{T,2}/2$ is limited to $H_{T,2}/2 < 1680$ GeV.

4.1 Data Samples

This measurement uses the data which was collected at the centre-of-mass energy of 8 TeV by CMS experiment in the 2012 run period of the LHC. The 2012 data is taken in four periods A, B, C, D and the data sets are divided into samples according to the run period. Further each sample is grouped into subsets based on the trigger decision. For run B-D, the **JetMon** stream datasets contain prescaled low trigger threshold paths (HLTPFJet40, 80, 140, 200 and 260) while the **JetHT** stream datasets contain unprescaled high threshold trigger paths (HLT PFJet320 and 400). For run A, the **Jet** stream contains all the above mentioned trigger paths. The data to be used in physics analysis must satisfy a certain criteria according to which it should fulfill the validation requirements of data quality monitoring procedure. CMS uses JSON (Java Script Object Notation) format files to store the range of good lumi sections within a run. In the current analysis, the applied certification file¹ is based on the final event reconstruction of the 2012 CMS data sets. The datasets used in the current study are mentioned in the Table 4.1 along with the luminosity of each dataset.

The data sets have the LHC luminosity increasing with period, full data sample of 2012 corresponds to an integrated luminosity of 19.71 fb^{-1} .

¹Cert_190456-208686_8TeV_22Jan2013ReReco_Collisions12.JSON

Table 4.1: Run range and luminosity of the proton-proton collisions data collected at the centre-of-mass energy of 8 TeV by CMS experiment in the year of 2012 in four different run periods A, B, C and D.

Run	Run range	Data set	Luminosity fb^{-1}
A	190456-193621	/Jet/Run2012A-22Jan2013-v1/AOD	0.88
B	193834-196531	/Jet[Mon,HT]/Run2012B-22Jan2013-v1/AOD	4.41
C	198022-203742	/Jet[Mon,HT]/Run2012C-22Jan2013-v1/AOD	7.06
D	203777-208686	/Jet[Mon,HT]/Run2012D-22Jan2013-v1/AOD	7.37

4.1.1 Monte Carlo Samples

To have a comparison of data results with the simulated events, the MADGRAPH5 [1] Monte-Carlo (MC) event generator has been used. The MADGRAPH5 generates matrix elements for High Energy Physics processes, such as decays and $2 \rightarrow n$ scatterings. It has been interfaced to PYTHIA6 [2] by the LHE event record [3], to generate the rest of the higher-order effects using the Parton Showering (PS) model, with tune Z2* to model the underlying event. Matching algorithms make sure that there is no double-counting between the tree-level and the PS-model-generated partons. The MC samples are processed through the complete CMS detector simulation to allow studies of the detector response and compare to measured data on detector level.

The cross-section measured as a function of the transverse momentum p_T or the scalar sum of the transverse momentum of all jets H_T falls steeply with the increasing p_T . So in the reasonable time, it is not possible to generate a large number of high p_T events. Hence, the events are generated in the different phase-space region binned in H_T or the leading jet p_T . Later on, the different phase-space regions are added together in the data analyses by taking into account the cross-section of the different phase-space regions. The official CMS MADGRAPH5+PYTHIA6 (MG5+P6) MC samples used in this analysis are generated as slices in the H_T phase-space are tabulated in Table 4.2 along with their cross-sections and number of events generated.

Table 4.2: The official Monte Carlo samples are produced in phase space slices in H_T with the generator MADGRAPH5 and interfaced to PYTHIA6 for the parton shower and motorization of the events. The cross-section and number of events generated are mentioned for each sample.

Generator	Sample	Events	Cross-section pb
MADGRAPH5 + PYTHIA6	/QCD_HT-100To250_TuneZ2star_8TeV-madgraph-pythia6/ Summer12_DR53X-PU_S10-START53_V7A-v1/AODSIM	50129518	1.036×10^7
	/QCD_HT-250To500_TuneZ2star_8TeV-madgraph-pythia6/ Summer12_DR53X-PU_S10-START53_V7A-v1/AODSIM	27062078	2.760×10^5
	/QCD_HT-500To1000_TuneZ2star_8TeV-madgraph-pythia6/ Summer12_DR53X-PU_S10-START53_V7A-v1/AODSIM	30599292	8.426×10^3
	/QCD_HT-1000ToInf_TuneZ2star_8TeV-madgraph-pythia6/ Summer12_DR53X-PU_S10-START53_V7A-v1/AODSIM	13843863	2.040×10^2

4.2 Event Selection

The events are selected according to several quality criteria which ensures the high purity and high selection efficiency of the sample to be studied. This event selection also reduces beam induced background, detector-level noise and jets arising from fake calorimeter energy deposits.

4.2.1 Trigger Selection

CMS implements a two-level trigger system to reduce the amount of recorded events to a sustainable rate. In this analysis the jets are the final objects to study. So single jet trigger paths with varying thresholds are used to select events in data. It consists of one L1 trigger seed and multiple HLT filters. The L1 jet trigger uses transverse energy sums computed using both HCAL and ECAL in the central region ($|\eta| < 3.0$) or HF in the forward region ($|\eta| > 3.0$). The single jet triggers (HLT_PFJetX) used for the current study are tabulated in Table 4.3. A single jet trigger selects an event in which at least one jet has the transverse momentum above the threshold. HLT_PFJetX implies that there is at-least one jet in the event, whose $p_T > X$ (GeV). The L1 trigger has a lower threshold to ensure full efficiency versus p_T of the HLT trigger. The p_T spectrum is steeply falling and hence the rates for low- p_T jets are very high. So it is not feasible to use a single unprescaled trigger for the selection of

all required events. To collect sufficient data in the lower part of the p_T spectrum, different five prescaled low- p_T trigger paths, each with different prescale value, are used. Also, one unprescaled trigger i.e. HLT_Jet320 is used in the high p_T region, in which the rate is sufficiently small to collect and store all events. During the reconstruction of the spectrum, the prescales have been taken into the account.

Table 4.3: The single jet trigger paths used in the analysis are listed here. The column $H_{T,2}/2$, 99% indicates the value of $H_{T,2}/2$ at which each trigger exhibits an efficiency larger than 99%. The last column gives the effective luminosity seen by each trigger which divided by the total integrated luminosity of 19.71 fb^{-1} , gives the effective prescale applied on a trigger over the whole run period.

Trigger Path	L1 threshold GeV	HLT threshold GeV	$H_{T,2}/2$, 99% GeV	Eff. Lumi fb^{-1}
HLT_PFJet80	36	80	120.0	0.0021
HLT_PFJet140	68	140	187.5	0.056
HLT_PFJet200	92	200	262.5	0.26
HLT_PFJet260	128	260	345.0	1.06
HLT_PFJet320	128	320	405.0	19.71

The efficiency of each trigger path as a function of $H_{T,2}/2$ is described by the turn-on curves with a rising part where the trigger is partly inefficient, until a plateau region where the trigger is fully efficient. Hence it is important to determine the threshold above which a trigger becomes fully efficient. The threshold is the value at which the trigger efficiency exceeds 99%. The trigger efficiency for HLT_PFJetY is given by Eq. 4.3 where HLT_PFJetX is the reference trigger and is assumed to be fully efficient in the considered phase space region. The value of X is chosen previous to that of Y in p_T ordering from the trigger list so that the higher trigger condition can be emulated from the lower trigger path.

$$\epsilon_{\text{HLT_PFJetY}} = \frac{H_{T,2}/2 \left(\text{HLT_PFJetX} + (\text{L1Object_p}_T > Z) + (\text{HLTObject_p}_T > Y) \right)}{H_{T,2}/2(\text{HLT_PFJetX})} \quad (4.3)$$

where Y is the p_T threshold of HLT_PFJetY and Z is the L1 seed value corresponding

to the trigger path HLT_PFJetY. The denominator represents the number of events for which the reference trigger path HLT_PFJetX has been fired. The numerator is the number of events for which HLT_PFJetX has been fired along the p_T of L1Object $\geq Z$ and the p_T of HLTOBJECT $\geq Y$. For example, to obtain turn-on curve for HLT_PFJet260, HLT_PFJet200 is the reference HLT path. The p_T cut on L1Object is 128 GeV and p_T cut on HLTOBJECT is 260 GeV. The threshold point at which the trigger efficiency is larger than 99% is determined by fitting the turn-on distribution with a sigmoid function described in Eq. 4.4. The trigger turn-on curves as a function of $H_{T,2}/2$ can be seen in Fig. 4.1 which are described by a sigmoid function (blue line). The error bars give the uncertainty on the efficiency which is calculated using Clopper-Pearson confidence intervals [4].

$$f_{fit}(x) = \frac{1}{2} \left(1 + \operatorname{erf} \left(\frac{x - \mu}{\sqrt{2}\sigma} \right) \right) \quad (4.4)$$

4.2.2 Primary Vertex Selection

The reconstructed tracks, selected based on the transverse impact parameter significance with respect to the beam line, number of strip and pixel hits and the normalized track χ^2 , identify the primary vertex (PV). The tracks are clustered according to the z-coordinate of their point of closest approach to the beam axis. A selection criteria for primary vertex should be followed which helps to identify and reject the beam background events. At-least one good primary vertex reconstructed from at least four tracks within a distance of $|z(PV)| < 24$ cm to the nominal interaction point in a collision, is required in each event. The radial distance in x-y plane, $\rho(PV)$ should be not be greater than 2 cm. The number of degrees of freedom in fitting for the position of each vertex using its associated tracks should be at-least four in number.

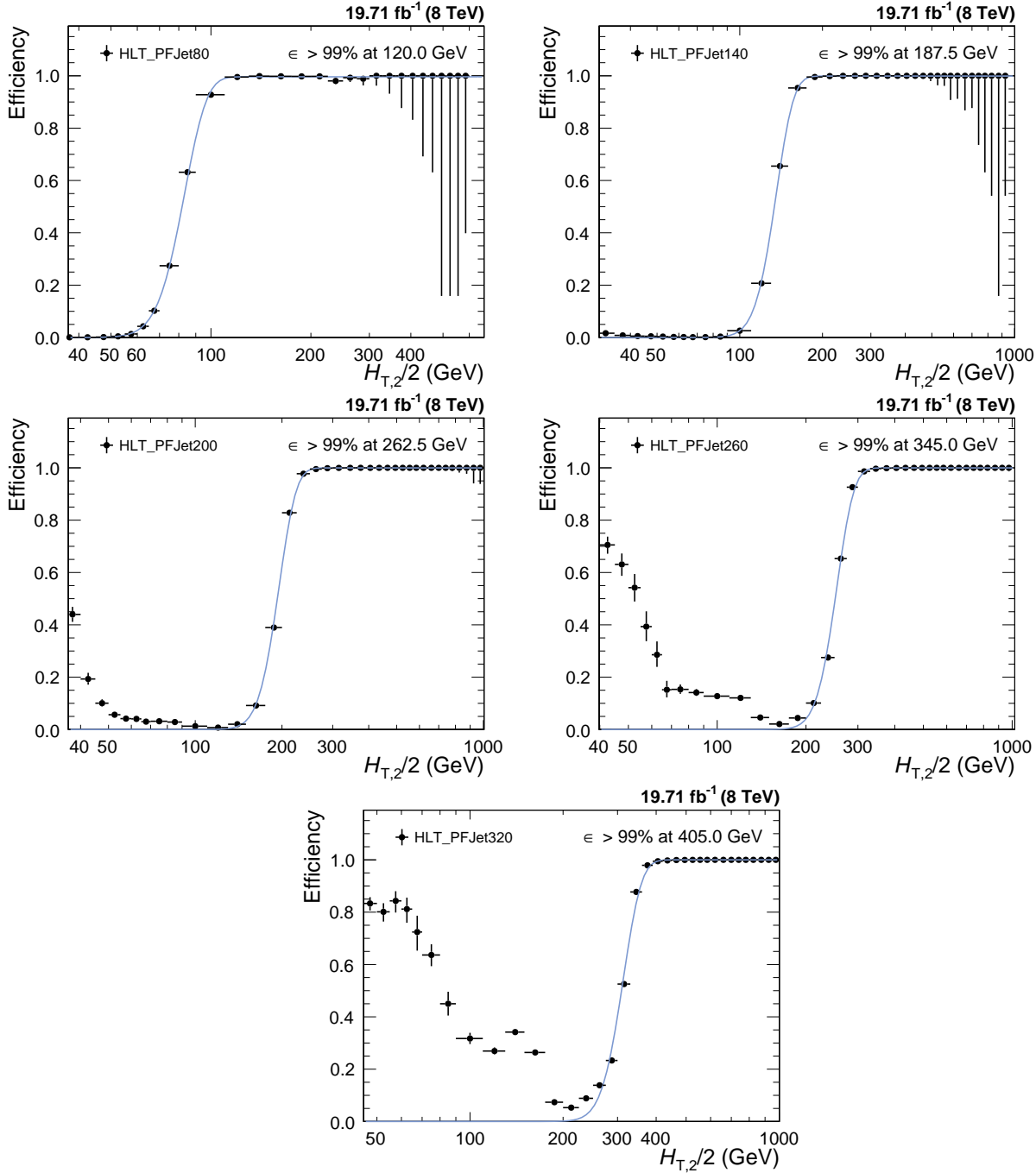


Figure 4.1: Trigger efficiencies turn-on curves for the single jet trigger paths are fitted with a sigmoid function (blue line) to obtain the 99% efficiency threshold. The error bars give the uncertainty on the efficiency which is calculated using Clopper-Pearson confidence intervals [4].

4.2.3 Missing Transverse Energy

In an ideal detector where all particles could be identified and perfectly measured, the transverse momentum of all particles would sum up to zero. But the neutral weakly interacting particles, such as neutrinos, escape from typical collider detectors and do not produce any direct response in the detector elements. The imbalance of total momentum of all visible particles can give the hints of the presence of such particles. The vector momentum imbalance in the plane perpendicular to the beam direction is known as missing transverse momentum or energy (E_T^{miss}). It is one of the most important observables for discriminating leptonic decays of W bosons and top quarks from background events which do not contain neutrinos, such as multijet and Drell–Yan events or searches for physics beyond the Standard Model.

The ratio of missing transverse energy to the total transverse energy $E_T^{\text{miss}}/\sum E_T$, shown in Fig. 4.2 for $n_j \geq 2$ (left) and $n_j \geq 3$ events (right), shows a discrepancy between data (black solid circles) and simulated MC (blue histogram), at the tail part of the distribution. This is because of a finite contribution from $Z(\rightarrow \nu\bar{\nu}) + \text{jet}$ events which gives rise to non-zero E_T in the events in data. Such events are absent in QCD simulated events in MC. Hence $E_T^{\text{miss}}/\sum E_T$ is required to be less than 0.3 to reject events with high E_T^{miss} .

4.2.4 Jet Identification

In order to suppress fake jets, arising from detector noise or misreconstructed particles, jet identification criteria (ID) has been applied. Instead of applying it event-wise, it is applied it on each jet. The algorithm works on reconstructed jets using information of the clustered particle candidates. The official tight jet ID [5], recommended by JETMET group [6] is used. Due to pileup and electronic noise the jet constituent fractions may vary from event to event. In order to reject the noisy jets, some jet selection criteria are optimized to select only good quality jets. The selec-

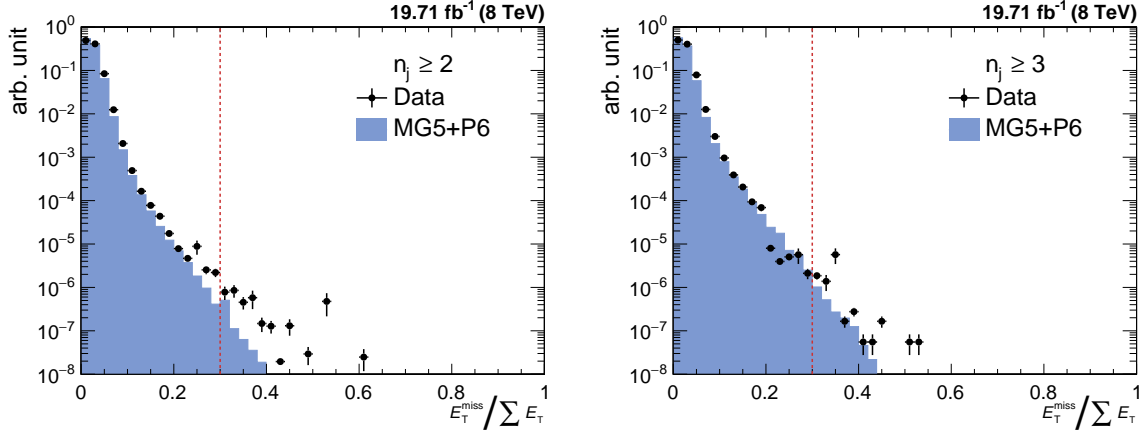


Figure 4.2: Missing transverse energy fraction of the total transverse energy per event in data (black solid circles) and simulated Monte Carlo events (blue histogram) in inclusive 2-jet (left) and 3-jet events (right). To remove background and noise, events with a fraction exceeding a certain threshold, here indicated with the red dashed line, are rejected.

tion criteria are implemented as selection cut on jet fractions. Table 4.4 summarizes the properties of the reconstructed jets and their respective cuts. Each jet should contain at least two particles, one of which should be a charged hadron. The cut on the fraction of neutral hadrons and photons removes HCAL noise and ECAL noise, respectively. Muons that are falsely identified and clustered as jets are removed by the muon fraction criterion. Based on information of the tracker, additional selection cuts are enforced in the region $|\eta| < 2.4$. The charged electromagnetic fraction cut removes the jets clustered from misidentified electrons. Furthermore, the fraction of charged hadrons in the jet must be larger than zero and jets without any charged hadrons are very likely to be pileup jets. The Figs. 4.3 and 4.4 show the distributions of the jet constituents observed in data (black solid circles) and simulated MC events (blue histogram) for $n_j \geq 2$ and $n_j \geq 3$, respectively.

4.2.4.1 Jet ID Efficiency

The efficiency of the jet ID as a function of $H_{T,2}/2$ is studied using a tag-and-probe technique with dijet events. The two leading jets are required to be back-to-back in the azimuthal plane such that $|\Delta\phi - \pi| < 0.3$. One of the dijets is selected randomly

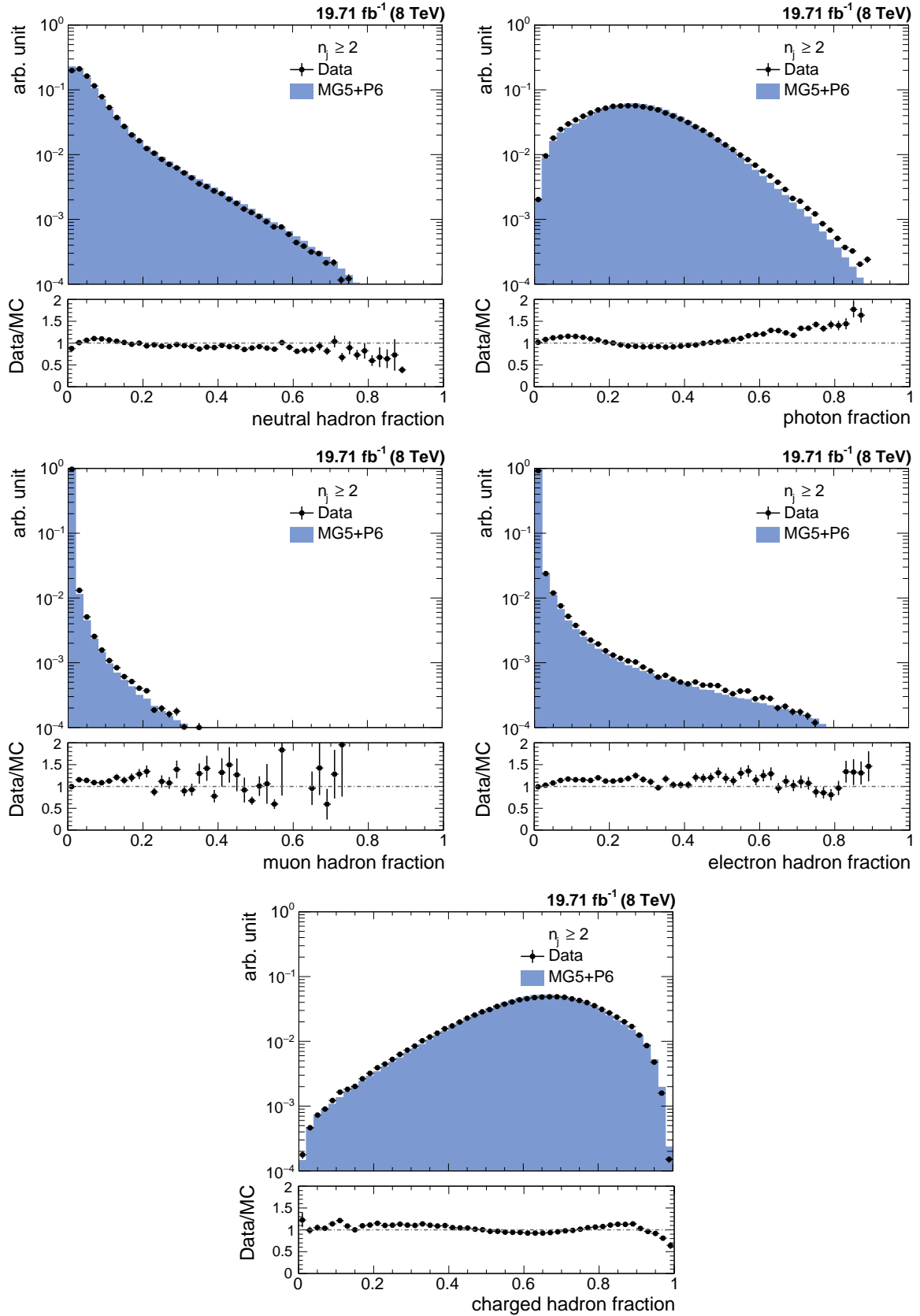


Figure 4.3: The fractions of jet constituents as observed in data (black solid circles) and simulated Monte Carlo events (blue histogram) for different types of PF candidates for inclusive 2-jet events. Data and simulations are normalized to the same number of events. The distributions are shown after the application of the jet ID.

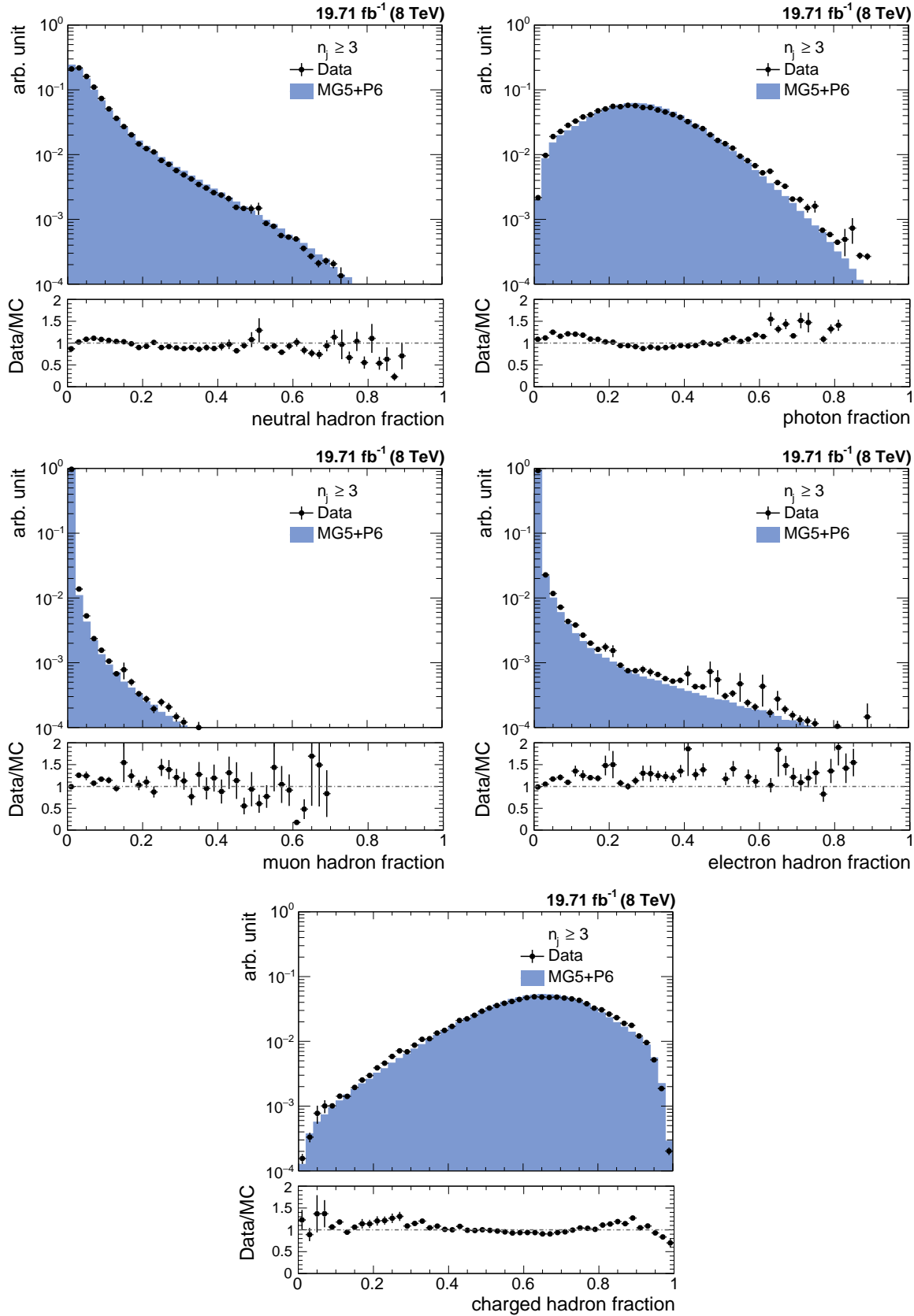


Figure 4.4: The fractions of jet constituents as observed in data (black solid circles) and simulated Monte Carlo events (blue histogram) for different types of PF candidates for inclusive 3-jet events. Data and simulations are normalized to the same number of events. The distributions are shown after the application of the jet ID.

Table 4.4: The jet ID removes noise and fake jets based on the properties of the reconstructed jets and the clustered particle candidates. All the selection cuts which are recommended by the JETMET group are applied [6].

	Property	Loose ID	Tight ID
Whole η region	neutral hadron fraction	< 0.99	< 0.90
	neutral EM fraction	< 0.99	< 0.90
	number of constituents	> 1	> 1
	muon fraction	< 0.80	< 0.80
only $ \eta < 2.4$	charged hadron fraction	> 0	> 0
	charged multiplicity	> 0	> 0
	charged EM fraction	< 0.99	< 0.90

as a “tag” jet which is required to fulfill the tight jet ID criteria. The other jet is called “probe” jet for which it is examined, whether it also passes the tight jet ID. The ID efficiency is defined as the ratio of events where the probe jet passes the ID requirements, over the total number of dijet events. It is shown as function of $H_{T,2}/2$ in Fig. 4.5 and as expected, it is always greater than 99%. The QCD cross-section decreases as a function of $H_{T,2}/2$ and hence the number of events decrease on moving to higher $H_{T,2}/2$. Consequently the statistical fluctuations for ID efficiency are larger at higher $H_{T,2}/2$.

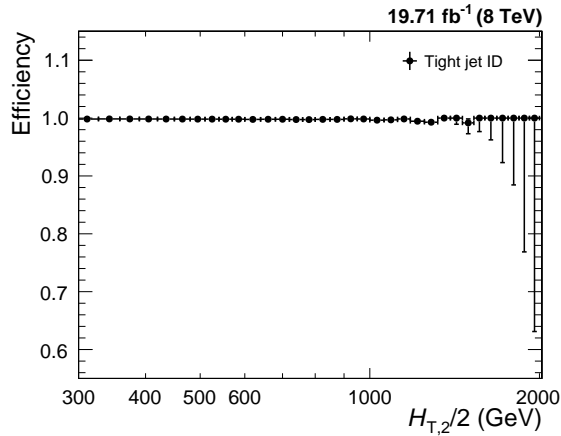


Figure 4.5: The jet ID efficiency is studied as a function of $H_{T,2}/2$ with tag-and-probe technique using dijet event topologies and it always exceeds 99%.

4.2.5 Jet Selection

The measurement of differential cross-sections and their ratio uses jets clustered from particle flow candidates using the anti- k_t jet algorithm with a size parameter, $R = 0.7$. The energy scale of the jets is corrected with the CMS recommended jet energy corrections, described in Sec. [?](#). These corrections are applied to jets in both data² as well those in simulated events³. The jet selection, based on phase space cuts on transverse momentum and rapidity of jets in an event, is as follows :

- All jets having $p_T > 150$ GeV and $|y| < 5.0$ are selected.
- Events with at least two jets are selected.
- The two leading jets should have $|y| < 2.5$ and further jets are counted only, if they lie within the same central rapidity range of $|y| < 2.5$.

These cuts assure high detector acceptance and exactly same selection is applied in the measurement, simulated events as well in theoretical calculations for a consistent comparison.

4.3 Comparison with Simulation

4.3.1 Pile-up Reweighting

While generating the official Monte-Carlo samples, the number of pileup interactions describing the conditions expected for each data-taking period are taken care of. But the number of pile-up events implemented in the simulation $N_{MC}(N_{PU,truth})$, does not match exactly with the one measured actually in data $N_{data}(N_{PU,est.})$. To match the pile-up distributions in data, a reweighting factor w_{PU} , as given by Eq. [4.5](#) is applied

²Winter14_V8 jet energy corrections

³START53_V27 jet energy corrections

to the simulated events. In Fig. 4.6 the number of reconstructed vertices are shown before (left) and after pile-up reweighting (right). It is observed that before pile-up reweighting there was a significant mismatch of the pile-up distributions in data (black solid circles) and simulated MC events (blue histogram), which completely vanishes after reweighting.

$$w_{\text{PU}} = \frac{N_{\text{data}}(N_{\text{PU,est.}}) / \sum N_{\text{data}}}{N_{\text{MC}}(N_{\text{PU,truth}}) / \sum N_{\text{MC}}} \quad (4.5)$$

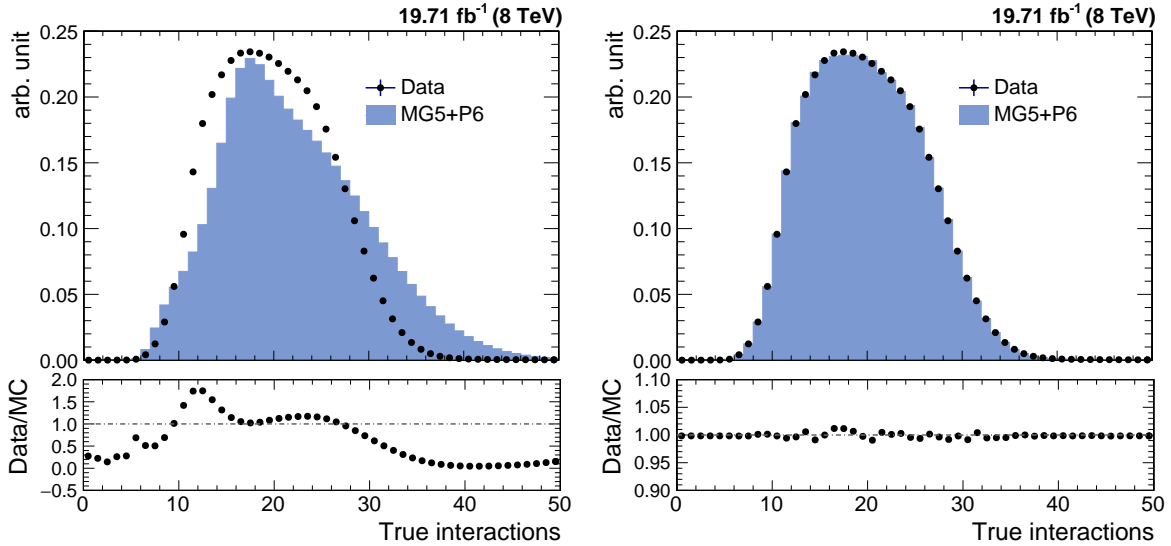


Figure 4.6: Number of reconstructed vertices in data (black solid circles) and simulated Monte Carlo events (blue histogram) before (left) and after (right) the pile-up reweighting.

4.3.2 Comparison of Cross-sections and their Ratio

The measured data distribution of differential cross-section at detector level is compared to the predictions of Monte Carlo simulation using MADGRAPH5 generator interfaced with PYTHIA6 (MG5+P6) including the detector simulation as well as to a fixed-order theory prediction obtained using CT10-NLO PDF set. Figure 4.7 shows the comparison of differential cross-section as a function of $H_{\text{T},2}/2$ for $n_j \geq 2$ (left) and $n_j \geq 3$ events (right), for data (black solid circles), MG5+P6 MC (red empty

circles) and CT10-NLO (blue histogram). The bottom panel in each plot shows the ratio of data to the MC predictions (red line) as well as to the CT10-NLO theory predictions (blue line). The NLO predictions on parton level are not corrected for non-perturbative effects. Still the NLO predictions describe the data better as compared to the LO MC simulations which roughly describes the spectrum on detector level. The sufficient data for $n_j \geq 2$ and $n_j \geq 3$ events are available up to $H_{T,2}/2 = 2000$ GeV and 1680 GeV, respectively. Due to some kinematical constraints, the minimum cut on $H_{T,2}/2$ is 300 GeV (explained in Sec. 5.1.1). Hence the differential cross-sections are studied in the range $300 \text{ GeV} \leq H_{T,2}/2 < 2000$ GeV for $n_j \geq 2$ and $300 \text{ GeV} \leq H_{T,2}/2 < 1680$ GeV for $n_j \geq 3$ events.

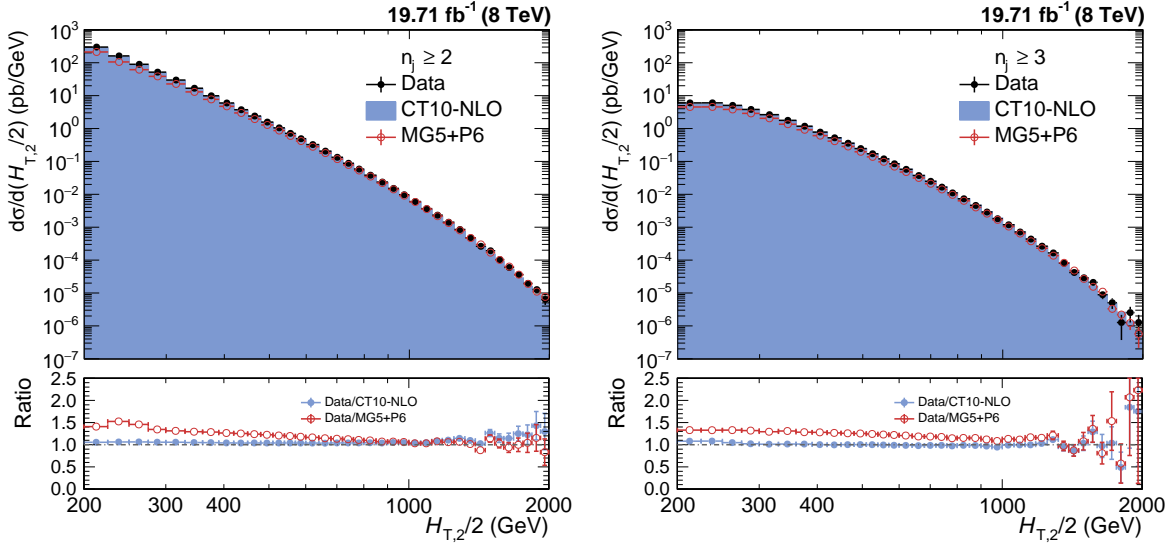


Figure 4.7: The differential cross-sections are compared for data (black solid circles) and LO MADGRAPH5+PYTHIA6 (MG5+P6) Monte Carlo (red empty circles), at reconstructed level with CT10-NLO theory predictions (blue histogram), as a function of $H_{T,2}/2$ for inclusive 2-jet (left) and 3-jet events (right). Ratios of data to the Monte Carlo predictions (red line) as well as to the CT10-NLO predictions (blue line) are shown in bottom panel of each plot.

The ratio of differential cross-sections, R_{32} as a function of $H_{T,2}/2$, is extracted by dividing the cross-section of selected inclusive 3-jet events to that of inclusive 2-jet events at any given bin size of $H_{T,2}/2$. In the cross-section ratios, the numerator and denominator are not independent samples. So to calculate the

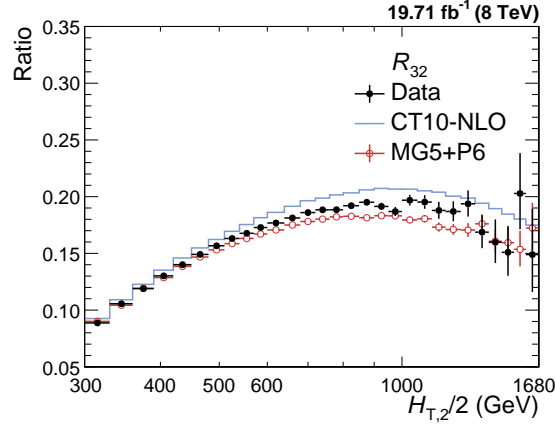


Figure 4.8: Comparison of the cross-section ratio R_{32} as a function of $H_{T,2}/2$, for data (black solid circles) and LO MADGRAPH5+PYTHIA6 (MG5+P6) Monte Carlo (red empty circles), at reconstructed level with CT10-NLO theory predictions (blue line). The error bars give the asymmetrical statistical uncertainty, calculated by the Wilson score interval method which takes into the account the correlation between the numerator and denominator.

statistical uncertainty for the cross-section ratios at reconstructed level, the Wilson score interval method is used which takes into account the correlation between the numerator and the denominator and give asymmetric errors. Figure 4.8 shows the comparison of the cross-section ratio R_{32} as a function of $H_{T,2}/2$, for data (black solid circles) and LO MADGRAPH5+PYTHIA6 (MG5+P6) Monte Carlo (red empty circles), at reconstructed level with CT10-NLO theory predictions (blue line). Since in $n_j \geq 3$ events, the enough statistics for differential cross-section is available upto 1680 GeV of $H_{T,2}/2$ only, R_{32} is also studied in the range $300 \text{ GeV} \leq H_{T,2}/2 < 1680 \text{ GeV}$. The bin-wise inclusive 2-jet and 3-jet events differential cross-sections as well as their ratio R_{32} , calculated at detector level, along with statistical uncertainty (in %) are tabulated in Table A.1.

4.4 Jet Energy Resolution (JER)

In an ideal experiment, the value of a physical quantity would be determined exactly with an infinite precision. For e.g. whenever a particle with energy E passes an ideal calorimeter having infinite resolution, the measured energy should always be equal

to E . But in real world, the measured energy of the above mentioned particle might differ from the value E . This difference of the measured quantity from its true value may be due to detector noise, uncertainties in the calibration, non-linearity of the response etc. Hence this results in the finite value of the resolution of the detector known as jet energy resolution (JER). In such case, the measured values of energy of different particles, passing through the same detector with same energy E , will be different. Such measurements are described by a Gaussian distribution which is centered around the true value of the measured quantity and its width is generally interpreted as detector resolution. Hence the importance of the detector resolution lies in the fact that it indicates how much the measured value of the observable differs from the true one i.e. how precisely a physical observable can be measured. The narrower the distribution, the higher the resolution is and hence the more efficient is the detector.

Due to finite resolution of the CMS detector, the measured transverse momentum of jets gets smeared. Since the observable in this study i.e. $H_{T,2}/2$ is the average sum of transverse momentum of leading and sub-leading jets, the resolution of the detector has to be studied in terms of the observable. CMS detector simulation based on MG5+P6 MC event generators is used to determine the resolution as both the particle and reconstructed level information is available. The jets clustered from stable generator particles called Gen jets as well as from particle flow candidates reconstructed from the simulated detector output called Reco jets, are used. The studies of the JETMET working group at CMS has shown that the jet energy resolution in data is actually worse than in simulation [7]. So the reconstructed jet transverse momentum needs to be smeared additionally to match the resolution in data. Table 4.5 shows the scaling factors (c) which need to be applied on the transverse momentum of simulated reconstructed jets. The scaling factors depend on the absolute η of the jet. The uncertainty on these measured scaling factors ($c_{central}$) needs to be taken into account in a physics analysis. This is done by smearing the reconstructed jets with two additional sets of scaling factors, c_{up}

and c_{down} , that correspond to varying the factors up and down respectively, by one sigma and evaluating the impact of these new sets.

Table 4.5: JETMET working group at CMS has shown that the jet energy resolution in data is actually worse than in simulation [7]. To match the resolution in data, the reconstructed jet transverse momentum in simulated events need to be smeared by applying the scale factors. The uncertainty on the resolution is given by an upwards and downwards variation c_{up} and c_{down} of the measured scaling factor $c_{central}$.

η	0.0 - 0.5	0.5 - 1.1	1.1 - 1.7	1.7 - 2.3	2.3 - 2.8
$c_{central}$	1.079	1.099	1.121	1.208	1.254
c_{down}	1.053	1.071	1.092	1.162	1.192
c_{up}	1.105	1.127	1.150	1.254	1.316

The reconstructed jet p_T is smeared randomly using a Gaussian width widened by the scaling factor ($c_{central}$)

$$p_T \rightarrow Gauss\left(\mu = p_T, \sigma = \sqrt{c_{central}^2 - 1} \cdot JER(p_T)\right) \quad (4.6)$$

where $JER(p_T)$ is the resolution determined as a function of jet p_T using MG5+P6 MC simulated events. After smearing transverse momentum of each reco jet, $H_{T,2}/2$ is calculated from both generator particle jets (Gen $H_{T,2}/2$) as well as the particle flow or reconstructed jets (Reco $H_{T,2}/2$). Then the response is calculated as defined in the Eq. 4.7.

$$R = \frac{\text{Reco } H_{T,2}/2}{\text{Gen } H_{T,2}/2} \quad (4.7)$$

The width of the response distribution in a given Gen $H_{T,2}/2$ bin is interpreted as the resolution which in good approximation can be described by the σ of a Gaussian fit of the response distribution. A double-sided Crystal-Ball function takes into account the non-Gaussian tails of the jet response distribution. The resolution as a function of $H_{T,2}/2$ is calculated separately for both $n_j \geq 2$ and $n_j \geq 3$ events.

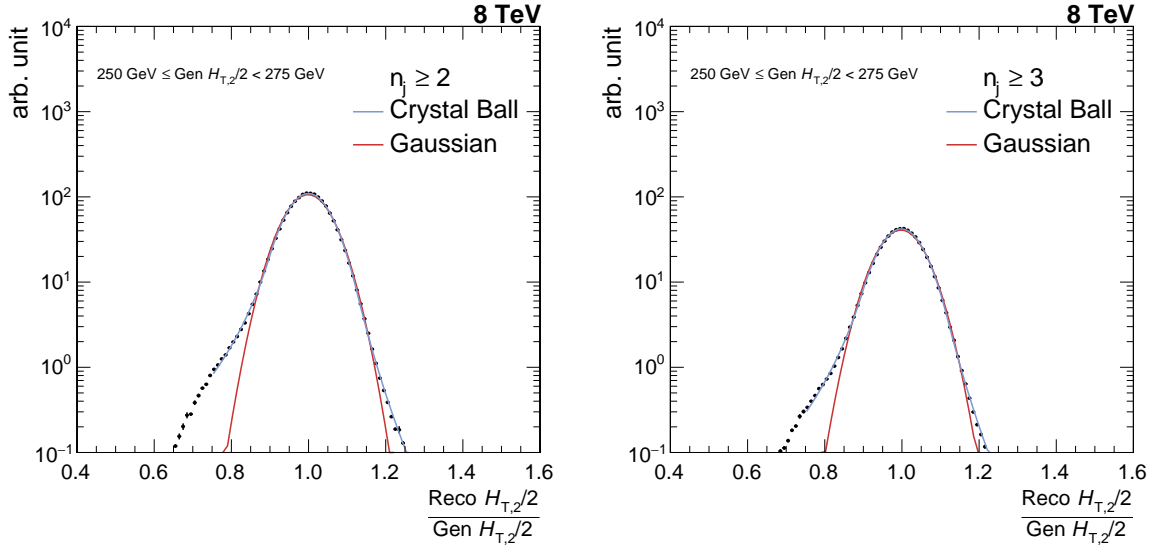


Figure 4.9: Fitting of the resolution distribution, obtained using LO MADGRAPH5+PYTHIA6 (MG5+P6) Monte Carlo simulated events, as a function of $H_{T,2}/2$ for inclusive 2-jet (left) and 3-jet events (right). The blue line shows the double-sided Crystal Ball function fit of $\frac{\text{Reco } H_{T,2}/2}{\text{Gen } H_{T,2}/2}$ in each $\text{Gen } H_{T,2}/2$ bin, overlaid by Gaussian fitting the core of the resolution (red line).

A fit example for one $\text{Gen } H_{T,2}/2$ bin is shown in Fig. 4.9 for $n_j \geq 2$ (left) and 3-jet events (right). Here the black dots represent the jet response distribution and the double-sided Crystal-Ball fit (blue line) is overlaid by the Gaussian fit (red line). The resolution in each $\text{Gen } H_{T,2}/2$ bin is then plotted as a function of $\text{Gen } H_{T,2}/2$.

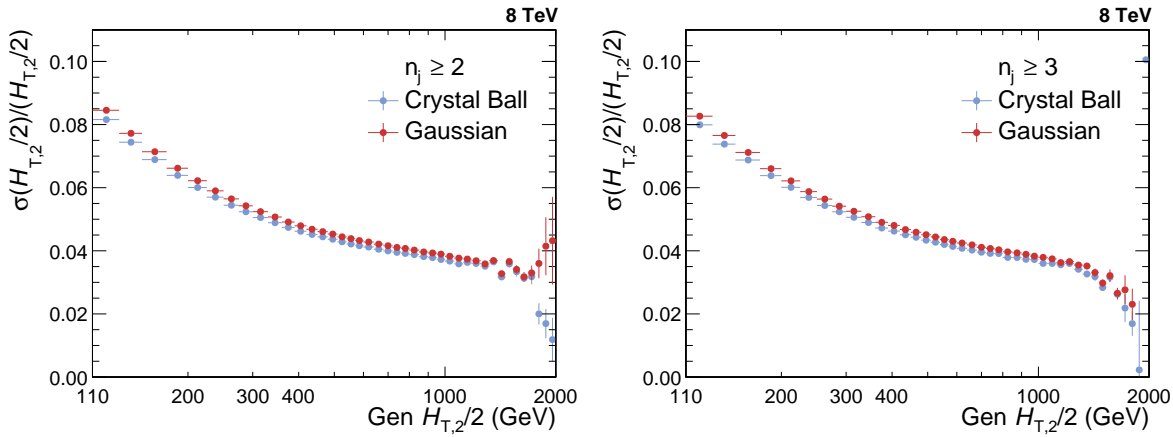


Figure 4.10: Comparison of jet energy resolution calculated using Crystal-Ball fit function (blue solid circles) and Gaussian fit function (red solid circles) for inclusive 2-jet (left) and 3-jet events (right).

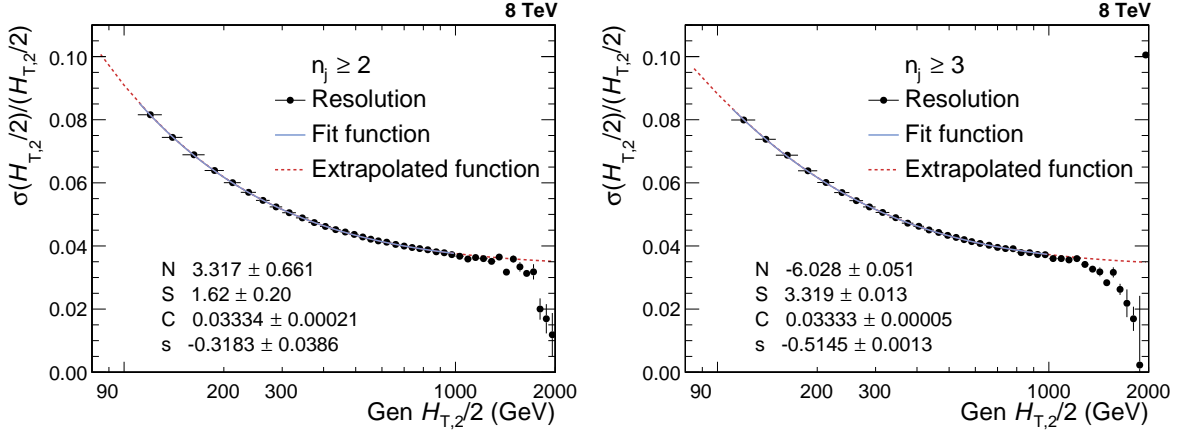


Figure 4.11: Jet energy resolution (JER) is shown as a function of $\text{Gen } H_{T,2}/2$ for inclusive 2-jet (left) and 3-jet events (right). JER (black solid circles) is fitted by using the modified NSC-formula (blue solid line) which is extrapolated to 80 GeV and upto 2000 GeV (red dashed line) to consider the migration into lower as well as higher bins.

As expected, it has been observed from Fig. 4.10 that the Crystal Ball function (blue solid circles) describes the measured distributions better as compared to Gaussian function fit (red solid circles), especially in the low- $H_{T,2}/2$ region where the non-Gaussian tails are more pronounced. Hence JER is determined using Crystal Ball function fit. Figure 4.11 shows the final relative jet energy resolution (JER) which is described by a modified version of the NSC formula (blue solid line) [8], as mentioned in Equation 4.8. To consider the migration to lower as well higher bins and to obtain the resolution with reasonable statistics over the full range of $\text{Gen } H_{T,2}/2$, the fit function is extrapolated to 80 GeV and upto 2000 GeV which is shown by red dashed line. The fit formula used here is basically the usual NSC formula which describes the resolution in terms of noise N originating due to electronic and pileup noise and is independent of $H_{T,2}/2$; a stochastic component S due to sampling fluctuation and EM fraction fluctuation per hadrons; and a constant term C because of dead material, magnetic field and calorimeter cell to cell fluctuation. In the low $H_{T,2}/2$ region the tracking has a non-negligible influence on the resolution due to the particle flow algorithm, so the additional parameter s is introduced to obtain slightly better fits. The parameters obtained after fitting the relative resolution

using the above mentioned NSC formula are tabulated in Table 4.6 for $n_j \geq 2$ and $n_j \geq 3$ events. This calculated JER is used in unfolding procedure to smear the generated truth spectrum which is used as input in getting the response matrices and is explained in details in Sec. 4.5.1. Since JER in $n_j \geq 2$ events is similar to that one in $n_j \geq 3$ events, so N, S and C fit parameters obtained for $n_j \geq 3$ events are used for unfolding R_{32} .

$$\frac{\sigma(x)}{x} = \sqrt{\text{sgn}(N) \cdot \frac{N^2}{x^2} + S^2 \cdot x^{s-1} + C^2} \quad (4.8)$$

Table 4.6: The parameters obtained by fitting the relative resolution as a function of $H_{T,2}/2$, using the modified NSC formula, for inclusive 2-jet and 3-jet events.

	N	S	C	s
Inclusive 2-jet	3.32	1.62	0.0333	-0.318
Inclusive 3-jet	-6.03	3.32	0.0333	-0.515

Since the JER is calculated using MG5+P6 Reco and Gen $H_{T,2}/2$ distributions, so it is expected that if Gen $H_{T,2}/2$ is smeared using this JER, it should match the Reco $H_{T,2}/2$. But this extracted JER in one large rapidity bin, smears the Gen $H_{T,2}/2$ too much because Smeared Gen/Gen ratio (red line) shows a discrepancy from simulated Reco/Gen ratio (blue line), as observed in Fig. 4.12 for $n_j \geq 2$ (left) and $n_j \geq 3$ events (right). Some shortcomings in the detector simulation of the theory spectra leads to these small nonclosures. When the 30% reduced JER is used to smear Gen, then the ratio Smeared Gen/Gen (pink line) matches with simulated Reco/Gen ratio (blue line) within the statistical fluctuations. Hence an additional unfolding uncertainty is attributed by comparison to 30% reduced JER for both $n_j \geq 2$ and $n_j \geq 3$ events. Due to high statistical fluctuations at high $H_{T,2}/2$, range is presented upto 1680 GeV only.

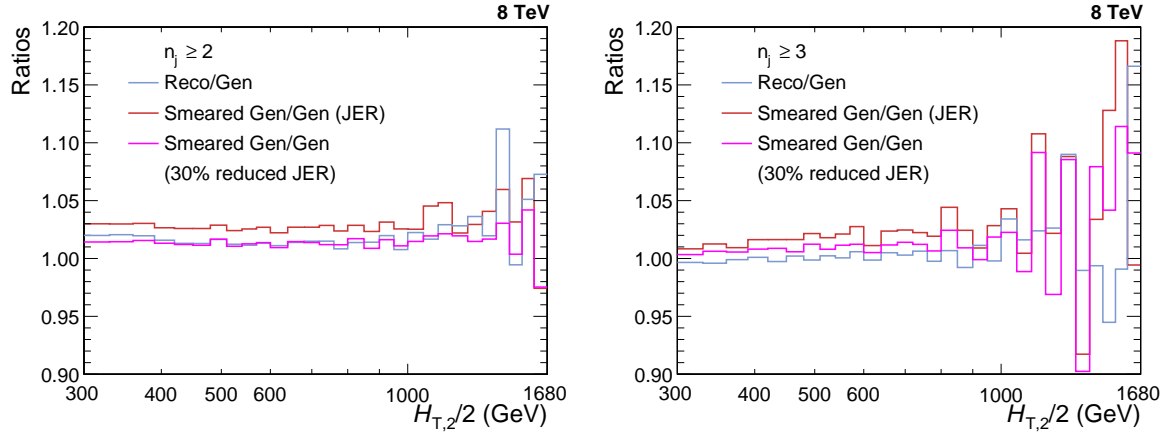


Figure 4.12: MADGRAPH5+PYTHIA6 (MG5+P6) Gen smeared using extracted jet energy resolution (JER) shows a discrepancy from simulated Reco as Smeared Gen/Gen ratio (red line) does not match with Reco/Gen ratio (blue line), for both inclusive 2-jet (left) and 3-jet events (right). Smeared Gen/Gen ratio (pink line) where Gen is smeared using 30% reduced JER matches with simulated Reco/Gen ratio (blue line) within the statistical fluctuations. Hence an additional unfolding uncertainty is attributed by comparison to 30% reduced JER.

4.5 Unfolding

One of the main goals in an experimental measurement is to do the comparison of data with theory predictions or with the results obtained from other experiments. But the finite resolution of a detector and the steeply falling jet p_T spectrum distorts the physical quantities. As a result, the measured observables are different from their corresponding true values. Each p_T bin content contains the migrated events from neighbouring bins along with the original events. So an unfolding process of the data should be followed in order to remove detector effects. In this analysis, the measurements are corrected for detector smearing effects and unfolded to stable particle level by using the iterative D'Agostini Bayesian algorithm [9, 10] as implemented in RooUnfold software package [11]. In this algorithm, the number of iterations regularize the unfolding process. The obtained distribution in one iteration is taken as the input in the next one. χ^2 between two successive iterations is given by Eq. 4.9. The number of iterations stop when χ^2/N_{bins} is < 1 . A reduced χ^2 is obtained by a higher number of iterations but this will also increase the uncertainty and there

are larger bin-by-bin fluctuations and correlations. So the optimization of number of iterations is very important. In the current analysis, unfolding done with “four” iterations gives the best results with low χ^2 and low bin-by-bin correlations.

$$\chi^2 = \sum_{i=1}^{N_{bins}} \left(\frac{n_i^{j+1} - n_i^j}{\sqrt{n_i^j}} \right)^2 \quad (4.9)$$

where n_i^j number of events in i -th bin for j -th iteration

The measured differential cross-sections as a function of $H_{T,2}/2$, are unfolded separately for $n_j \geq 2$ and $n_j \geq 3$ events. The measured cross-section ratio R_{32} is also corrected for detector smearing effects and unfolded to particle level. There can be two ways to obtain unfolded cross-section ratio :

- **Method I** : First unfold separately the inclusive 2-jet and 3-jet measured cross-sections and then construct the ratio R_{32}
- **Method II** : Unfold directly the cross-section ratio R_{32}

In further analysis, unfolded cross-section ratio R_{32} and its systematic uncertainties are calculated using Method I, whereas Method II is used only to propagate the statistical uncertainties including bin-by-bin correlations and statistical correlations between the inclusive 3-jet and 2-jet events cross-sections. Unfolding takes the response matrix as an input which are explained in the next section.

4.5.1 Response Matrices

The response matrix is a two dimensional mapping between the true and measured distributions. It is usually derived from simulated Monte Carlo (MC) samples, which takes the true distribution from MC as an input and smears it by taking into account the detector resolution. Then this response matrix is used to unfold the measured

data spectrum. But there are several drawbacks of constructing response matrix using this method. In some phase space regions, the shape of the distribution is not well described by the LO predictions. Also, the limited number of events in the MC samples at high transverse momenta introduces high statistical fluctuations in the response matrix.

However, there is an indirect way of constructing the response matrix which uses a custom Toy Monte Carlo method. In this method, the particle level or true $H_{T,2}/2$ spectrum is obtained by fitting the theoretically predicted NLO spectrum. Then this distribution is smeared with forward smearing technique, using the extracted jet energy resolution (JER) to obtain the reconstructed level or measured $H_{T,2}/2$ spectrum. After that, the response matrix is constructed from these two distributions is used for the unfolding procedure.

4.5.1.1 Inclusive Cross-sections

The NLO spectrum of the differential cross-sections for $n_j \geq 2$ and $n_j \geq 3$ events obtained using CT10-NLO PDF set are fitted with the following two different functions defined in Eq. 4.10 and 4.13. These functions describes the shape as well as normalization of the distribution.

- **Function I :**

$$f(H_{T,2}/2) = N[x_T]^{-a}[1 - x_T]^b \times \exp[-c/x_T] \quad (4.10)$$

where N is normalization factor and a, b, c are fit parameters.

This function is derived from the below function [12] :

$$f(p_T; \alpha, \beta, \gamma) = N_0[p_T]^{-\alpha} \left[1 - \frac{2 p_T \cosh(y_{min})}{\sqrt{s}} \right]^\beta \times \exp[-\gamma/p_T] \quad (4.11)$$

using

$$\alpha = a, \quad \beta = b, \quad \gamma = c * \sqrt{s}/2, \quad x_T = \frac{2 * H_{T,2}/2 * \cosh(y_{min})}{\sqrt{s}} = \frac{2 * H_{T,2}/2}{\sqrt{s}} \quad (4.12)$$

where transverse scaling variable x_T corresponds to the proton fractional momentum x for dijets with rapidity $y = 0$, $\sqrt{s} = 8000$ GeV and y_{min} is low-edge of the rapidity bin y under consideration (here y_{min} is taken equal to 0)

• **Function II :**

$$f(H_{T,2}/2) = A_0 \left(1 - \frac{H_{T,2}/2}{A_6}\right)^{A_7} \times 10^{F(H_{T,2}/2)}, \text{ where } F(x) = \sum_{i=1}^5 A_i \left(\log\left(\frac{x}{A_6}\right)\right)^i \quad (4.13)$$

where the parameter A_6 is fixed to $\frac{\sqrt{s}}{2 \cosh(y_{min})}$, where $\sqrt{s} = 8000$ GeV and y_{min} is the minimum rapidity. The other parameters are derived from the fitting.

Figure 4.13 shows the fitted CT10-NLO spectrum of differential cross-section as a function of $H_{T,2}/2$ (green solid circles) using Function I (top) and using Function II (bottom) : for inclusive 2-jet (left) and 3-jet events (right). Function I is used primarily to generate response matrices and perform the closure tests and Function II is used as an alternative function to calculate unfolding uncertainty, described in Sec. 4.6.3. To include the migration to lower bins, the fit functions described by red lines are extrapolated to 80 GeV (blue dashed lines).

A flat $H_{T,2}/2$ spectrum is generated by using toy Monte Carlo events and the fit parameters obtained from the NLO spectrum using function I (as shown in Fig. 4.13) provides weights to the flat spectrum. A total of ten million events are generated randomly (in $H_{T,2}/2$ range 80-2000). These generated values are then smeared with a Gaussian function, where σ of the Gaussian is determined from the relative resolution

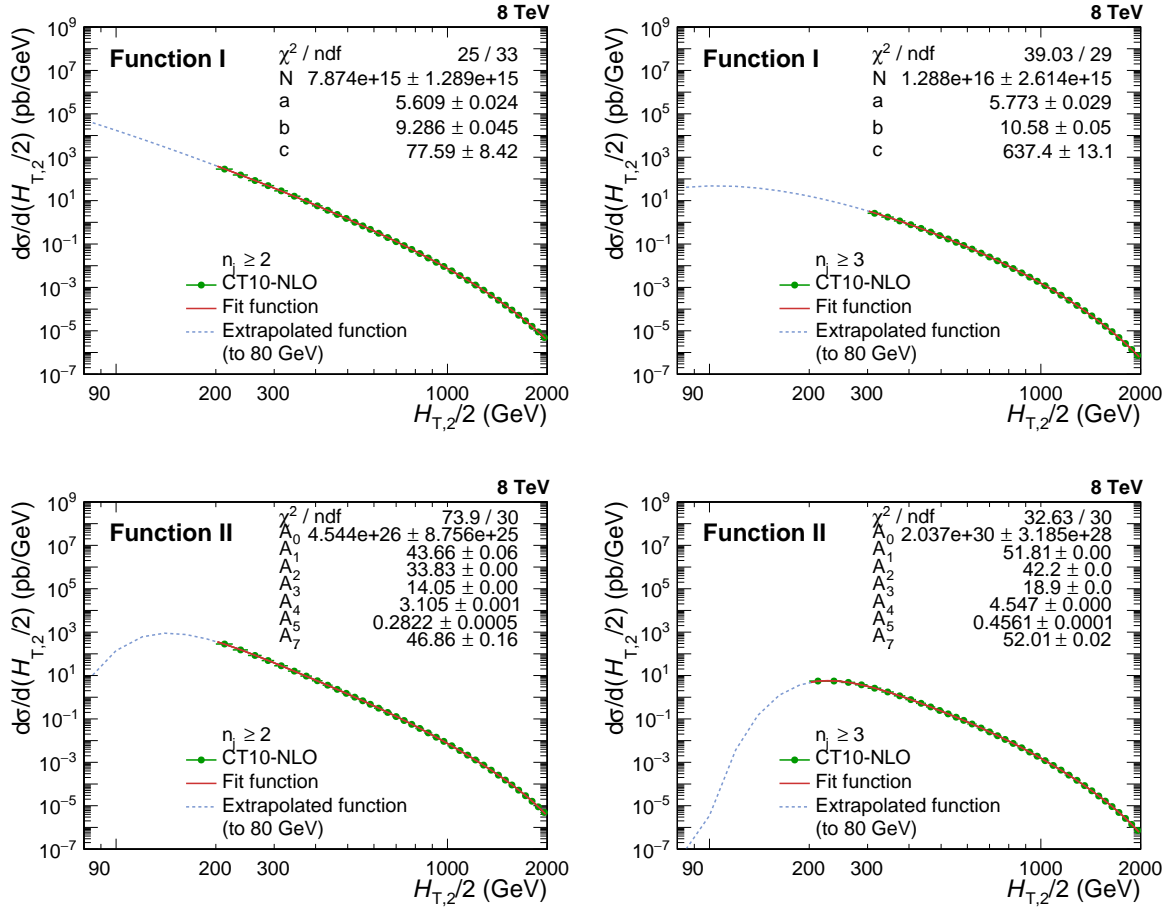


Figure 4.13: Fitted CT10-NLO spectrum of differential cross-section as a function of $H_{T,2}/2$ (green solid circles) using Function I (top) defined in Eq. 4.10 and using Function II (bottom) given by Eq. 4.13, for inclusive 2-jet (left) and 3-jet events (right). To consider the migration to lower $H_{T,2}/2$ bins, the fit functions described by red lines are extrapolated to 80 GeV (blue dashed lines).

parametrization as a function of $H_{T,2}/2$ calculated from NSC formula mentioned in equation 4.8. The parameters N, S, C used for smearing are taken from Table 4.6. These randomly generated (Gen_{Toy}) and smeared ($\text{Measured}_{\text{Toy}}$) values are used to fill the response matrices. Figure 4.14 shows the response matrices derived using the Toy MC for $n_j \geq 2$ (left) and $n_j \geq 3$ events (right). The matrices are normalized to the number of events in each column. The response matrices are diagonal as the migrations in off-diagonal bins are much smaller than the bins along the diagonal.

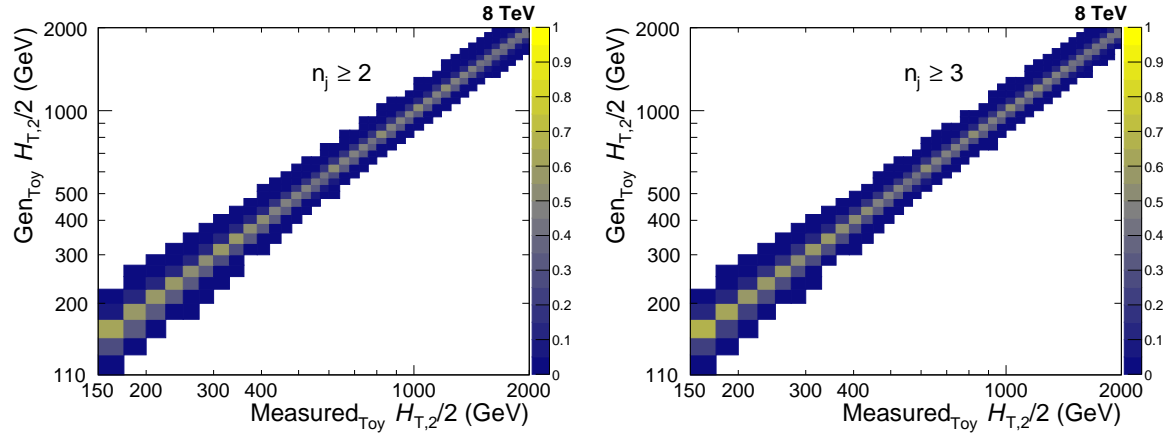


Figure 4.14: The response matrices are derived using the Toy Monte Carlo and forward smearing method, for inclusive 2-jet (left) and 3-jet events (right). The matrices are normalized to the number of events in each column and are diagonal with small off-diagonal migrations between close-by $H_{T,2}/2$ bins.

4.5.1.2 Cross-section Ratio, R_{32}

To obtain the statistical uncertainty on the unfolded cross-section ratio R_{32} , Method II is used. In this method, the response matrix is constructed using Toy MC method as done in Sec. 4.5.1.1 for differential cross-sections. To obtain the true spectrum for R_{32} , the ratio of cross-section spectrum described by Eq. 4.10 for inclusive 3-jet to that of 2-jet events is taken. This ratio is shown by green solid circles in Fig. 4.15 (left) which is fitted using a polynomial function of degree 8 (red line). Then as explained in above section, response matrix is derived for R_{32} using the Toy Monte Carlo and forward smearing method which is shown in Fig. 4.15 (right). The matrix is normalized to the number of events in each column and is diagonal with small off-diagonal migrations between close-by $H_{T,2}/2$ bins.

4.5.2 Closure Test

A closure test has been performed to confirm the working of the unfolding procedure. In this test, $\text{Measured}_{\text{Toy}}$ spectrum is unfolded using the constructed response matrices shown in Figure 4.14. It is expected that the same Gen_{Toy} spectrum should be re-obtained after unfolding. Figure 4.16 confirms that the unfolded $\text{Measured}_{\text{Toy}}$

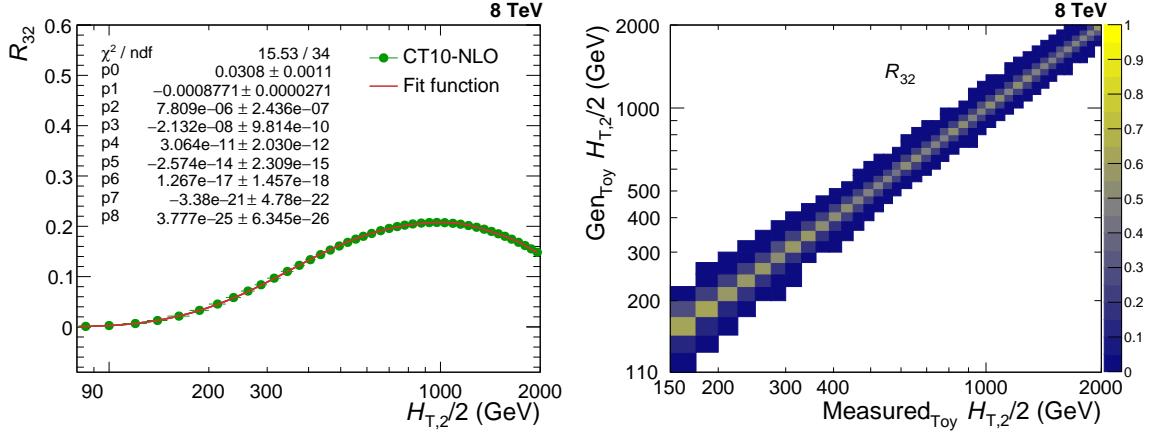


Figure 4.15: Left : The ratio of cross-sections described by Eq. 4.10 for inclusive 3-jet to that of 2-jet events is shown as a function of $H_{T,2}/2$ (green solid circles). It is fit using a polynomial function of degree 8 (red line). Right : The response matrix is derived using the Toy Monte Carlo and forward smearing method, for the cross-section ratio R_{32} . The matrix is normalized to the number of events in each column and is diagonal with small off-diagonal migrations between close-by $H_{T,2}/2$ bins.

spectrum matches exactly with Gen_{Toy} spectrum as the ratio of these distributions is perfectly flat at one for both $n_j \geq 2$ (top left) and $n_j \geq 3$ events (top right) cross-sections as well as the cross-section ratio R_{32} (bottom).

For another closure test, Reco MG5+P6 MC differential cross-section distribution is unfolded using the above constructed response matrices using JER for forward smearing the randomly generated spectrum. While taking ratio of the unfolded distribution to that of Gen MG5+P6 MC, it is observed that a well closure is not obtained. This is represented by blue line in Fig. 4.17 for $n_j \geq 2$ (top left) and $n_j \geq 3$ events (top right). As observed in Fig. 4.12 in Sec. 4.4, if Reco MG5+P6 MC is unfolded using the response matrices obtained using 30% reduced JER, then the good closure is obtained as shown by red line in Fig. 4.17. Since unfolded cross-section ratio R_{32} is the ratio of unfolded differential cross-sections (Method I), same behaviour is observed for R_{32} (bottom).

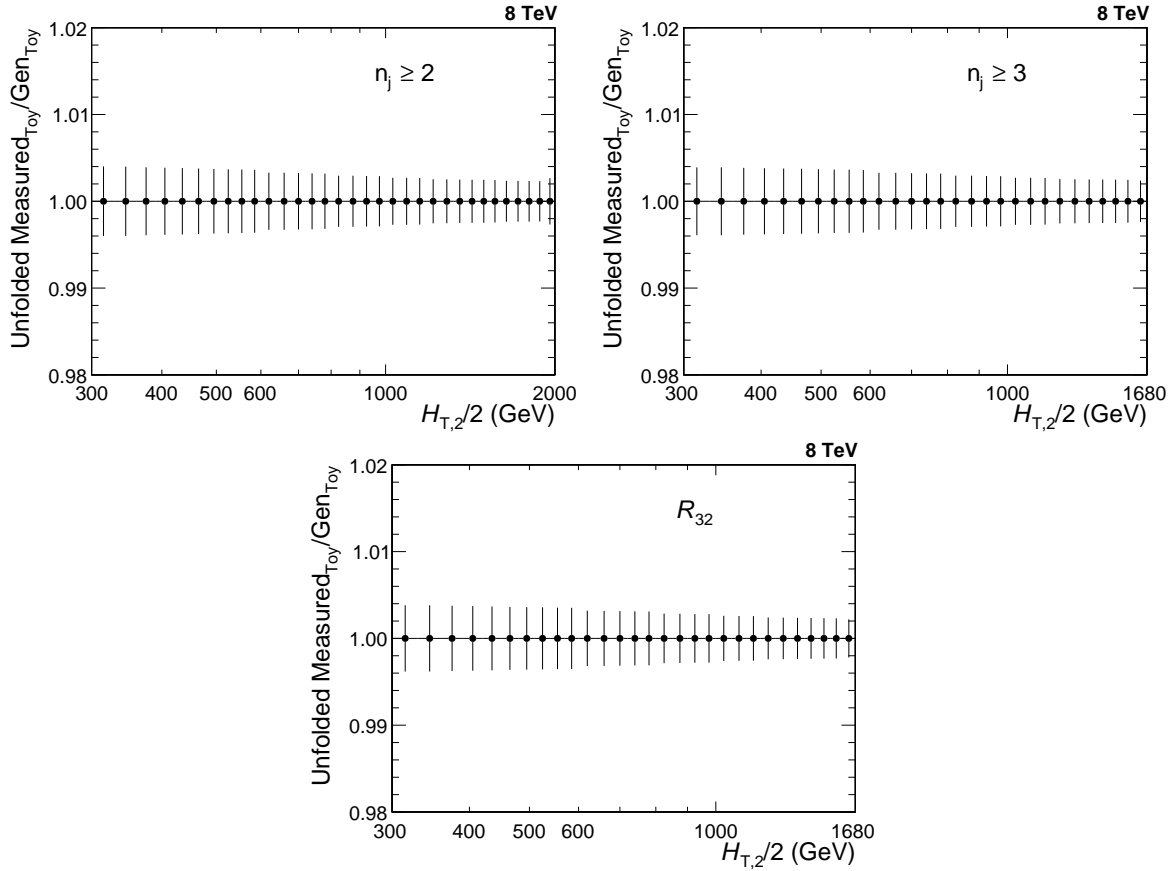


Figure 4.16: Closure test of the unfolding technique where the smeared spectrum obtained from Toy Monte Carlo method (Measured_{Toy}), is unfolded using the constructed response matrices (obtained by forward smearing the randomly generated spectrum (Gen_{Toy}) using extracted jet energy resolution (JER)). As expected, the unfolded measured_{Toy} spectrum matches exactly with Gen_{Toy} spectrum as the ratio of these distributions is perfectly flat at one for both inclusive 2-jet (top left) and 3-jet events (top right) cross-sections as well as the cross-section ratio R_{32} (bottom).

4.5.3 Unfolding of the Measurement

After validity the unfolding method, the measured differential cross-sections as well as R_{32} are unfolded using the above reconstructed response matrices. The unfolded data spectrum is compared to that of measured one in Fig. 4.18 for $\eta_j \geq 2$ (top left) and $\eta_j \geq 3$ events (top right) cross-sections and for the cross-section ratio R_{32} (bottom). As already discussed that 30% reduced JER gives better closures than JER, so the unfolding of data is done with response matrices using JER (blue solid circles) as well as 30% reduced JER (red solid circles) for smearing. The difference

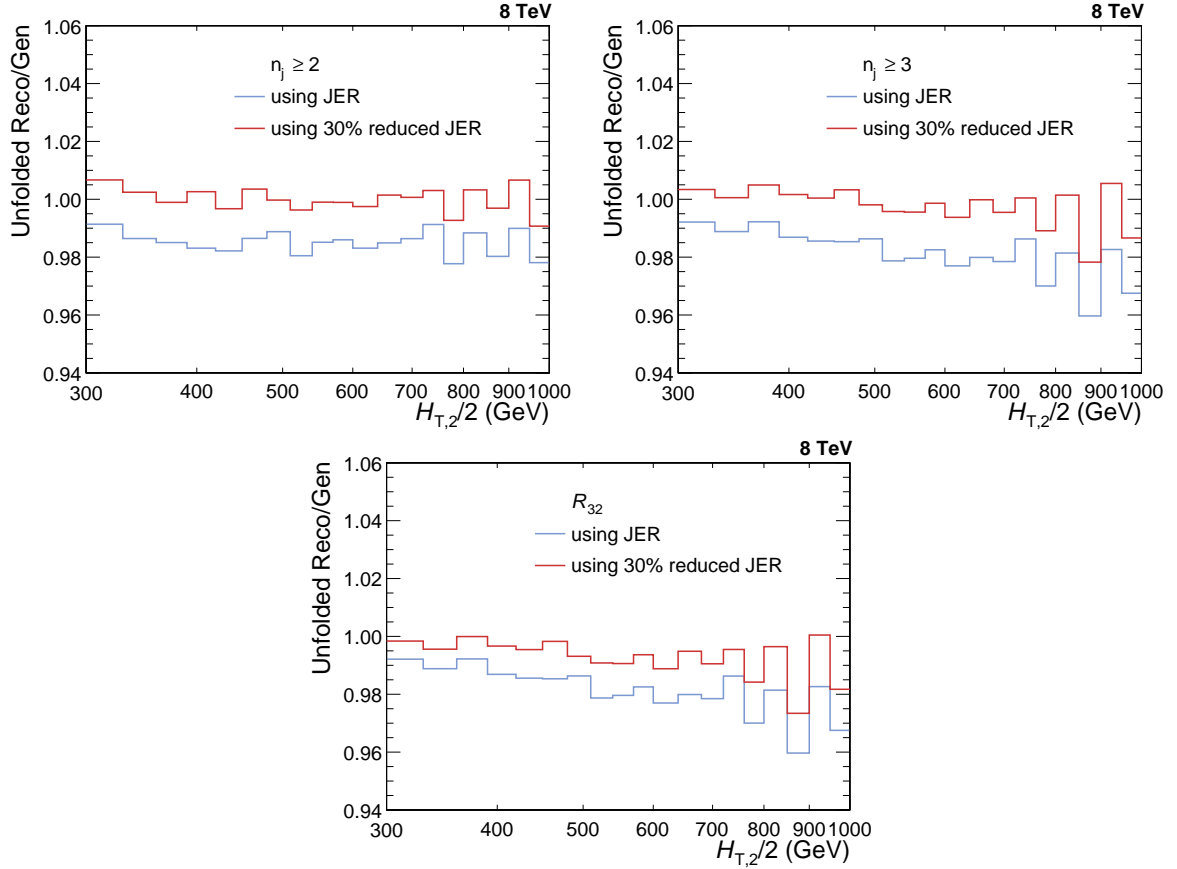


Figure 4.17: Reco MADGRAPH5+PYTHIA6 Monte Carlo (MG5+P6 MC) differential cross-section distributions unfolded with the response matrices (obtained by forward smearing the randomly generated spectrum (Gen) using extracted jet energy resolution (JER)), does not give a good closure with Gen MG5+P6 MC (blue line), for inclusive 2-jet (top left) and 3-jet events (top right). After performing the unfolding using 30% reduced JER, a good closure is obtained (red line). Since unfolded the cross-section ratio R_{32} is the ratio of unfolded differential cross-sections, same behaviour is observed for R_{32} (bottom).

between both is taken as an additional uncertainty on the unfolded measurement.

4.6 Experimental Uncertainties

In an experimental measurement of any physical observable, the uncertainties play a key role and hence are important to study in a physics analysis. The uncertainties can be categorized into two types : statistical and systematic. The statistical uncertainties arise due to random fluctuations depending on the number of events.

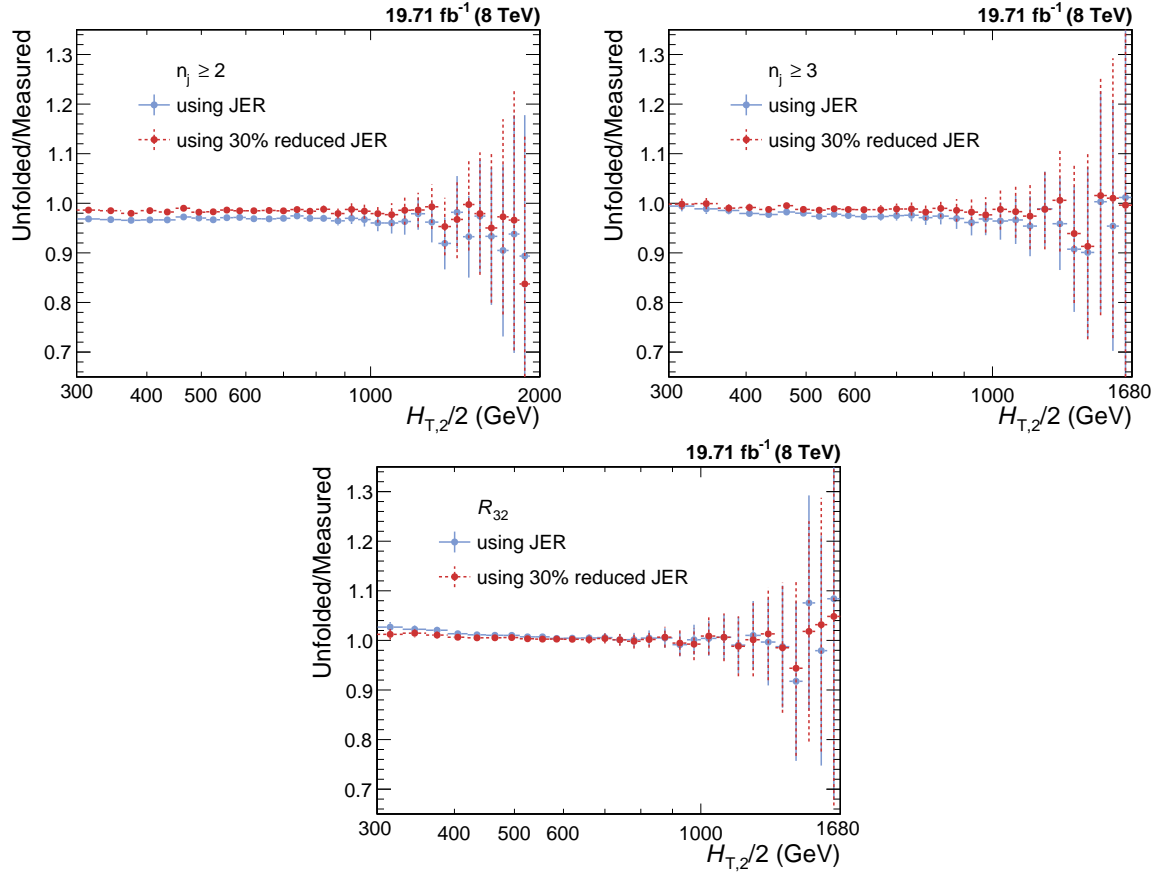


Figure 4.18: The measured differential cross-sections as well as the cross-section ratio R_{32} are unfolded as a function of $H_{T,2}/2$ using the response matrices derived using the Toy Monte Carlo and forward smearing method. The unfolded spectrum are compared with that of the measured one for inclusive 2-jet (top left) and 3-jet events cross-sections (right) as well as for R_{32} (bottom). The unfolding is done with response matrices using JER (blue solid circles) as well as 30% reduced JER (red solid circles) for smearing. The difference between both is taken as an additional uncertainty on the unfolded measurement.

The more the number of events, less is the statistical uncertainty. The systematic uncertainties may be due to known detector effects, model dependence, assumptions made or various corrections applied. In general, if the statistical and systematic uncertainties are uncorrelated, these can be added in quadrature to obtain the total uncertainty on the measurement. In this section, all the experimental uncertainties affecting the measurement of cross-sections and the cross-section ratio R_{32} are described. The systematic experimental uncertainties for R_{32} are propagated from the cross-sections to the ratio taking into account correlations. Due to this, the systematic uncertainties may cancel for R_{32} completely or partially as compared to

those for the individual cross-sections.

4.6.1 Statistical Uncertainty

Statistical uncertainty on the measurement is obtained through the unfolding procedure using a toy MC method. The measured data points are smeared within their statistical uncertainties to get the smeared spectrum. Such smeared spectra are produced million in number and the unfolding is performed multiple times for each smeared spectra. The differences between the unfolded spectra and the measured one give the statistical uncertainty. The unfolding process introduces more statistical fluctuations which can be observed in Fig. 4.19. Here the fractional statistical uncertainties of the unfolded data (red line) are compared with those of the measured one (blue line) for $n_j \geq 2$ (top left) and $n_j \geq 3$ events cross-sections (top right) as well as for the cross-section ratio R_{32} (bottom).

After the unfolding, the final statistical uncertainties become correlated among the bins such that the size of these correlations varies between 10 and 20%. The correlation (anti-) is more significant for neighbouring bins in $H_{T,2}/2$ as compared to the far off ones. In Fig. 4.20, the correlations of the statistical uncertainty after the unfolding can be seen for $n_j \geq 2$ (top left) and $n_j \geq 3$ events cross-sections (top right) and for the cross-section ratio R_{32} (bottom). These correlations must be considered while performing the fits to extract the value of the strong coupling constant, α_S .

4.6.2 Jet Energy Corrections Uncertainty

As explained in Sec. ?, the measured jet energy is corrected for a variety of detector effects by applying jet energy corrections (JEC) [13]. There are 25 mutually independent sources which contribute to JEC. Each source presents a 1σ shift and is fully correlated in p_T and η but uncorrelated to all other sources. The observable is

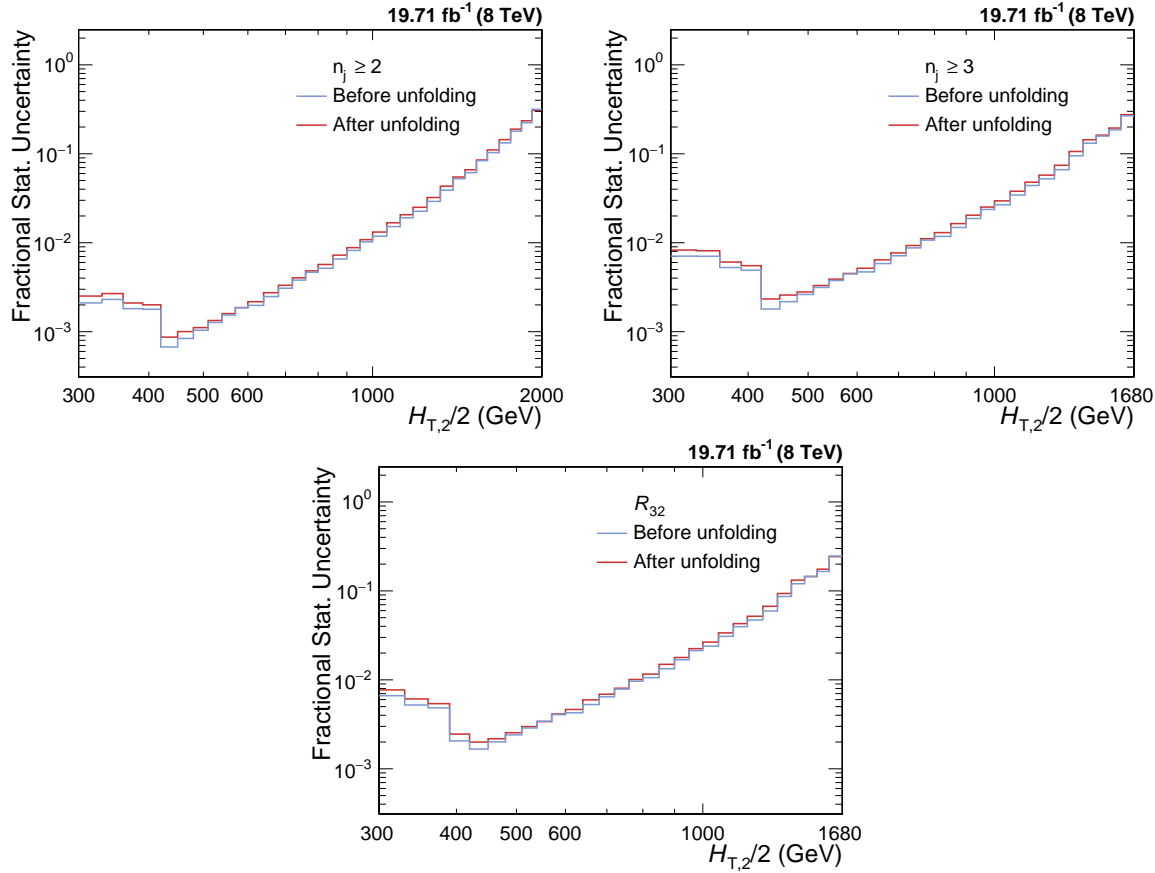


Figure 4.19: The fractional statistical uncertainties of the unfolded data (red line) are compared with those of the measured one (blue line) for inclusive 2-jet (top left) and 3-jet events cross-sections (top right) as well as for the cross-section ratio R_{32} (bottom). After unfolding, the statistical uncertainty increases slightly.

studied with the nominal values of the jet energy which gives nominal distributions as well as by varying up and down the energy of all jets by the uncertainty. The differences between the nominal distributions and the ones obtained by varying the jet energy gives the uncertainties from each source. The JEC uncertainties can be asymmetric in nature which leads to separate treatment of upwards and downwards variation of each source. The sum in quadrature of uncertainties from all sources gives the total JEC uncertainty. In the current analysis, JEC uncertainties are a dominant source of experimental uncertainty at low $H_{T,2}/2$. The JEC uncertainty ranges from 3% to 10% for $n_j \geq 2$ and from 3% to 8% for $n_j \geq 3$ events cross-sections measurement. To calculate JEC uncertainty for ratio R_{32} , the inclusive 2-jet and

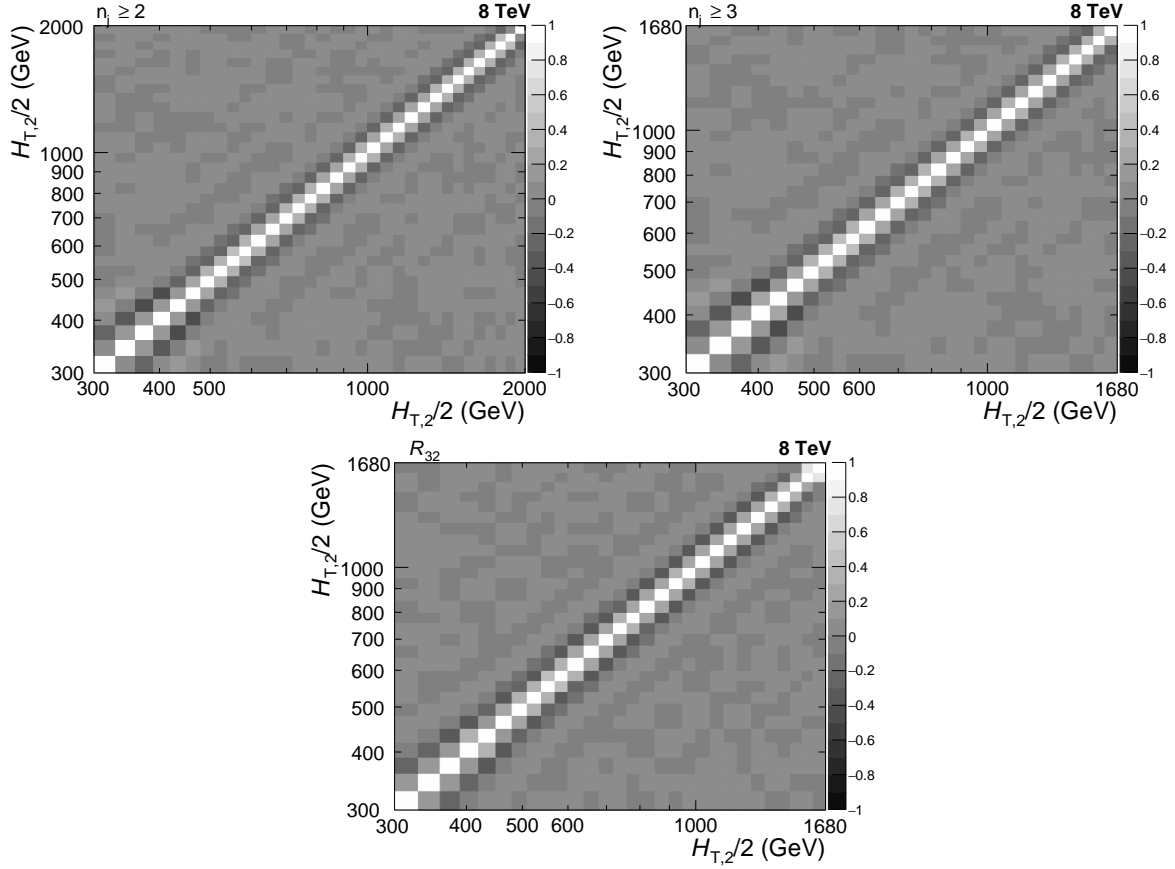


Figure 4.20: The unfolding procedure introduces the correlations of the statistical uncertainty through bin migrations which are shown here for inclusive 2-jet (top left) and 3-jet events cross-sections (top right) as well as for the cross-section ratio R_{32} (bottom). The correlation (anti-) is more significant between neighbouring bins than far-off ones.

3-jet events cross-sections are measured as a function of $H_{T,2}/2$ by shifting the jet p_T according to the JEC uncertainty for each source of JEC separately. Then the ratio of these cross-sections is taken and the difference of these from the central ratio R_{32} , gives the JEC uncertainty for R_{32} . As expected, JEC uncertainty for R_{32} is small as compared to that for individual cross-sections and is about 1 to 2% over all $H_{T,2}/2$ bins.

The sources of JEC considered in the current measurements are : AbsoluteStat, AbsoluteScale, AbsoluteFlavMap, AbsoluteMPFBias, Fragmentation, SinglePionECAL, SinglePionHCAL, FlavorQCD, RelativeJEREC1, RelativeJEREC2, RelativeJERHF, RelativePtBB, RelativePtEC1, RelativePtEC2, RelativePtHF, Rel-

ativeFSR, RelativeStatFSR, RelativeStatEC2, RelativeStatHF, PileUpDataMC, PileUpPtRef, PileUpPtBB, PileUpPtEC1, PileUpPtEC2 and PileUpPtHF. The AbsoluteFlavMap uncertainty is exactly zero for the 8 TeV and can be ignored. For the four sources : RelativeJERHF, RelativePtHF, RelativeStatHF, PileUpPtHF, the JEC uncertainty is exactly zero because of $|y| < 2.5$ cut used in the analysis. So only 20 sources contribute to the total JEC uncertainty. The Figs. A.1-A.3 show the JEC uncertainty from each source separately for inclusive 2-jet (top) and 3-jet events cross-sections (middle) as for cross-section R_{32} (bottom). Depending on the origin of sources, they are categorized into four groups which are described below in brief :

1. **Pileup** : This uncertainty originates from the differences in the transverse momentum between the true offset and the Random Cone method (i.e. essentially difference of pile-up inside and outside of jets), in simulated events. This uncertainty is derived from Z/γ +jet, dijet and multijet data using fit procedure to estimate the residual pileup uncertainty after the calibration.
2. **Relative** : The forward jets are calibrated by the relative η -dependent corrections using dijet events. The main contribution to the uncertainty comes from jet energy resolution (JER), derived by varying JER scale factors up and down by quoted uncertainties and the initial and final state radiation bias corrections.
3. **Absolute** : A global fit to Z/γ +jet and multi-jet events gives the absolute calibration of the jet energy scale. The uncertainties are related to the lepton momentum scale for muons in $Z (\rightarrow \mu\mu)$ +jet and the single pion response in the HCAL.
4. **Flavor** : Flavor response differences are studied from simulation by cross-checking the results with quark- and gluon-tagged γ +jet and Z +jet events. These uncertainties are based on PYTHIA6.4 and HERWIG++2.3 differences

propagated through the data-based calibration method.

The details of the jet energy corrections and uncertainties can be found in [14].

4.6.3 Unfolding Uncertainty

The unfolding uncertainty is comprised of three uncertainties which are explained as follows :

1. **Jet Energy Resolution :** The calculation of the jet energy resolution (JER) using simulated MG5+P6 Monte Carlo events is already explained in Sec. 4.4. As mentioned before, the measured jet transverse momentum (p_T) in simulated MC events needs to be smeared additionally to match the resolution in data. This smearing is done by using measured scale factors ($c_{central}$) mentioned in Table 4.5. It is recommended by JETMET group that the uncertainty on these measured scaling factors must be taken into account in a physics analysis. Since JER is used in constructing the response matrix which is an input in unfolding procedure, so the uncertainty on scale factors accounts for the unfolding uncertainty. To calculate JER uncertainty, p_T is smeared with two additional sets of scale factors corresponding to varying the factors up and down by one sigma, and corresponding $H_{T,2}/2$ is calculated. Then again JER is calculated as a function of $H_{T,2}/2$ using these upwards (c_{up}) and downwards (c_{down}) variations of the scaling factors. Alternative response matrices are built using the JER with above variations and the unfolding is performed again. The differences of the obtained unfolded spectrums to the nominal ones accounts for a systematic JER uncertainty.
2. **Model Dependence :** It is explained in Sec. 4.5.1 that to obtain the true $H_{T,2}/2$ spectrum to be used in constructing response matrix using Toy MC method, the fitting of the CT10-NLO predictions is performed with the Function I described in Eq. 4.10. Using the alternative function, Function II given

by Eq. 4.13, for this fitting and then constructing different response matrix, gives the model dependence of the true $H_{T,2}/2$ spectrum. The differences in unfolded distributions using the above mentioned two different response matrices gives the model dependence uncertainty.

3. **Additional Uncertainty** : Small nonclosures observed in Fig. 4.12 introduces a supplementary uncertainty which is attributed by comparison of distributions unfolded using response matrices constructed using JER from simulation with that obtained with a 30% reduced JER.

All the three above mentioned uncertainties are added in quadrature to get the total unfolding uncertainty which increases from about 1% at low $H_{T,2}/2$ up to 2% at the high $H_{T,2}/2$ ends of the cross-sections for both $n_j \geq 2$ and $n_j \geq 3$ events. This uncertainty account for about less than 1% for R_{32} .

4.6.4 Luminosity Measurement Uncertainty

The measurement of the luminosity delivered to CMS detector by LHC in the proton-proton collisions in the year of 2012 is done by using the silicon pixel cluster counting method [15]. The uncertainty related to the integrated luminosity measurement is estimated to be 2.5% (syst.) and 0.5% (stat.). This uncertainty propagates directly to any absolute cross-section measurement. Hence, a total systematic uncertainty of 2.6% is considered across all the $H_{T,2}/2$ bins. At low $H_{T,2}/2$, it is similar in size as the one from JEC. This uncertainty cancels completely for R_{32} .

4.6.5 Residual Uncertainty

The small trigger and jet identification inefficiencies account for smaller than 1% uncertainties on the cross-section measurements [16, 17]. Hence, an uncorrelated residual uncertainty of 1% is assumed across all $H_{T,2}/2$ bins for both $n_j \geq 2$ and

$n_j \geq 3$ events cross-sections whereas for R_{32} , it gets cancel completely.

4.6.6 Total Experimental Uncertainty

After calculating the uncertainties from all the above mentioned sources, the total experimental uncertainty on measurement of cross-sections as well as cross-section ratio R_{32} , is obtained by adding in quadrature the uncertainties from individual sources. The values of uncertainties (in %) from each source as well as total uncertainty, for each $H_{T,2}/2$ bin, are tabulated in Tables A.2, A.3 and A.4 for $n_j \geq 2$ and $n_j \geq 3$ events cross-sections and cross-section ratio R_{32} , respectively. Figure 4.21 shows the experimental uncertainties, from different sources as well as the total uncertainty, affecting the measurement of $n_j \geq 2$ (top left) and $n_j \geq 3$ events cross-sections (top right) and cross-section ratio R_{32} (bottom). The error bars represent the statistical uncertainty obtained after unfolding. The systematic uncertainties due to jet energy corrections (JEC by blue line), luminosity (red dashed line), unfolding (green dashed line) and residual effects (light purple line) are also presented. The uncertainties due to luminosity and residual effects cancel completely in R_{32} . The total uncertainty (black dashed line) on the measurements is asymmetric in nature and dominated by the uncertainty due to the jet energy corrections (JEC) at lower $H_{T,2}/2$ values and by statistical uncertainty at higher $H_{T,2}/2$ values. The experimental uncertainties from each source as well as total uncertainty are also quoted in Table 4.7.

The complete data analysis of the differential inclusive 2-jet and 3-jet events cross-sections as well as their ratio R_{32} has been presented as a function of $H_{T,2}/2$. The measured spectrums after correcting for detector effects through the unfolding procedure, are compared with the next-to-leading order (NLO) pQCD calculations in the next chapter.

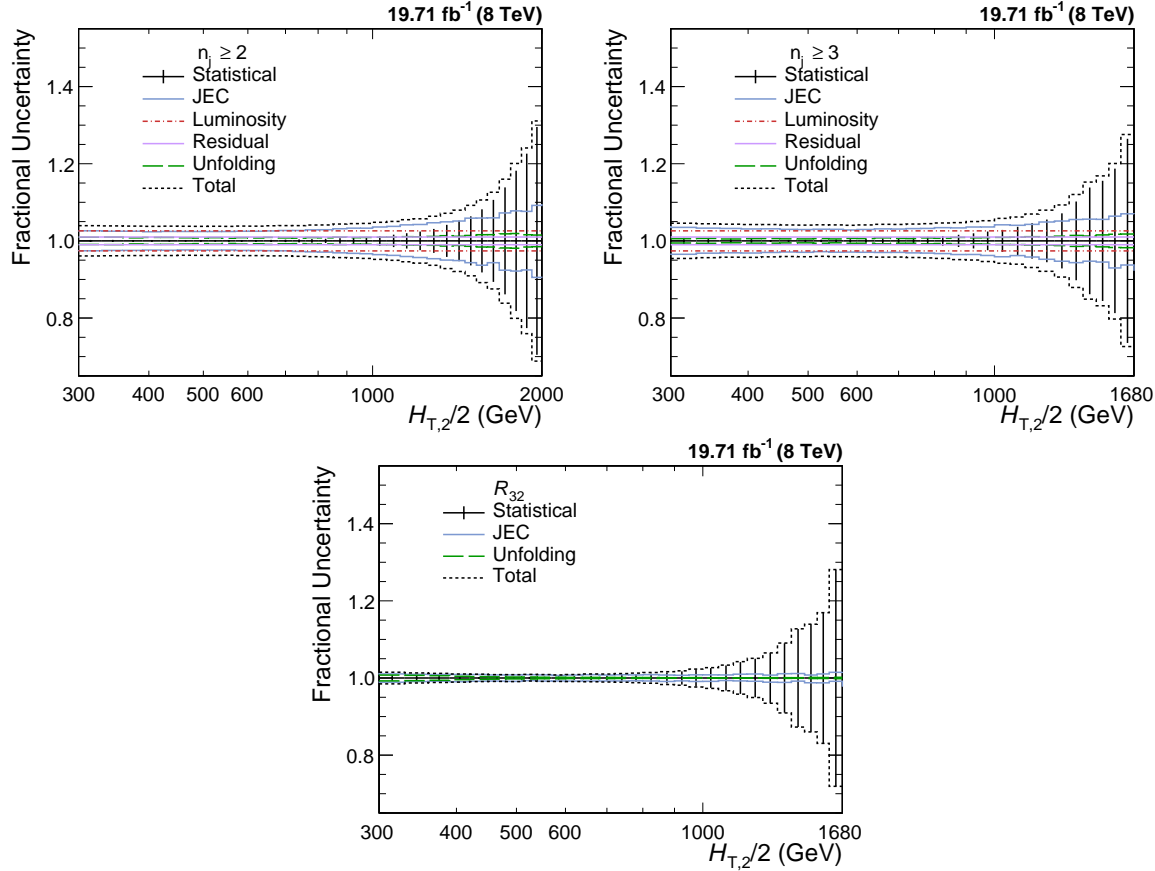


Figure 4.21: Experimental uncertainties from different sources affecting the measurement of cross-sections for inclusive 2-jet (top left) and 3-jet events (top right) and cross-section ratio R_{32} (bottom). The error bars represent the statistical uncertainty after unfolding. The systematic uncertainties due to jet energy corrections (JEC by blue line), luminosity (red dashed line), unfolding (green dashed line) and residual effects (light purple line) are also presented. The uncertainties due to luminosity and residual effects cancel completely in R_{32} . The total uncertainty (black dashed line) is the quadrature sum of the individual sources of uncertainty.

Table 4.7: Overview of all experimental uncertainties affecting the measurement of cross-sections for inclusive 2-jet (left) and 3-jet events (middle) and cross-section ratio R_{32} (right). The uncertainties due to luminosity and residual effects cancel completely in R_{32} . The total uncertainty is the quadrature sum of the individual sources of uncertainty.

Uncertainty Source	Inclusive 2-jet	Inclusive 3-jet	R_{32}
Statistical	< 1 to 30%	< 1 to 27%	< 1 to 28%
Jet energy corrections (JEC)	3 to 10%	3 to 8%	1 to 2%
Unfolding	1 to 2%	1 to 2%	< 1%
Luminosity	2.6%	2.6%	cancels
Residual	1%	1%	cancels
Total	4 to 32%	4 to 28%	1 to 28%

Chapter 5

Theoretical Calculations

In an experiment, the measurements are validated by doing the comparison with the perturbative QCD (pQCD) theoretical calculations. The lowest order (LO) calculations describe well the shapes of the measured distributions but not the normalization due to the dependence on the unphysical renormalization (μ_r) and factorization (μ_f) scales. The next-to-leading order calculations (NLO) improves the precision by reducing the dependence on μ_r and μ_f scales and become an essential feature in the determination of fundamental parameters such as α_S and the parton distribution functions (PDF). This chapter describes the next-to-leading order pQCD calculations used for comparison with the measurements. NLO pQCD calculations need to be corrected for the multiparton interactions (MPI) and hadronization effects by applying non-perturbative (NP) corrections and also for the electroweak interactions (EW).

5.1 Fixed Order NLO Calculations

The predictions of the inclusive differential jet event cross-section at NLO accuracy in pQCD are computed with the NLOJET++ program version 4.1.3 [18, 19]. The results are provided within the framework of FASTNLO version 2.3 [20, 21].

The PDFs are accessed through the LHAPDF6 library [22, 23]. The FASTNLO is preferred over the direct calculation with NLOJET++ because with FASTNLO the calculations of the cross-sections can be repeated several times with different PDFs and scale choices required for calculating the PDF and scale uncertainties. Here the factorization and renormalization scales are chosen equal to $H_{T,2}/2$, i.e. $\mu_f = \mu_r = H_{T,2}/2$.

In the current study, different PDF sets available for a series of different assumptions on the strong coupling constant at the scale of the Z boson mass $\alpha_s(M_Z)$ are used for NLO calculations. Table 5.1 summarizes the already existing PDF sets in LHC Run 1 (upper rows) and the newer PDF sets for Run 2 (lower rows). The different columns list the number of flavours N_f , the assumed masses M_t and M_Z of the top quark and the Z boson, respectively, the default values of $\alpha_s(M_Z)$, and the range in $\alpha_s(M_Z)$ variation available for fits for different PDF sets. All sets uses a variable-flavour number scheme with at most five or six flavours apart from the ABM11 PDFs, which employ a fixed-flavour number scheme with $N_F = 5$. Out of these eight PDF sets the following three are not considered further because of the below mentioned reasons :

- At NLO, predictions based on ABM11 do not describe LHC jet data at small jet rapidity [24–27].
- The HERAPDF2.0 set exclusively fits HERA DIS data with only weak constraints on the gluon PDF.
- The range in values available for $\alpha_s(M_Z)$ is too limited for the NNPDF3.0 set.

Mainly CT10 PDF set is considered for comparison between data and theory predictions as well as for calculating theoretical uncertainties.

Table 5.1: NLO PDF sets are available via LHAPDF6 with various assumptions on the value of $\alpha_s(M_Z)$. The upper rows list the already existing sets in LHC Run 1 and newer ones for Run 2 are listed in lower rows, along with the corresponding number of flavours N_f , the assumed masses M_t and M_Z of the top quark and the Z boson, respectively, the default values of $\alpha_s(M_Z)$, and the range in $\alpha_s(M_Z)$ variation available for fits.

Base set	N_F	M_t (GeV)	M_Z (GeV)	$\alpha_s(M_Z)$	$\alpha_s(M_Z)$ range
ABM11 [28]	5	180	91.174	0.1180	0.110 - 0.130
CT10 [29]	≤ 5	172	91.188	0.1180	0.112 - 0.127
MSTW2008 [30, 31]	≤ 5	10^{10}	91.1876	0.1202	0.110 - 0.130
NNPDF2.3 [32]	≤ 6	175	91.1876	0.1180	0.114–0.124
CT14 [33]	≤ 5	172	91.1876	0.1180	0.111–0.123
HERAPDF2.0 [34]	≤ 5	173	91.1876	0.1180	0.110–0.130
MMHT2014 [35]	≤ 5	10^{10}	91.1876	0.1200	0.108–0.128
NNPDF3.0 [36]	≤ 5	173	91.2	0.1180	0.115–0.121

5.1.1 NLO Correction Factors

The differences between LO predictions and NLO predictions give the effect of the higher-order contributions to the pQCD predictions. These are described by a NLO correction factor, k-factor, which is derived as the ratio of cross-sections at NLO accuracy to that at LO i.e.

$$\text{k-factor} = \frac{\sigma_{\text{NLO}}}{\sigma_{\text{LO}}} \quad (5.1)$$

The impact of the higher-order corrections is determined by the size of k-factor. The small size of k-factor indicates that the cross-section predictions are precisely described at the LO whereas the larger size hints the contributions from NLO. Figure 5.1 shows the k-factors of the NLOJET++ calculations, for inclusive 2-jet and 3-jet event cross-sections and their ratio R_{32} , using five different PDF sets. k-factor for R_{32} is obtained by taking the ratio of k-factors for inclusive 3-jet event cross-sections to that of inclusive 2-jet. The k-factors are similar for all the PDF sets in the lower region, but the differences increase in regions with larger $H_{T,2}/2$. It is observed that for inclusive 3-jet event cross-sections, k-factor jumps at lowest

$H_{T,2}/2$. This is because some jet configurations are kinematically forbidden near the p_T cut bin i.e. 150 GeV. Since the first few bins in $H_{T,2}/2$ (below 225 GeV) still suffer from these kinematical effects, the minimum value of $H_{T,2}/2$ studied is 300 GeV.

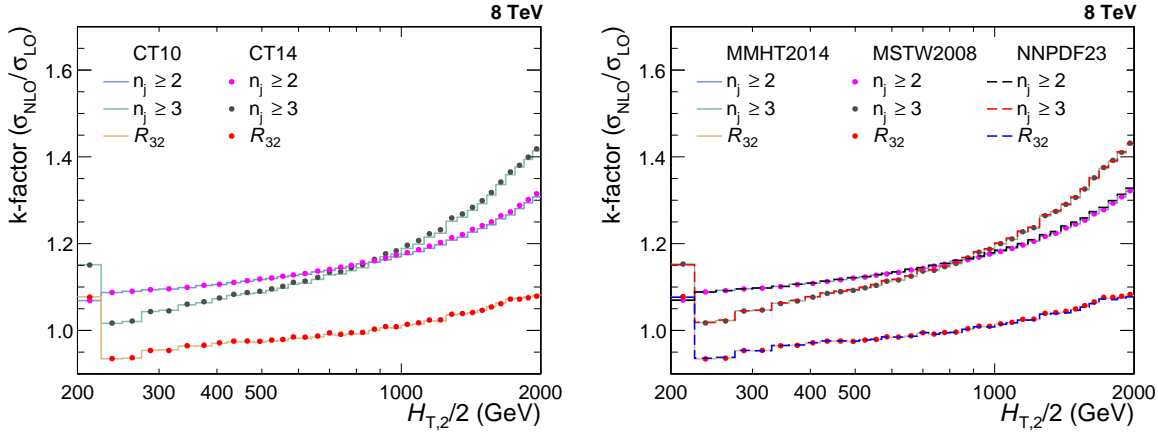


Figure 5.1: The k-factors of the NLOJET++ calculations, for inclusive 2-jet and 3-jet event cross-sections and their ratio R_{32} , using five different PDF sets.

5.1.2 Non-Perturbative Corrections

The fixed-order pQCD NLO calculations predict the parton-level cross-section but lacks accuracy due to several effects. The partons which are emitted close to each other in phase space are not handled well in lower order perturbation theories and hence requires a parton shower (PS) correction. The scattering phenomena between partons within a colliding proton, other than the hard scattering, give rise to multi-parton interactions (MPI). The partons of the hard scattering forms colorless bound states called hadrons through a process of hadronization (HAD). The MPI and hadronization cannot be modelled well within the perturbative framework. Since the fixed-order NLO calculations do not include these additional soft QCD effects, these calculations cannot be compared directly to unfolded data. So the corrections for non-perturbative effects (NP) should be taken into account in NLO calculations. The ratio of cross-section predicted with a nominal event generation interfaced to

the simulation of UE contributions and to the one without hadronization and MPI effects gives the NP correction factors which are defined as :

$$C^{\text{NP}} = \frac{\sigma^{\text{PS+HAD+MPI}}}{\sigma^{\text{PS}}} \quad (5.2)$$

In the current study, the NP effects are estimated by using samples obtained from various MC event generators with a simulation of parton shower and underlying-event (UE) contributions. The leading order (LO), HERWIG++ [37] with the default tune of version 2.3 and PYTHIA6 [2] with tune Z2*, and the NLO, POWHEG [38–40], MC event generators are considered. The matrix-element calculation is performed with POWHEG interfaced to PYTHIA8 with tune CUETS1 [41] for the UE simulation. The ratio, defined in Eq. 5.2, is obtained for each MC generator and is fitted by a power-law function defined in Eq. 5.3. Since this ratio obtained from different MC generators have large differences, so the average of the envelope, which covers all the differences, is taken as the correction factor which is then applied as bin-by-bin multiplicative factor to the parton-level NLO cross-section. The half of the envelope it is taken as the uncertainty on the NP correction factor.

$$f(H_{\text{T},2}/2) = a \cdot (H_{\text{T},2}/2)^b + c \quad (5.3)$$

The NP correction factors, $C_{3\text{-jet}}^{\text{NP}}$ and $C_{2\text{-jet}}^{\text{NP}}$ are calculated for $n_j \geq 2$ and $n_j \geq 3$ event cross-sections respectively and then their ratio gives the correction factor for R_{32} . The correction factors are shown in Fig. 5.2 for the inclusive 2-jet (top left) and 3-jet event cross-sections (top right), and for ratio R_{32} (bottom). At $H_{\text{T},2}/2 \sim 300$ GeV, the NP corrections amount to $\sim 4\text{--}5\%$ for inclusive 2-jet and 3-jet event cross-sections and $\sim 1\%$ for R_{32} , and decrease rapidly for increasing $H_{\text{T},2}/2$. On comparing the NP correction factors of R_{32} with that for individual cross-sections, it has been observed that the non-perturbative effects get reduced in R_{32} .

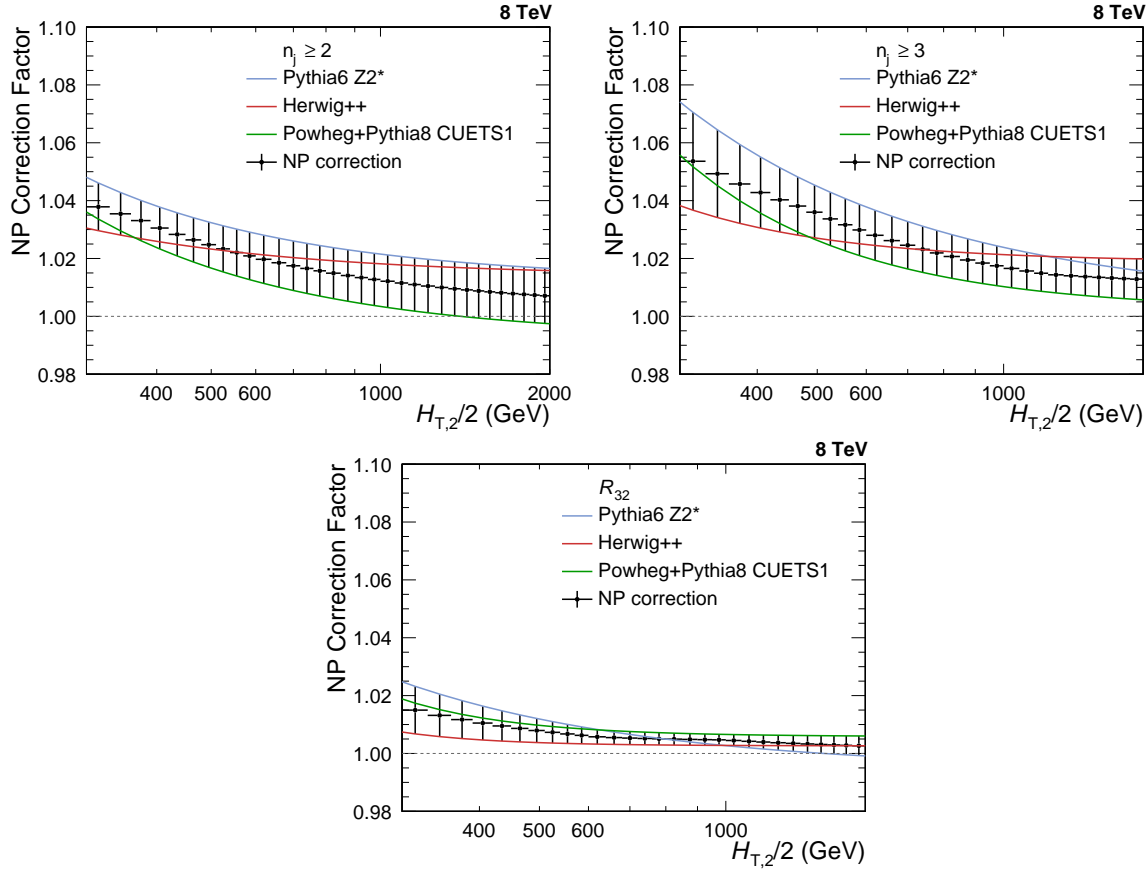


Figure 5.2: The nonperturbative (NP) corrections are presented as a function of $H_{T,2}/2$ for inclusive 2-jet (top left) and 3-jet (top right) event cross-sections, as well as their ratio R_{32} . These corrections are calculated from the leading order HERWIG++ with the default tune of version 2.3 (red line) and PYTHIA6 with tune Z2* (blue line); and the next-to-leading order POWHEG interfaced to PYTHIA8 with tune CUETS1 (green line) Monte Carlo event generators. The black solid circles give the average NP correction factor along with the uncertainty shown by the error bars.

5.1.3 Electroweak Corrections

In LHC, the centre-of-mass energy of proton-proton collisions is well beyond the electroweak (EW) scale $\sim O(100 \text{ GeV})$. At such a high energy, the impact of higher order EW corrections is much more with respect to QCD effects [42] and affect jet cross-sections at large $H_{T,2}/2$. The quark-quark scattering processes involving virtual exchanges of massive W and Z bosons contribute to electroweak (EW) corrections. The fixed-order QCD calculations do not include EW corrections and hence the NLO theory calculations are corrected for EW effects. The EW corrections have

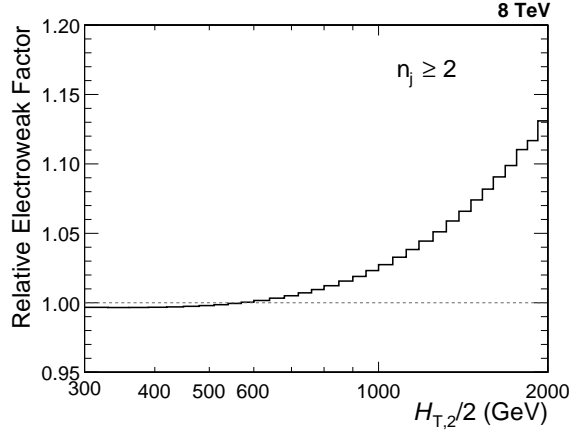


Figure 5.3: The electroweak (EW) corrections [43] in the phase space of the measurement are shown as a function of $H_{T,2}/2$ for inclusive 2-jet event cross-sections. These corrections are applied as a bin-by-bin correction factor to the fixed-order calculation of NLOJET++ as well as the MC predictions of MADGRAPH5+PYTHIA6. The EW correction factor increases up to 13% at high ends of $H_{T,2}/2$ and significantly improves the agreement between data and prediction.

been calculated for inclusive 1-jet and 2-jet case, in Ref. [43]. The EW correction factors in the phase space of the measurement are shown as a function of $H_{T,2}/2$ in Fig. 5.3 for inclusive 2-jet event cross-sections. These correction factor increases up to 13% at high ends of $H_{T,2}/2$ which are applied as a bin-by-bin correction factor to the fixed-order calculation of NLOJET++. To see the effects of EW corrections, a ratio of data to theory predictions obtained using CT10-NLO PDF set and corrected with NP effects without including EW corrections (left) and including EW corrections (right) is plotted for inclusive 2-jet event cross-sections in Fig. 5.4. On comparing both the figures, it is observed that the EW corrections significantly improve the agreement between data and prediction in the high $H_{T,2}/2$ region. EW corrections are not available yet for inclusive 3-jet production and hence not applied for inclusive 3-jet event cross-sections. The guess from theory side is that EW for inclusive 2-jet and 3-jet will be similar, so for R_{32} , it is assumed to be equal to the factor of 1. Since the EW effects are not taken care of in MC simulations so these corrections are applied to MC predictions also.

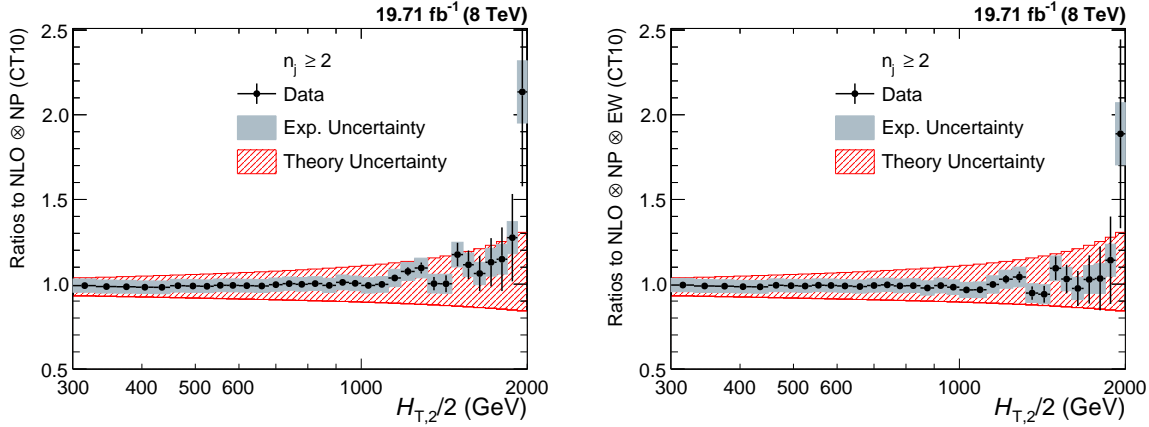


Figure 5.4: Ratio of data over theory obtained using the CT10-NLO PDF set and corrected with non-perturbative effects (NP) without including electroweak (EW) corrections (left) and including EW corrections (right) is shown for inclusive 2-jet event cross-sections. The error bars represents the statistical uncertainty of the data and the shaded rectangles represents the total experimental systematic uncertainty. The shaded band around unity indicate the total uncertainty of the theory. The EW corrections significantly improve the agreement between data and prediction in the high $H_{T,2}/2$ region.

5.2 Theoretical Uncertainties

The measurements are not only sensitive to experimental uncertainties but also to the theoretical uncertainties. The renormalization and factorization scale variations, PDF uncertainties and the non-perturbative corrections contribute to theoretical uncertainties which are described below :

5.2.1 Scale Uncertainty

In perturbative QCD calculations of cross-sections, one has to choose a renormalization (μ_r) and factorization (μ_f) scale. The dependence on scales is negligible if these calculations are performed for all orders of the perturbative series. But the perturbative series is truncated at NLO, so there is a scale dependence of the measurement which is covered by systematic uncertainty known as scale uncertainty. The scale uncertainty is evaluated with the conventional recipe of varying the default scale $H_{T,2}/2$ chosen for μ_r and μ_f independently in the following six combinations: $(\mu_r/H_{T,2}/2, \mu_f/H_{T,2}/2) = (1/2, 1/2), (1/2, 1), (1, 1/2), (1, 2), (2, 1)$ and $(2, 2)$. The

maximal upwards and downwards deviations in cross-section from the central prediction give the scale uncertainty. To calculate the scale uncertainty for cross-section ratio R_{32} , first R_{32} is obtained for each above mentioned scale choice and then its difference from central R_{32} is taken. The scale uncertainty calculated using CT10-NLO PDF set ranges from 5% to 13% and 11% to 17% for inclusive 2-jet and 3-jet events cross-sections respectively, and from 6% to 8% for R_{32} .

5.2.2 PDF Uncertainty

The calculation of jet cross-sections in proton-proton collisions relies upon the knowledge of PDFs. These PDF sets are determined by global fits to all the available deep inelastic scattering (DIS) and related hard scattering data from different experiments. The various sources affect the PDFs such as theory model, input parameters like the strong coupling constant α_S , the quark masses and the statistical and systematic uncertainty sources of the data included in the PDF fit. These sources contribute to PDF uncertainty which is evaluated according to the prescriptions given for each PDF set. The CT10-NLO PDF set [29, 44] employ the eigenvector method to evaluate the PDF uncertainties. The CT10-PDF set consists of $N_{\text{ev}} = 26$ eigenvectors with two PDF members per eigenvector k , which are varied upwards and downwards to generate a set of eigenvector pairs. The asymmetric uncertainties, ΔX^+ and ΔX^- , of a quantity X are given by Eq. 5.4 where X_0 is the central prediction, X_k^+ and X_k^- are the predictions using the upwards and downwards variation of each eigenvector k .

$$\begin{aligned}\Delta X^+ &= \sqrt{\sum_{k=1}^{N_{\text{ev}}} [\max(X_k^+ - X^0, X_k^- - X^0, 0)]^2} \\ \Delta X^- &= \sqrt{\sum_{k=1}^{N_{\text{ev}}} [\min(X_k^+ - X^0, X_k^- - X^0, 0)]^2}\end{aligned}\tag{5.4}$$

The symmetric uncertainty (ΔX^\pm) is given by half the difference of the upwards and downwards variations :

$$\Delta X^\pm = \sqrt{\sum_{k=1}^{N_{\text{ev}}} \left[\frac{X_k^+ - X_k^-}{2} \right]^2} \quad (5.5)$$

The CT10-NLO PDF set uncertainties are downscaled by a factor of 1.64 in order to have the uncertainties at the 68.3% confidence level $\text{CL}(1\sigma)$ instead of 90% $\text{CL}(2\sigma)$ such that to have a uniform treatment with respect to other PDF sets. The PDF uncertainty as derived with the CT10-NLO PDF set is the dominant source of uncertainty and ranges from 3% to 30% for inclusive 2-jet and from 4% to 32% for 3-jet cross-sections. For R_{32} , the ratio of predictions for inclusive 3-jet to that of 2-jet is taken for each eigen vector with upwards and downwards variations separately and then PDF uncertainty is calculated as done for individual cross-sections. The PDF uncertainty ranges and from 2% to 10% for cross-section ratio R_{32} .

5.2.3 Non-perturbative Uncertainty

As discussed in 5.1.2, the differences in the non-perturbative (NP) corrections calculated from various Monte Carlo event generators introduce the NP uncertainty which is of the order of 1% and 1 to 2% for inclusive 2-jet and 3-jet event cross-sections respectively, and $< 1\%$ for cross-section ratio R_{32} .

5.2.4 Total Theoretical Uncertainty

The total systematic theoretical uncertainties are obtained as the quadratic sum of the scale, PDF and NP uncertainties. Figure 5.5 presents the systematic theoretical uncertainties affecting the cross-section measurement for inclusive 2-jet (top left) and 3-jet events (top right) and the cross-section ratio R_{32} (bottom), using CT10-

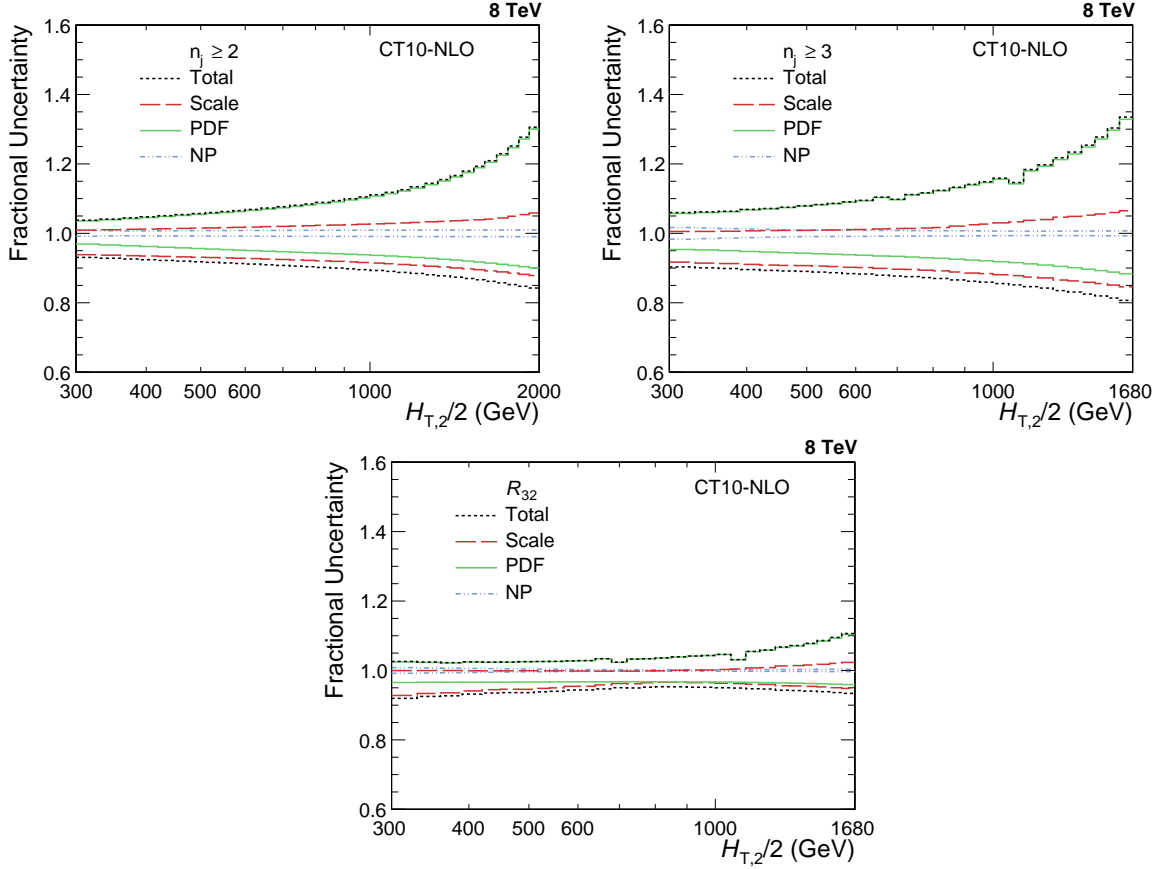


Figure 5.5: The systematic theoretical uncertainties affecting the cross-section measurement for inclusive 2-jet (top left) and 3-jet events (top right) and their ratio R_{32} (bottom). The scale (red dashed line), PDF (green line) and NP (blue dashed line) uncertainties as well as total uncertainty (black dashed line) obtained using CT10-NLO PDF set are shown. The total theoretical uncertainty is asymmetric and is dominated by PDF uncertainty.

NLO PDF set. The scale (red dashed line), PDF (green line) and NP (blue dashed line) uncertainties as well as total theoretical uncertainty (black dashed line) are shown. The total theoretical uncertainty is asymmetric and is dominated by PDF uncertainty which grows in magnitude with increasing value of $H_{T,2}/2$. Table 5.2 quotes the values of the theoretical uncertainty from each source as well as total uncertainty affecting the measurements. The bin-wise values of uncertainties (in %) from each source as well as total uncertainty are shown in Tables A.5, A.6 and A.7 for $n_j \geq 2$ and $n_j \geq 3$ event cross-sections and cross-section ratio R_{32} , respectively. The computation of the NLO predictions with NLOJET++ is also

subject to statistical fluctuations from the complex numerical integrations. For the inclusive 2-jet event cross-sections this uncertainty is smaller than about a per mille, while for the inclusive 3-jet event cross-section it amounts to 1-9 per mille. Hence the statistical uncertainty is not considered in the total theoretical uncertainty. The small dips at ~ 700 and 1000 GeV in the PDF uncertainty for inclusive 3-jet events cross-sections and cross-section ratio R_{32} is a feature of the CT10-NLO PDF set.

Table 5.2: Overview of all systematic theoretical uncertainties, obtained using CT10-NLO PDF set, affecting the measurement of cross-sections for inclusive 2-jet (left) and 3-jet events (middle) and cross-section ratio R_{32} (right).

Uncertainty Source	Inclusive 2-jet	Inclusive 3-jet	R_{32}
Scale	5 to 13%	11 to 17%	6 to 8%
PDF	3 to 30%	4 to 32%	2 to 10%
Non-perturbative (NP)	1%	1 to 2%	$< 1\%$
Total	3 to 30%	5 to 34%	3 to 11%

5.3 Comparison of Theory to Data

After correcting the measurement for detector effects as well as NLO pQCD calculations for non-perturbative (NP) and electroweak (EW) effects, it is now feasible to compare the measured cross-sections with the theory predictions. Figure 5.6 shows the measured differential inclusive 2-jet and 3-jet event cross-sections as a function of $H_{T,2}/2$ after unfolding for detector effects. On the left, the measurements (points) are compared to the NLOJET++ predictions using the CT10-NLO PDF set (line), corrected for NP effects and in addition for EW effects in the 2-jet case. On the right, the comparison is made to the predictions from MADGRAPH5+PYTHIA6 (MG+P6) with tune Z2* (line), corrected for EW effects in the 2-jet case. The error bars give the total experimental uncertainty, given by the quadrature sum of the statistical and systematic uncertainties. On a logarithmic scale, the data are in well agreement with the NLO predictions over the whole range of $H_{T,2}/2$ from 300 GeV up to 2000

(2-jet) and 1680 GeV (3-jet) respectively.

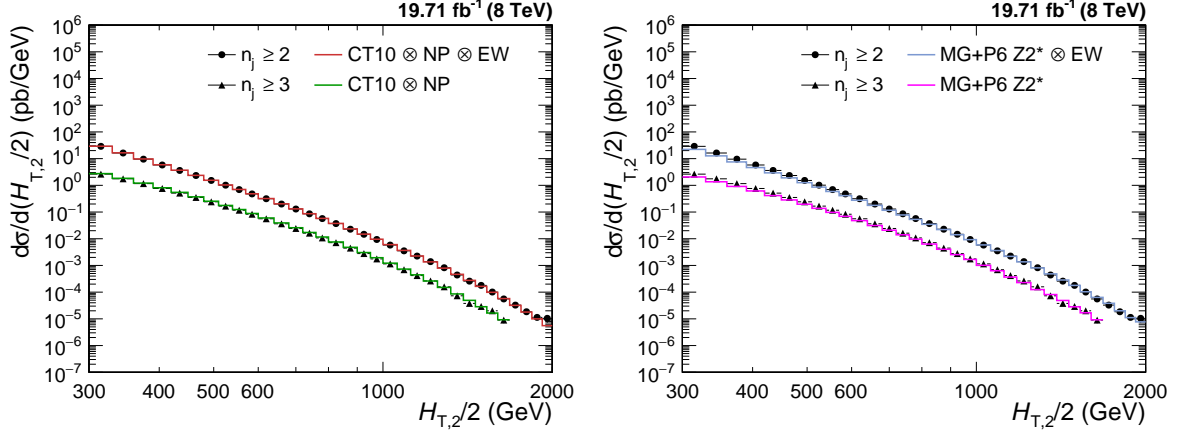


Figure 5.6: Comparison of the measured differential inclusive 2-jet and 3-jet event cross-sections as a function of $H_{T,2}/2$ to theoretical predictions. On the left, the data (points) are shown together with NLOJET++ predictions (line) using the CT10-NLO PDF set, corrected for non-perturbative (NP) and electroweak (EW) effects (2-jet) or only NP effects (3-jet). On the (right), the data (points) are compared to predictions from MADGRAPH5+PYTHIA6 (MG+P6) with tune Z2* (line), corrected for EW effects in the 2-jet case. The error bars give the total experimental uncertainty, given by the quadrature sum of the statistical and systematic uncertainties.

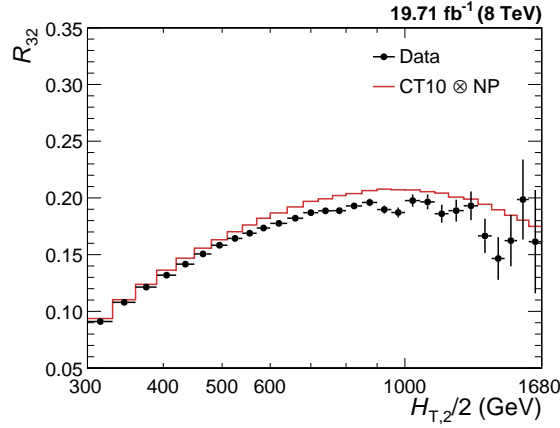


Figure 5.7: Cross-section ratio R_{32} as a function of $H_{T,2}/2$ calculated from data (solid circles) in comparison to that from NLO pQCD predictions obtained using the CT10-NLO PDF set corrected with non-perturbative (NP) corrections (line). The error bars correspond to the total experimental uncertainty derived as quadratic sum from all uncertainty sources.

Figure 5.7 shows the cross-section ratio R_{32} obtained from unfolded data data (solid circles) in comparison to that from NLO pQCD predictions obtained using the CT10-NLO PDF set corrected with NP corrections (line). The error bars here

represents the total experimental uncertainty derived as quadratic sum from all uncertainty sources. The deviations of measured R_{32} from the theoretical predicted value can be explained by the electroweak effects which are not considered yet because of their unavailability for inclusive 3-jet event cross-sections.

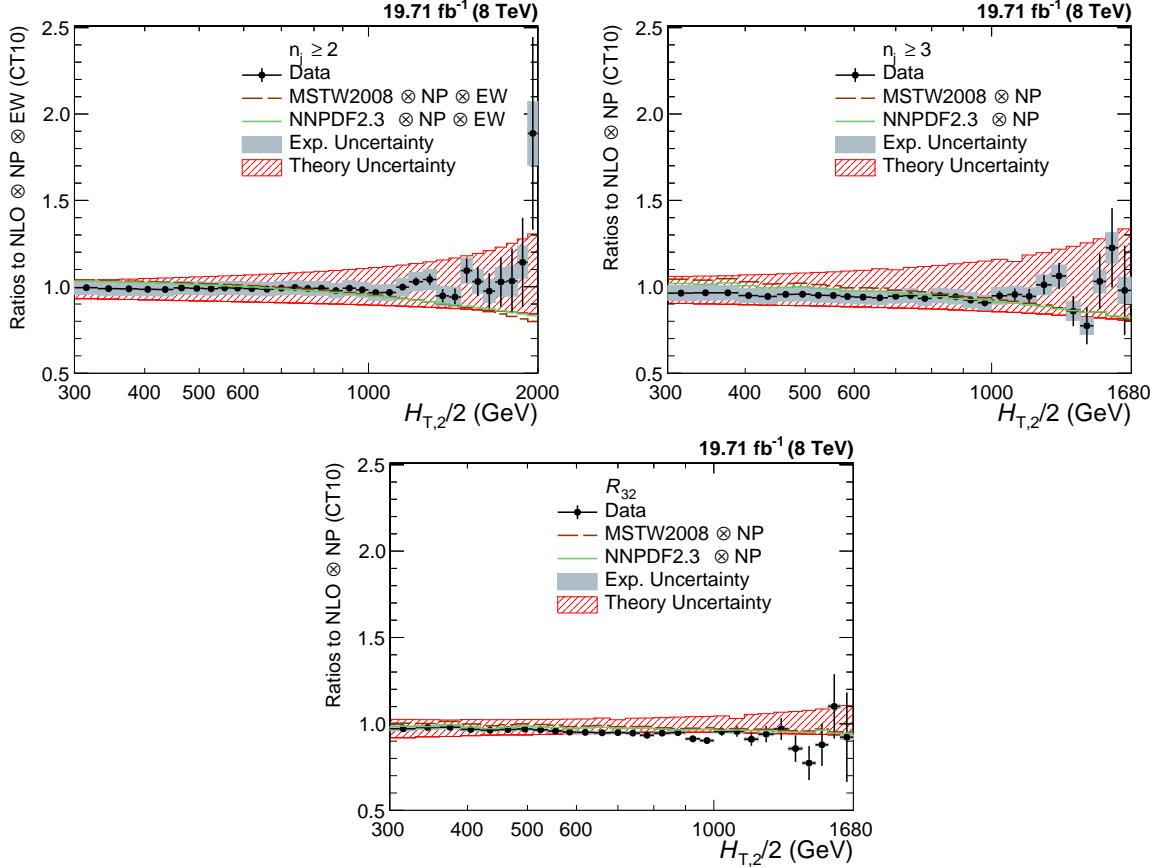


Figure 5.8: Ratio of data over theory using the CT10-NLO PDF set for inclusive 2-jet (top left) and 3-jet event cross-sections (top right) and their ratio R_{32} (bottom). The theory predictions are corrected for non-perturbative effects (NP) and also for electroweak effects (EW) for inclusive 2-jet only. For comparison predictions employing two other PDF sets, MSTW2008 and NNPDF2.3, are also shown. The error bars represent the statistical uncertainty of the data and the shaded rectangles represent the total experimental systematic uncertainty. The shaded band around unity indicates the total uncertainty of the theory.

For better visibility, the ratios of data over the theory at NLO are also studied in details. In Fig. 5.8, the ratios of data over NLOJET++ predictions using the CT10-NLO PDF set are shown for inclusive 2-jet (top left) and 3-jet event cross-sections (top right) as well as their ratio R_{32} (bottom). The data are well described by the predictions within their uncertainty, which is dominated at large $H_{T,2}/2$ by

PDF effects in the upwards and by scale variations in the downwards direction. A trend towards an increasing systematic excess of the 2-jet data with respect to theory, starting at about 1 TeV in $H_{T,2}/2$, is remedied by the inclusion of EWK corrections. In the 3-jet case the statistical precision of the data and the reach in $H_{T,2}/2$ is insufficient to observe any effect. The alternative PDF sets MSTW2008 and NNPDF2.3 exhibit a small underestimation of the cross-sections at high $H_{T,2}/2$.

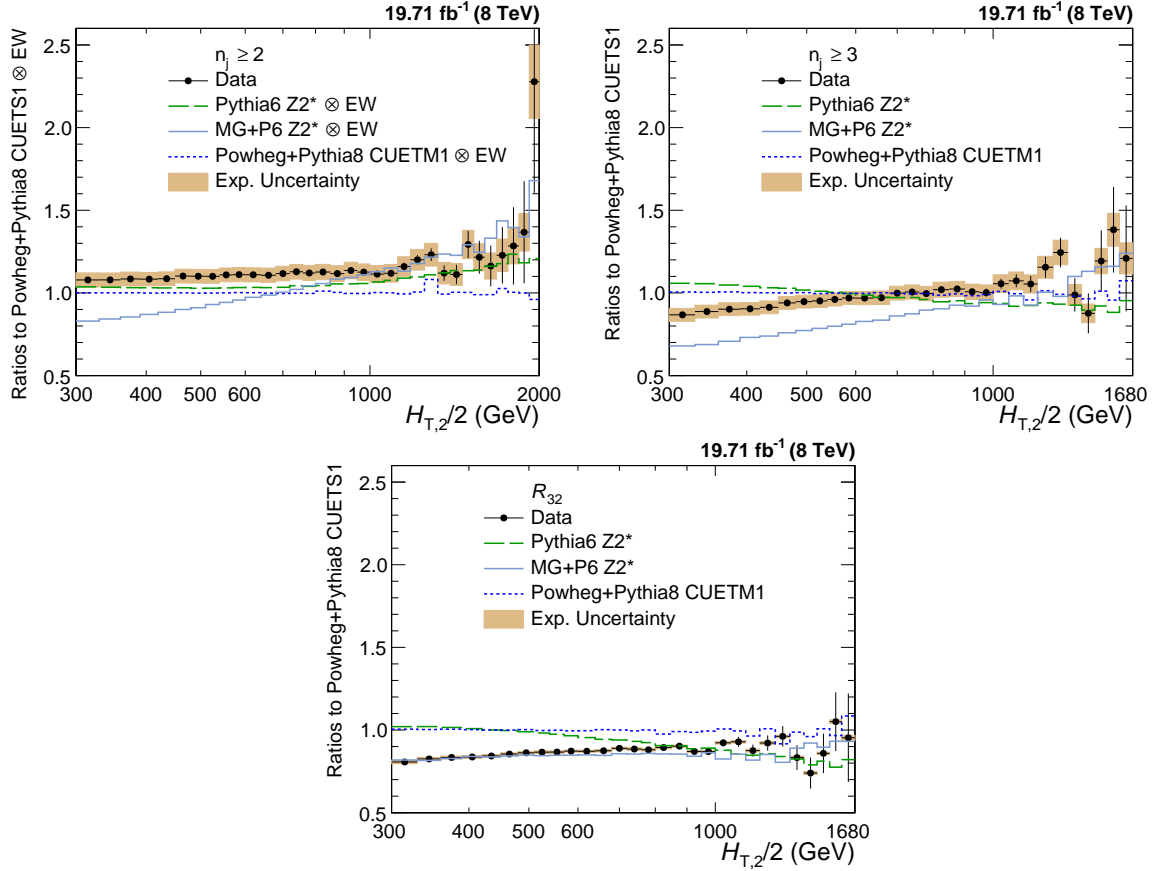


Figure 5.9: Ratio of data over the prediction from POWHEG+PYTHIA8 with tune CUETS1 are presented for inclusive 2-jet (top left) and 3-jet event cross-sections (top right) as well as their ratio R_{32} (bottom). For comparison the alternative tune CUETM1 of POWHEG+PYTHIA8, the tree-level multi-leg improved prediction by MADGRAPH5+PYTHIA6 with tune Z2*, and the the LO MC predictions from PYTHIA6 tune Z2* are shown as well. The error bars correspond to the statistical uncertainty of the data and the shaded rectangles to the total experimental systematic uncertainty. EW corrections have been accounted for in this comparison in the 2-jet case only.

The POWHEG framework providing a NLO dijet calculation matched to the parton showers of PYTHIA8 employed with the CUETS1 and CUETM1 tunes [41] is

also used for a comparison. The ratios of data over theory from POWHEG+PYTHIA8 with tune CUETS1 are shown for inclusive 2-jet (top left) and 3-jet event cross-sections (top right) as well as their ratio R_{32} (bottom) in Fig. 5.9. For comparison, the LO prediction from PYTHIA6 with tune Z2*, the tree-level multi-leg improved prediction by MADGRAPH5+PYTHIA6 with tune Z2*, and the matched NLO prediction from POWHEG+PYTHIA8 with tune CUETM1 are shown as well. EW corrections have been accounted for in this comparison in the 2-jet case only. Significant discrepancies, which are cancelled to a large extent in the ratio R_{32} , are visible in the comparison with the LO prediction from MADGRAPH5+PYTHIA6 with tune Z2*, in particular for small $H_{T,2}/2$. In contrast, the employed dijet MC POWHEG+PYTHIA8 better describe the 2-jet event cross-section, but fail for the 3-jet case.

The jet measurements at hadron colliders can be used to extract the strong coupling constant α_S , which is discussed in the next chapter.

Chapter 6

Determination of the Strong Coupling Constant

The inclusive jet production cross-section at hadron colliders mainly depends on the strong coupling constant α_S for a given centre-of-mass energy. Hence the measurements of the inclusive jet cross-section and jet properties provide a direct probe to measure the strong coupling constant. The measurement of α_S has been already done by various experiments such as CMS [17, 26, 45–47], ATLAS [48], D0 [49, 50], H1 [51, 52], and ZEUS [53]. In this thesis, the measurements of differential inclusive 2-jet and 3-jet event cross-sections as well as the cross-section ratio R_{32} , as a function of $H_{T,2}/2$ are used to extract the value of the strong coupling constant at the scale of the Z boson mass $\alpha_s(M_Z)$. The differential inclusive jet production cross-section upto at NLO is given by [54] :

$$\frac{d\sigma}{d(H_{T,2}/2)} = \alpha_S^2(\mu_r) \hat{X}^{(0)}(\mu_f, H_{T,2}/2) [1 + \alpha_S(\mu_r) K1(\mu_r, \mu_f, H_{T,2}/2)] \quad (6.1)$$

where $\frac{d\sigma}{d(H_{T,2}/2)}$ is the differential inclusive jet production cross-section as a function of $H_{T,2}/2$, μ_r and μ_f are the renormalization and factoriza-

tion scales set equal to $H_{T,2}/2$, $\alpha_S^2(\mu_r)\hat{X}^{(0)}(\mu_f, H_{T,2}/2)$ is the leading order (LO) contribution to the differential inclusive jet production cross-section and $\alpha_S^3(\mu_r)\hat{X}^{(0)}(\mu_f, H_{T,2}/2)K1(\mu_r, \mu_f, H_{T,2}/2)$ is the next-to-leading order (NLO) contribution. Equation 6.1 shows how the inclusive jet production cross-section varies with $\alpha_S(\mu_r)$.

6.1 Sensitivity of Measurements to $\alpha_s(M_Z)$

For a fixed choice of μ_r and μ_f , different input values of $\alpha_s(M_Z)$ to a PDF set will lead to different theory predictions of the differential cross-section distribution. This will give an estimate of the sensitivity of the theory predictions to the varying input value of $\alpha_s(M_Z)$. A comparison of the measured spectrum with the theory predictions obtained using all $\alpha_s(M_Z)$ inputs will give a hint of the input value of $\alpha_s(M_Z)$ for which the theory distribution has the closest matching with data. In this section, the sensitivity of the inclusive differential jet event cross-sections and cross-section ratio, R_{32} to varying input values of $\alpha_s(M_Z)$ for different PDF sets is demonstrated by plotting the ratios of data over theory predictions with central value of $\alpha_s(M_Z)$.

Figures 6.1, 6.2 and 6.3 present the ratio of data to the theory predictions, corrected for NP effects, for all variations in $\alpha_s(M_Z)$ available for the PDF sets CT10, CT14, MSTW2008, MMHT2014 and NNPDF2.3 at NLO evolution order as specified in Table 5.1, for inclusive 2-jet event cross-sections, inclusive 3-jet events cross-sections and ratio R_{32} respectively. The $\alpha_s(M_Z)$ value is varied in the range 0.112-0.127, 0.111-0.123, 0.110-0.130, 0.108-0.128 and 0.114-0.124 in steps of 0.001 for the CT10, CT14, MSTW2008, MMHT2014 and NNPDF2.3PDF sets, respectively. The error bars correspond to the total experimental uncertainty derived as quadratic sum from all uncertainty sources. The theory predictions are also corrected for EW effects for inclusive 2-jet events cross-section. A small slope increasing with $H_{T,2}/2$

is visible for most PDFs in both cross-sections. This effect is largely cancelled in the cross-section ratio. R_{32} exhibits a flat behaviour with respect to the predictions for all five PDF sets in the whole range of $H_{T,2}/2$ up to 1680 GeV. Therefore, these data can be used to determine the strong coupling constant, although only up to 1 TeV for the cross-sections as long as electroweak corrections are not taken into account.

Moreover, the different sensitivity to $\alpha_s(M_Z)$ caused by the leading power in α_s in the expansion of the 2-jet inclusive ($\propto \alpha_s^2$) and the 3-jet inclusive cross-section ($\propto \alpha_s^3$), and their ratio ($\propto \alpha_s^1$) is clearly visible from the spread between the calculations for the smallest and largest value of $\alpha_s(M_Z)$ within the same PDF set when passing through Figures 6.1–6.3. This also demonstrates the potential of ratios R_{mn} with $m-n > 1$.

6.2 Determination of $\alpha_s(M_Z)$

As discussed in the previous section, the measured inclusive 2-jet and 3-jet event cross-sections and their ratio R_{32} can be used for a determination of the strong coupling constant $\alpha_s(M_Z)$. To extract the value of $\alpha_s(M_Z)$, a general fit procedure [45, 47] has been followed and is described in the following section.

6.2.1 Fitting Procedure

The value of $\alpha_s(M_Z)$ is determined by minimizing the chi-square (χ^2) between the experimental measurement and the theoretical predictions. The χ^2 is defined as:

$$\chi^2 = M^T C^{-1} M \tag{6.2}$$

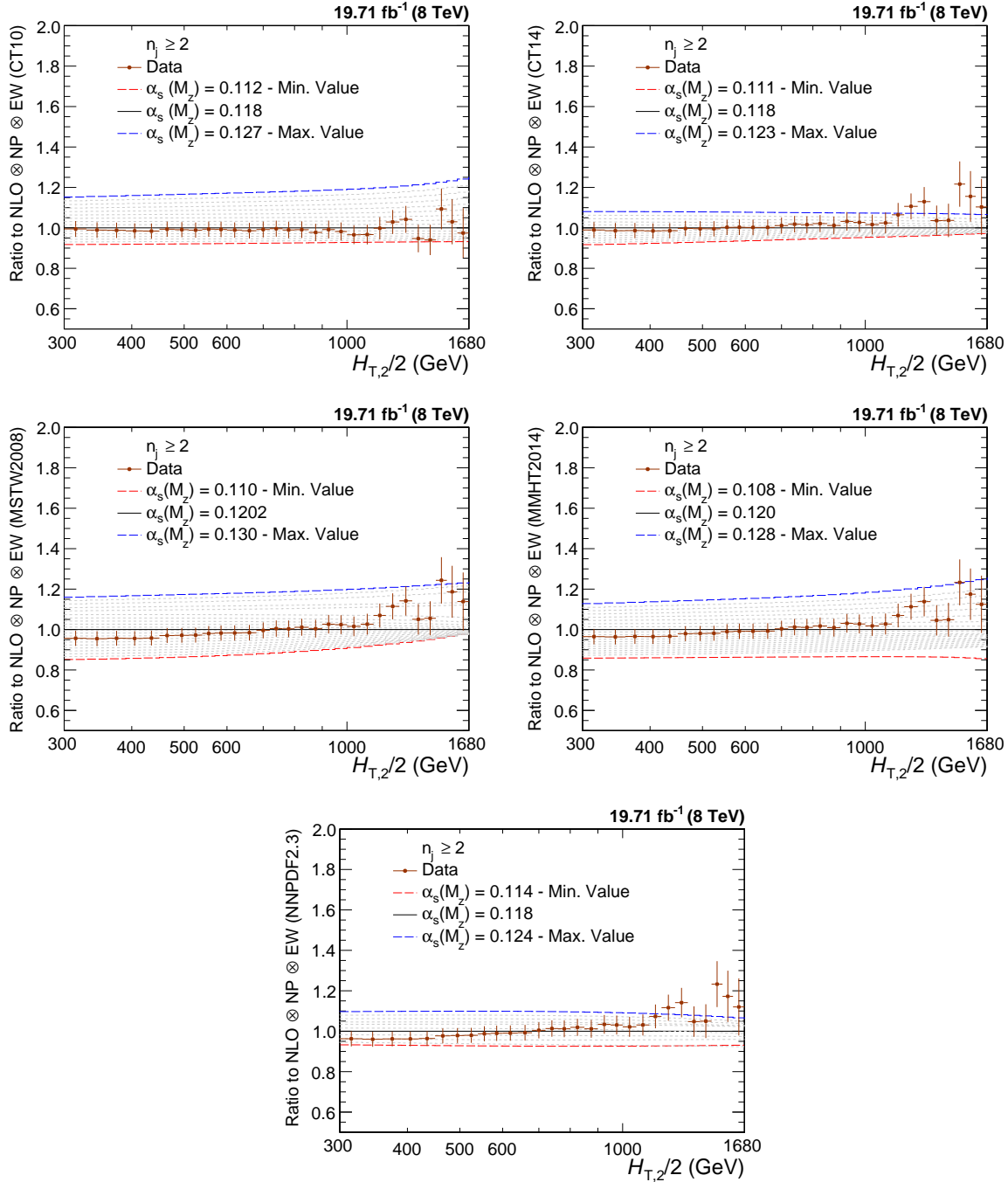


Figure 6.1: Ratio of the inclusive 2-jet differential cross-section to theory predictions using the CT10 (top left), the CT14 (top right), the MSTW2008 (middle left), the MMHT2014 (middle right) and NNPDF2.3 (bottom) NLO PDF sets for a series of values of $\alpha_s(M_Z)$. The $\alpha_s(M_Z)$ value is varied in the range 0.112-0.127, 0.111-0.123, 0.110-0.130 and 0.108-0.128 in steps of 0.001 for the CT10, CT14, MSTW2008, MMHT2014 and NNPDF2.3 NLO PDF sets, respectively. The error bars correspond to the total experimental uncertainty. The theory predictions are corrected for non-perturbative (NP) and electroweak (EW) effects.

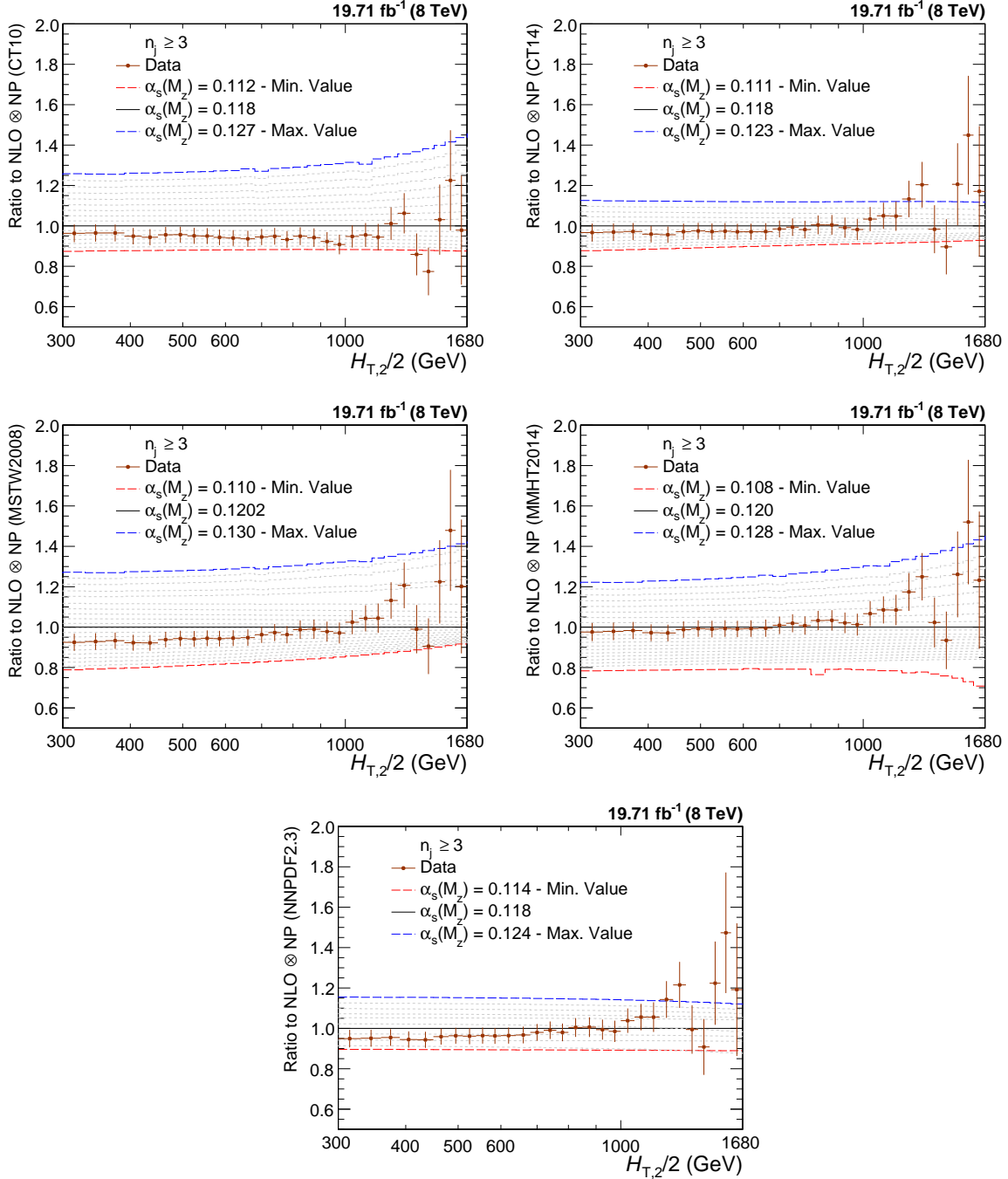


Figure 6.2: Ratio of the inclusive 3-jet differential cross-section to theory predictions using the CT10 (top left), the CT14 (top right), the MSTW2008 (middle left), the MMHT2014 (middle right) and NNPFD2.3 (bottom) NLO PDF sets for a series of values of $\alpha_s(M_Z)$. The $\alpha_s(M_Z)$ value is varied in the range 0.112-0.127, 0.111-0.123, 0.110-0.130, 0.108-0.128 and 0.114-0.124 in steps of 0.001 for the CT10, CT14, MSTW2008, MMHT2014 and NNPFD2.3 NLO PDF sets, respectively. The error bars correspond to the total experimental uncertainty. The theory predictions are corrected for non-perturbative (NP) effects.

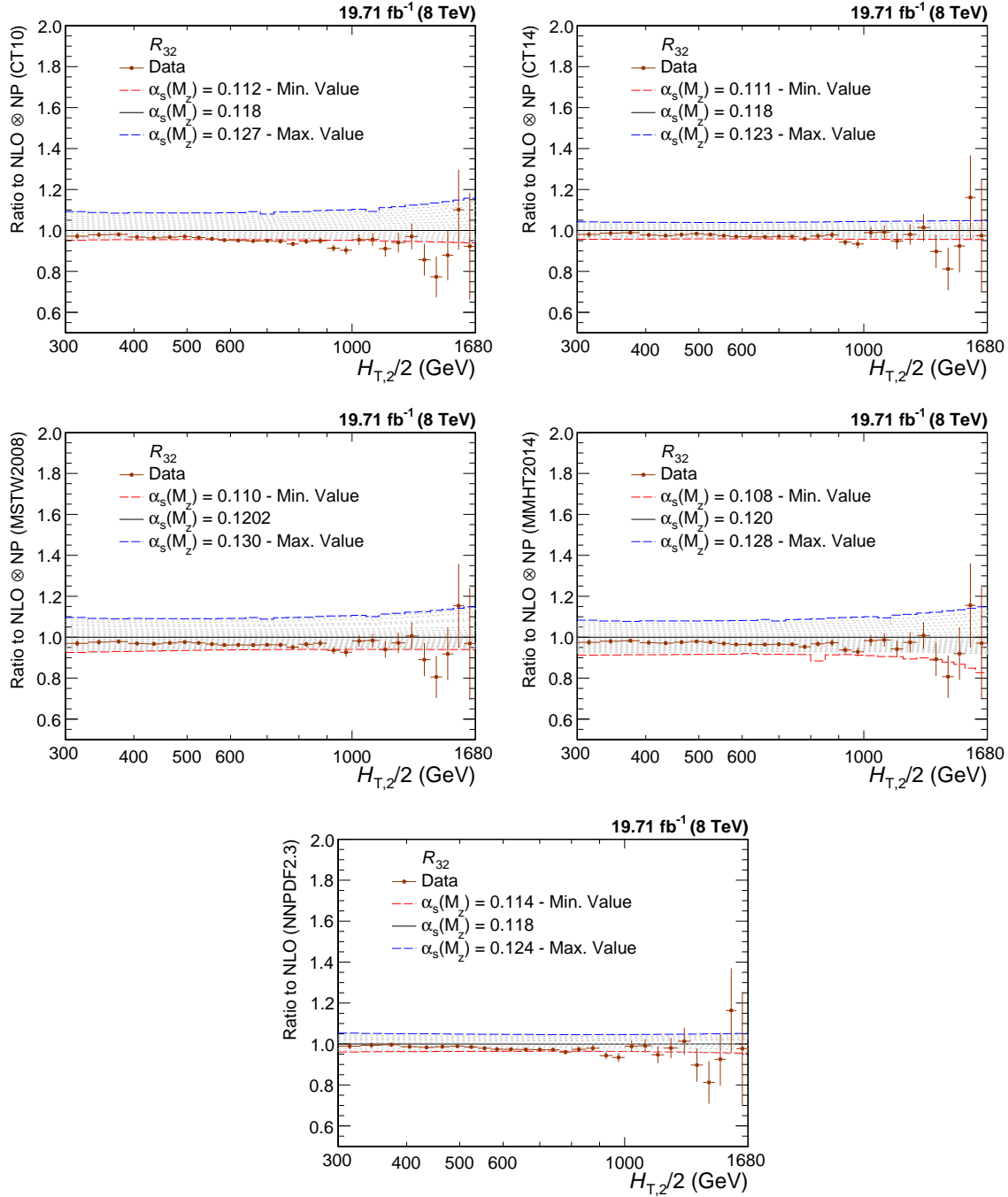


Figure 6.3: Ratio of the cross-section ratio, R_{32} to theory predictions using the CT10 (top left), the CT14 (top right), the MSTW2008 (middle left), the MMHT2014 (middle right) and NNPDF2.3 (bottom) NLO PDF sets for a series of values of $\alpha_s(M_Z)$. The $\alpha_s(M_Z)$ value is varied in the range 0.112-0.127, 0.111-0.123, 0.110-0.130, 0.108-0.128 and 0.114-0.124 in steps of 0.001 for the CT10, CT14, MSTW2008, MMHT2014 and NNPDF2.3 NLO PDF sets, respectively. The error bars correspond to the total experimental uncertainty. The theory predictions are corrected for non-perturbative (NP) effects.

where M is the vector of the differences between the data (D^i) and the theoretical values (T^i) in each bin i ,

$$M^i = D^i - T^i \quad (6.3)$$

and C is the covariance matrix including all experimental uncertainties as described in Sec. 4.6 and some theoretical uncertainties discussed in Sec. 5.2. The covariance matrix $C = C_{\text{exp}} + C_{\text{theo}}$ is defined as the sum of covariances of experimental and theoretical sources of uncertainty as follows :

$$C_{\text{exp}} = \text{Cov}^{\text{ExpStat}} + \sum \text{Cov}^{\text{JEC}} + \text{Cov}^{\text{Unfolding}} + \text{Cov}^{\text{Lumi}} + \text{Cov}^{\text{Residual}} \quad (6.4)$$

$$C_{\text{theo}} = \text{Cov}^{\text{TheoStat}} + \text{Cov}^{\text{NP}} + \text{Cov}^{\text{PDF}} \quad (6.5)$$

where the labelled covariance matrices account for the following effects:

- $\text{Cov}^{\text{ExpStat}}$: statistical uncertainty of the data including correlations introduced by the unfolding
- Cov^{JEC} : the jet energy corrections (JEC) systematic uncertainty
- $\text{Cov}^{\text{Unfolding}}$: the unfolding systematic uncertainty including the resolution (JER) and model dependence
- Cov^{Lumi} : the luminosity uncertainty
- $\text{Cov}^{\text{Residual}}$: a residual uncorrelated systematic uncertainty summarizing individual causes such as small trigger and identification inefficiencies, time dependence of the jet p_T resolution, and uncertainty on the trigger prescale factors
- $\text{Cov}^{\text{TheoStat}}$: statistical uncertainty caused by numerical integrations in the cross-section computations

- Cov^{NP} : the systematic uncertainty of the non-perturbative (NP) corrections
- Cov^{PDF} : the PDF uncertainties

While taking the differences between theory and data, the treatment of experimental and theoretical systematic uncertainties is crucial. The Unfolding, JEC, Lumi and PDF and NP systematic uncertainties are treated as 100% correlated among $H_{\text{T},2}/2$ bins. If δ_i is the total uncertainty on the differential cross-section, for the i -th $H_{\text{T},2}/2$ bin, for any of these fully correlated sources, then the i, j -th element of the corresponding covariance matrix is given by $\text{COV}_{ij} = \delta_i \times \delta_j$. The JEC, unfolding, and luminosity uncertainties are treated as multiplicative to avoid the statistical bias that arises when estimating uncertainties from data. In fits of the ratio R_{32} , the luminosity and residual uncorrelated uncertainties cancel completely. Partial cancellations between the other sources of uncertainty are taken into account in the fit.

The evaluation of PDF uncertainty depends on the individual PDF set as already discussed in Sec. 5.2.2. The PDF covariance matrix construction varies among different PDF sets. The CT10, CT14, MMHT2014 and MSTW2008 NLO PDF sets employ the eigenvector method to evaluate the PDF uncertainties as explained in Sec. 5.2.2. The number of eigenvectors (N_{ev}) with two PDF members per eigenvector for CT10, CT14, MMHT2014 and MSTW2008 NLO PDF sets are 26, 28, 25 and 20, respectively. The NNPDF2.3 PDF set comes with hundred different replicas (N_{rep}) instead of different eigenvectors, as for CT10 or CT14 PDF sets. The mean uncertainty is calculated as average uncertainty from 100 different replicas. Following the prescription given in [55], the PDF uncertainty is calculated as :

$$(\Delta X)^2 = \frac{1}{N_{\text{rep}} - 1} \sum_{k=1}^{N_{\text{rep}}} [X_k - \langle X_k \rangle]^2 \quad (6.6)$$

where ΔX is the uncertainty on predicted differential cross-section, X_k is the

differential cross-section for k -th replica and $\langle X_k \rangle$ is the average differential cross-section from all the replicas.

Scale uncertainties of the pQCD predictions are taken into account by employing the offset method, i.e. by performing separate fits with varying scale factors as described in the Sec. 5.2.1. The largest upwards and downwards deviations from the default factors are defined as the uncertainty. At NLO such scale variations predominantly lead to smaller cross-sections and also a smaller ratio R_{32} as visible in Fig. 5.5. As a consequence the scale uncertainty in fits is equally asymmetric, where smaller cross-sections or ratios are compensated by an increase in the fitted value for $\alpha_s(M_Z)$.

6.2.2 Fit Results

To determine the value of the strong coupling constant at the scale of the Z boson mass $\alpha_s(M_Z)$, fits to the differential inclusive 2-jet and 3-jet events cross-sections are performed using five different NLO PDF sets : CT10, CT14, MSTW2008, MMHT2014 and NNPDF2.3. The range in $H_{T,2}/2$ is restricted to be between 300 GeV and 1 TeV to avoid the region close to the minimal p_T threshold of 150 GeV for each jet at low p_T and the onset of electroweak effects at high $H_{T,2}/2$, which are available for the dijet case only. The $\alpha_s(M_Z)$ results obtained from a simultaneous fit to all 19 $H_{T,2}/2$ bins in the above mentioned range are reported in Table 6.1. For comparison, a simultaneous fit to both cross-sections ignoring any correlations, and a fit to the cross-section ratio R_{32} , fully accounting for correlations is also performed and the results are tabulated in Table 6.2. The electroweak effects are assumed to cancel in the ratio as do the luminosity and the uncorrelated uncertainty.

All cross-section fits give compatible values for $\alpha_s(M_Z)$ in the range of 0.115-0.118 whereas for the ratio R_{32} somewhat smaller values are obtained. But for individual cross-sections, χ^2/n_{dof} values are small as compared to the cross-section

ratio R_{32} . A possible explanation is an overestimation of the residual uncorrelated uncertainty of 1% that is cancelled for R_{32} . If the fits are repeated with an assumed uncertainty of 0.25% instead, the χ^2/n_{dof} values lie around unity while the $\alpha_s(M_Z)$ values are still compatible with the previous results but with slightly reduced uncertainties.

Table 6.1: Determination of $\alpha_s(M_Z)$ from the inclusive 2-jet and 3-jet event cross-sections using five PDF sets at NLO. Only total uncertainties without scale variations are quoted. The results are obtained from a simultaneous fit to all 19 $H_{T,2}/2$ bins in the restricted range of $0.3 < H_{T,2}/2 < 1.0$ TeV.

PDF set	Inclusive 2-jets			Inclusive 3-jets		
	$\alpha_s(M_Z)$	$\pm\Delta\alpha_s(M_Z)$	χ^2/n_{dof}	$\alpha_s(M_Z)$	$\pm\Delta\alpha_s(M_Z)$	χ^2/n_{dof}
CT10	0.1174	0.0032	3.0/18	0.1169	0.0027	5.4/18
CT14	0.1160	0.0035	3.5/18	0.1159	0.0031	6.1/18
MSTW2008	0.1159	0.0025	5.3/18	0.1161	0.0021	6.7/18
MMHT2014	0.1165	0.0034	5.9/18	0.1166	0.0025	7.1/18
NNPDF2.3	0.1183	0.0025	9.7/18	0.1179	0.0021	9.1/18

Table 6.2: Determination of $\alpha_s(M_Z)$ from the inclusive 2-jet and 3-jet event cross-sections simultaneously and from their ratio R_{32} using five PDF sets at NLO. Only total uncertainties without scale variations are quoted. The results are obtained from a simultaneous fit to all 38 (left) and 19 (right) $H_{T,2}/2$ bins in the restricted range of $0.3 < H_{T,2}/2 < 1.0$ TeV. For comparison, correlations between the two cross-sections are neglected in the simultaneous fit on the left, but fully taken into account in the ratio fit on the right.

PDF set	Inclusive 2- and 3-jets			R_{32}		
	$\alpha_s(M_Z)$	$\pm\Delta\alpha_s(M_Z)$	χ^2/n_{dof}	$\alpha_s(M_Z)$	$\pm\Delta\alpha_s(M_Z)$	χ^2/n_{dof}
CT10	0.1170	0.0026	8.2/37	0.1141	0.0028	19./18
CT14	0.1161	0.0029	9.1/37	0.1139	0.0032	15./18
MSTW2008	0.1161	0.0021	11./37	0.1150	0.0023	21./18
MMHT2014	0.1168	0.0025	11./37	0.1142	0.0022	19./18
NNPDF2.3	0.1188	0.0019	15./37	0.1184	0.0021	12./18

To investigate how the electroweak (EW) corrections affect the fit results for $\alpha_s(M_Z)$, the range in $H_{T,2}/2$ is extended to $0.3 < H_{T,2}/2 < 1.68$ TeV. $\alpha_s(M_Z)$ values are obtained from fits to the inclusive 2-jet event cross-section in this range with or without EW correction factors and the results are presented in Table 6.3. The largest impact is a reduction in χ^2/n_{dof} , which indicates a better agreement when

EW effects are included. In addition, a tendency to slightly smaller $\alpha_s(M_Z)$ values is observed without the EW corrections. For the ratio R_{32} , it is expected that these effects are much reduced.

Table 6.3: Determination of $\alpha_s(M_Z)$ from the inclusive 2-jet event cross-section using five PDF sets at NLO without (left) and with (right) electroweak (EW) corrections. Only total uncertainties without scale variations are quoted. The results are obtained from a simultaneous fit to all 29 $H_{T,2}/2$ bins in the range of $0.3 < H_{T,2}/2 < 1.68$ TeV.

PDF set	without EW			with EW		
	$\alpha_s(M_Z)$	$\pm\Delta\alpha_s(M_Z)$	χ^2/n_{dof}	$\alpha_s(M_Z)$	$\pm\Delta\alpha_s(M_Z)$	χ^2/n_{dof}
CT10	0.1163	0.0034	15./28	0.1165	0.0032	14./28
CT14	0.1137	0.0033	24./28	0.1144	0.0033	17./28
MSTW2008	0.1093	0.0028	27./28	0.1133	0.0023	19./28
MMHT2014	0.1127	0.0032	32./28	0.1141	0.0032	21./28
NNPDF2.3	0.1162	0.0024	31./28	0.1168	0.0024	23./28

From Fig. 6.3 follows that only the PDF sets MSTW2008 and MMHT2014 provide a large enough range in $\alpha_s(M_Z)$ values to ensure fits without extrapolation. The other three PDF sets are at the limit such that reliable fits cannot be performed for all scale settings and/or bins in scale $Q = H_{T,2}/2$. Since many systematic uncertainties cancel completely or partially in the cross-section ratio R_{32} as compared to the individual cross-sections, R_{32} is used mainly to determine the value of $\alpha_s(M_Z)$. Table 6.4 give the complete results for MSTW2008 and MMHT2014 for the full range in $H_{T,2}/2$ of 300 GeV up to 1.68 TeV along with the corresponding components of PDF, scale, NP and total experimental except scale uncertainties are shown. In contrast to fits at NLO using cross-sections where the scale uncertainty recipe usually leads to a very asymmetric behaviour with larger downward uncertainties in the case, this is inverted for the fits to the cross-section ratio R_{32} . The scale uncertainty is the most dominant source of total uncertainty on $\alpha_s(M_Z)$. These values are determined with the central renormalization and factorization scales i.e. $\mu_r = \mu_f = H_{T,2}/2$. The values are also determined for the six scale factor combinations for the two PDF sets MSTW2008 and MMHT2014 and results are shown in Table 6.5.

The uncertainty decomposition for $\alpha_s(M_Z)$ determined from cross-section ratio R_{32} is performed in four sub-ranges of $H_{T,2}/2$ and the results are shown in Table 6.6. The statistical uncertainty of the NLO computation is negligible in comparison to any of the other sources of uncertainty. Electroweak corrections, significant only at high $H_{T,2}/2$, are assumed to cancel between the numerator and denominator.

Using the MSTW2008 PDF set, which dates from before the LHC start, the strong coupling constant finally is determined to

$$\begin{aligned}\alpha_s(M_Z) &= 0.1150 \pm 0.0010 (\text{exp}) \pm 0.0013 (\text{PDF}) \pm 0.0015 (\text{NP}) {}^{+0.0050}_{-0.0000} (\text{scale}) \\ &= 0.1150 \pm 0.0023 (\text{all except scale}) {}^{+0.0050}_{-0.0000} (\text{scale})\end{aligned}\tag{6.7}$$

The MMHT2014 PDF set, although using LHC jet data to determine the PDF parameters, leads to a very similar result of

$$\begin{aligned}\alpha_s(M_Z) &= 0.1142 \pm 0.0010 (\text{exp}) \pm 0.0013 (\text{PDF}) \pm 0.0014 (\text{NP}) {}^{+0.0049}_{-0.0006} (\text{scale}) \\ &= 0.1142 \pm 0.0022 (\text{all except scale}) {}^{+0.0049}_{-0.0006} (\text{scale})\end{aligned}\tag{6.8}$$

6.3 Running of the Strong Coupling Constant

The value of the strong coupling constant α_s depends on the energy scale Q and it decreases with the increase of scale Q . To study this dependence, the determination of α_s is carried out at different energies. The procedure to extract $\alpha_s(Q)$ is same as the one followed for the $\alpha_s(M_Z)$. To have different energy scales, the fitted $H_{T,2}/2$ range 300 - 1680 GeV is divided into four different sub-ranges as shown by the first column in Table 6.7. Each of the $H_{T,2}/2$ range is associated with a scale Q , which

Table 6.4: Determination of $\alpha_s(M_Z)$ from the ratio R_{32} using the two most compatible PDF sets MSTW2008 and MMHT2014 at NLO along with the corresponding components of PDF, scale, NP and total (except scale) experimental uncertainties. The results are obtained from a simultaneous fit to all 29 $H_{T,2}/2$ bins in the full range of $0.3 < H_{T,2}/2 < 1.68$ TeV.

PDF set	$\alpha_s(M_Z)$	exp	PDF	NP	all exc. scale	scale	χ^2/n_{dof}
MSTW2008	0.1150	± 0.0010	± 0.0013	± 0.0015	± 0.0023	$^{+0.0050}_{-0.0000}$	26./28
MMHT2014	0.1142	± 0.0010	± 0.0013	± 0.0014	± 0.0022	$^{+0.0049}_{-0.0006}$	24./28

Table 6.5: Determination of $\alpha_s(M_Z)$ from the ratio R_{32} in the $H_{T,2}/2$ range from 0.3 up to 1.68 TeV at the central scale and for the six scale factor combinations for the two PDF sets MSTW2008 and MMHT2014.

$\mu_r/H_{T,2}/2$	$\mu_f/H_{T,2}/2$	MSTW2008		MMHT2014	
		$\alpha_s(M_Z)$	χ^2/n_{dof}	$\alpha_s(M_Z)$	χ^2/n_{dof}
1	1	0.1150	26./28	0.1142	24./28
1/2	1/2	0.1165	77./28	0.1160	73./28
2	2	0.1200	18./28	0.1191	18./28
1/2	1	0.1150	53./28	0.1136	48./28
1	1/2	0.1150	30./28	0.1142	28./28
1	2	0.1155	23./28	0.1147	22./28
2	1	0.1180	19./28	0.1175	19./28

Table 6.6: Uncertainty decomposition for $\alpha_s(M_Z)$ from the determination of α_s from the jet event rate R_{32} in bins of $H_{T,2}/2$. The statistical uncertainty of the NLO computation is negligible in comparison to any of the other sources of uncertainty. Electroweak corrections, significant only at high $H_{T,2}/2$, are assumed to cancel between the numerator and denominator.

$H_{T,2}/2$ (GeV)	MSTW2008					MMHT2014				
	$\alpha_s(M_Z)$	exp	PDF	NP	scale	$\alpha_s(M_Z)$	exp	PDF	NP	scale
300-420	0.1157	± 0.0015	± 0.0014	± 0.0019	$^{+0.0053}_{-0.0000}$	0.1158	± 0.0014	± 0.0010	± 0.0019	$^{+0.0052}_{-0.0000}$
420-600	0.1153	± 0.0011	± 0.0014	± 0.0018	$^{+0.0057}_{-0.0000}$	0.1154	± 0.0011	± 0.0012	± 0.0017	$^{+0.0056}_{-0.0000}$
600-1000	0.1134	± 0.0013	± 0.0016	± 0.0019	$^{+0.0052}_{-0.0000}$	0.1140	± 0.0012	± 0.0012	± 0.0018	$^{+0.0045}_{-0.0000}$
1000-1680	0.1147	± 0.0029	± 0.0017	± 0.0018	$^{+0.0063}_{-0.0011}$	0.1154	± 0.0025	± 0.0014	± 0.0015	$^{+0.0056}_{-0.0011}$
300-1680	0.1150	± 0.0010	± 0.0013	± 0.0015	$^{+0.0050}_{-0.0000}$	0.1142	± 0.0010	± 0.0013	± 0.0014	$^{+0.0049}_{-0.0006}$

is the differential cross-section weighted average $H_{T,2}/2$ scale from the inclusive 2-jet calculations and integrated over all the measured $H_{T,2}/2$ bins contributing to that given $H_{T,2}/2$ range. Let N_{bin}^j be the total number of measured $H_{T,2}/2$ bins contributing to the j -th $H_{T,2}/2$ range, then the corresponding scale Q_j , shown in second column of Table 6.7, is calculated as :

$$Q_j = \frac{\sum_{i=1}^{N_{bin}^j} H_{T,2}^i \left[\frac{d\sigma}{d(H_{T,2}/2)} \right]^i}{\sum_{i=1}^{N_{bin}^j} \left[\frac{d\sigma}{d(H_{T,2}/2)} \right]^i} \quad (6.9)$$

The value of $\alpha_s(M_Z)$ is extracted in each $H_{T,2}/2$ range. These extracted $\alpha_s(M_Z)$ values are evolved to the corresponding values $\alpha_s(Q)$ and are quoted in Table 6.7 along with the extracted $\alpha_s(M_Z)$ values and the total uncertainty. The evolution is performed for five flavours at 2-loop order with the RUNDEC program [56, 57]. The obtained $\alpha_s(Q)$ points (black solid circles) are shown as a function of scale Q in Fig. 6.4. The black solid line and the yellow uncertainty band are evolved using $\alpha_s(M_Z) = 0.1150 \pm 0.0023$ (all except scale) $^{+0.0050}_{-0.0000}$ (scale) obtained using MSTW2008 NLO PDF set. The world average [58] (dashed line) and results from other measurements of the CMS [17, 26, 45–47], ATLAS [48], D0 [49, 50], H1 [51, 52], and ZEUS [53] experiments are also imposed. The current measurement is in very good agreement within the uncertainty with other results obtained by previous experiments as well as with the world average value of $\alpha_s(M_Z) = 0.1181 \pm 0.0011$ derived in Ref. [58].

Table 6.7: Evolution of the strong coupling constant between the scale of the Z boson mass and the cross-section averaged $H_{T,2}/2$ scale $\langle Q \rangle$ for the separate determinations in each respective fit range. The evolution is performed for five flavours at 2-loop order with the RUNDEC program [56, 57].

$H_{T,2}/2$ (GeV)	$\langle Q \rangle$ (GeV)	$\alpha_s(M_Z)$	$\alpha_s(Q)$	No. of data points	χ^2/n_{dof}
300-420	340	$0.1157^{+0.0060}_{-0.0030}$	$0.0969^{+0.0041}_{-0.0021}$	4	2.8/3
420-600	476	$0.1153^{+0.0062}_{-0.0025}$	$0.0928^{+0.0039}_{-0.0016}$	6	6.1/5
600-1000	685	$0.1134^{+0.0059}_{-0.0028}$	$0.0879^{+0.0035}_{-0.0017}$	9	7.1/8
1000-1680	1114	$0.1147^{+0.0074}_{-0.0040}$	$0.0841^{+0.0039}_{-0.0021}$	10	5.4/9

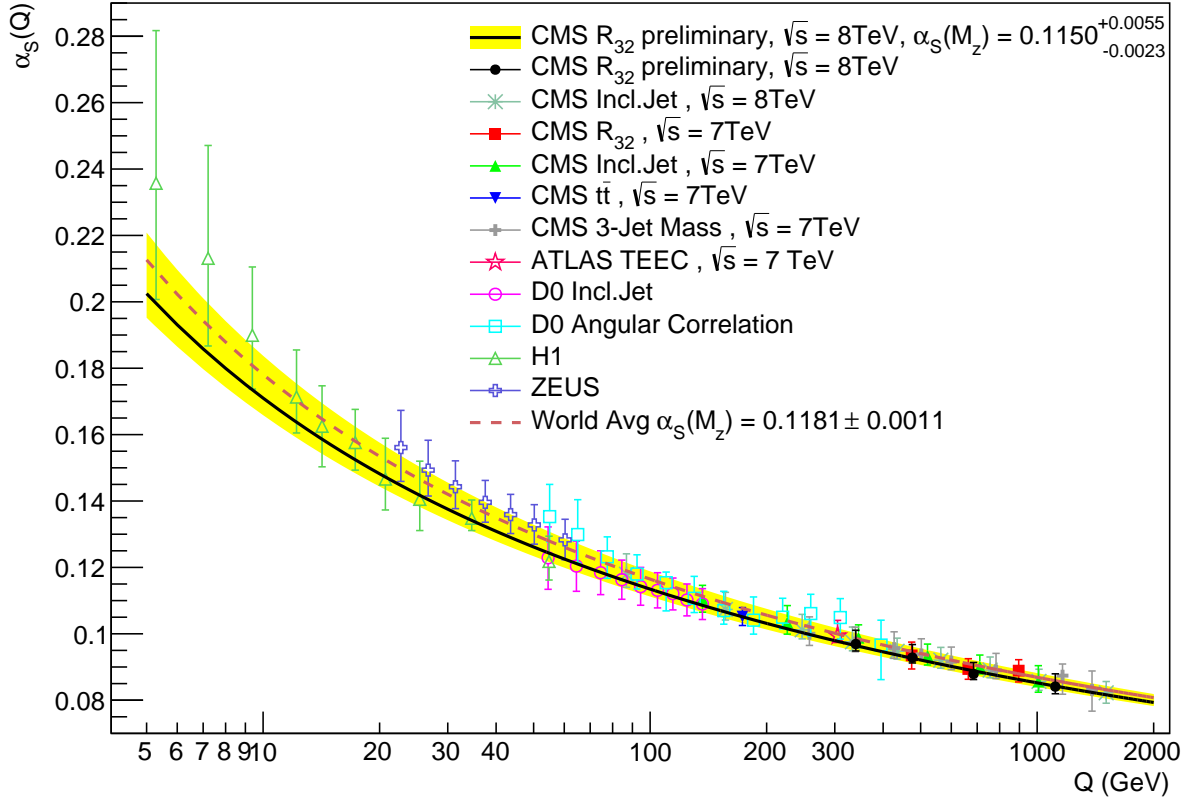


Figure 6.4: The running $\alpha_s(Q)$ as a function of the scale Q is shown as obtained by using the MSTW2008 NLO PDF set. The solid line and the uncertainty band are drawn by evolving the extracted $\alpha_s(M_Z)$ values using the 2-loop 5-flavour renormalization group equations as implemented in RUNDEC [56, 57]. The dashed line represents the evolution of the world average [58] and the black circles correspond to the $\alpha_s(Q)$ determinations presented in Table 6.7. Results from other measurements of CMS [17, 26, 45–47], ATLAS [48], D0 [49, 50], H1 [51, 52], and ZEUS [53] are superimposed.

Chapter 7

Summary

Inclusive jet production cross-section measured precisely as a function of jet transverse momentum is one of the important observables in understanding physics at hadron colliders. It provides the essential information about the structure of proton through parton distribution functions (PDFs) and the precise measurement of the strong coupling constant α_s . The value of the strong coupling constant at the scale of the Z boson mass $\alpha_s(M_Z)$ can be determined using cross-section ratio instead of individual cross-sections because many theoretical and experimental uncertainties (i.e. uncertainties due to luminosity, scale dependence, PDF dependence etc.) may cancel between numerator and denominator.

In this thesis, a measurement of the inclusive 2-jet and 3-jet event cross-sections as well as the cross-section ratio R_{32} has been presented. The data sample has been collected from proton-proton collisions recorded with the CMS detector at a centre-of-mass energy of 8 TeV corresponding to an integrated luminosity of 19.7 fb^{-1} . The jets are reconstructed with the anti- k_t clustering algorithm for a jet size parameter $R = 0.7$. The inclusive 2-jet and 3-jet event cross-sections are measured differentially as a function of the average transverse momentum of the two leading jets, referred as $H_{T,2}/2$. The ratio R_{32} is obtained by dividing the differential cross-sections of inclusive 3-jet events to that of inclusive 2-jet one in each bin of $H_{T,2}/2$. An

appropriate selection criteria has been designed for choosing the best events for analysis. The measurements are performed at a central rapidity of $|y| < 2.5$ in a range of $0.3 < H_{T,2}/2 < 2.0$ TeV for inclusive 2-jet event cross-sections and $0.3 < H_{T,2}/2 < 1.68$ TeV for inclusive 3-jet event cross-sections and ratio R_{32} .

The measured cross-sections after correcting for detector effects by using an iterative unfolding procedure are compared to the perturbative QCD predictions computed, using NLOJET++ program, at next-to-leading order (NLO) accuracy and complemented with non-perturbative (NP) corrections that are important at low $H_{T,2}/2$. The data are found to be well described by NLO calculations. The upwards trend observed in the inclusive 2-jet and 3-jet data at high $H_{T,2}/2$ in comparison to the prediction at NLO QCD, is explained by the onset of electroweak (EW) corrections in the 2-jet case. For the 3-jet event cross-sections these corrections have not yet been computed yet. In the 3-jet to 2-jet cross-section ratio R_{32} , the EW corrections are assumed to cancel. In fact, NLO QCD provides an adequate description of R_{32} in the accessible range of $H_{T,2}/2$. In contrast, leading order (LO) tree-level Monte Carlo (MC) predictions obtained using MADGRAPH5 event generator interfaced to PYTHIA6 exhibit significant deviations. The sources of experimental and theoretical uncertainties are studied in details. The experimental uncertainty ranges from 4 to 32% for inclusive 2-jet event cross-sections, from 4 to 28% for 3-jet event cross-sections and from 1 to 28% for cross-section ratio R_{32} . It is dominated by the uncertainty due to the jet energy corrections (JEC) at lower $H_{T,2}/2$ values and by statistical uncertainty at higher $H_{T,2}/2$ values. The theoretical uncertainty ranges from 3 to 30% and 5 to 34% for inclusive 2-jet and 3-jet event cross-sections respectively and from 3 to 11% for ratio R_{32} . The PDF uncertainty derived using the CT10-NLO PDF set is the dominant source of theoretical uncertainty.

The inclusive multijet cross-sections being proportional to the powers of the

strong coupling constant α_s ($\sigma_{n\text{-jet}} \propto \alpha_s^n$) are used to determine the strong coupling constant at the scale of the Z boson mass $\alpha_s(M_Z)$. In cross-section ratio R_{32} which is proportional to α_s , many uncertainties and PDF dependencies largely cancel and hence becomes the better tool to extract the value of $\alpha_s(M_Z)$. In this thesis, a fit of the ratio of the 3-jet over 2-jet event cross-section R_{32} in the range $0.3 < H_{T,2}/2 < 1.68$ TeV using the MSTW2008 PDF set gives :

$$\begin{aligned}\alpha_s(M_Z) &= 0.1150 \pm 0.0010 (\text{exp}) \pm 0.0013 (\text{PDF}) \pm 0.0015 (\text{NP})^{+0.0050}_{-0.0000} (\text{scale}) \\ &= 0.1150 \pm 0.0023 (\text{all except scale})^{+0.0050}_{-0.0000} (\text{scale})\end{aligned}$$

Very similar results are obtained using the MMHT2014 PDF set which gives :

$$\begin{aligned}\alpha_s(M_Z) &= 0.1142 \pm 0.0010 (\text{exp}) \pm 0.0013 (\text{PDF}) \pm 0.0014 (\text{NP})^{+0.0049}_{-0.0006} (\text{scale}) \\ &= 0.1142 \pm 0.0022 (\text{all except scale})^{+0.0049}_{-0.0006} (\text{scale})\end{aligned}$$

The equally compatible values of $\alpha_s(M_Z)$ are determined with separate fits to the inclusive 2-jet and 3-jet event cross-sections provided the range in $H_{T,2}/2$ is restricted to $0.3 < H_{T,2}/2 < 1.0$ TeV. The extracted $\alpha_s(M_Z)$ values in sub-ranges of $H_{T,2}/2$ are evolved to corresponding $\alpha_s(Q)$ along with the error bars at different scales Q . The current measurement of $\alpha_s(M_Z)$ and the running of $\alpha_s(Q)$ as a function of Q is in agreement with the world average value of $\alpha_s(M_Z) = 0.1181 \pm 0.0011$ [58] and already existing determinations performed by the CMS and other experiments.

The inclusion of the EW corrections in inclusive 2-jet event cross-sections become relevant at $H_{T,2}/2$ beyond 1 TeV. Their availability for 3-jet one and hence cross-section ratio R_{32} can improve the precision of the measurement of $\alpha_s(M_Z)$. Also as the theoretical calculations will be available for inclusive 4-jet event cross-sections, the various cross-section ratios such as $R_{43} \propto \alpha_s^1$ and $R_{42} \propto \alpha_s^2$ can be measured to extract the value of the strong coupling constant more precisely. Currently LHC is running at high center-of-mass energy of 13 TeV delivering a higher instantaneous luminosity and this makes possible to extend the accessible phase space and perform the measurements with more accuracy.

Appendix A

A.1 Cross-section Ratio, R_{32}

Table A.1: Differential cross-sections ($\times 10^{-3}(\text{pb/GeV})$) and cross-section ratio R_{32} at detector level in each bin of $H_{T,2}/2$, along with statistical uncertainty (in %).

Bin	2-jet cross-section	Stat. unc.	3-jet cross-section	Stat. unc.	Ratio R_{32}	Stat. unc.
300 - 330	29772.726	0.211	2640.629	0.707	0.089	+0.665 -0.661
330 - 360	16792.917	0.231	1773.485	0.704	0.106	+0.523 -0.521
360 - 390	9889.326	0.182	1176.544	0.526	0.119	+0.485 -0.483
390 - 420	5976.777	0.179	778.034	0.492	0.130	+0.206 -0.206
420 - 450	3731.760	0.067	522.624	0.180	0.140	+0.167 -0.167
450 - 480	2398.741	0.084	357.622	0.217	0.149	+0.201 -0.200
480 - 510	1570.192	0.104	246.051	0.262	0.157	+0.241 -0.241
510 - 540	1048.665	0.127	171.080	0.314	0.163	+0.288 -0.287
540 - 570	713.042	0.154	119.566	0.376	0.168	+0.344 -0.343
570 - 600	490.776	0.186	84.798	0.447	0.173	+0.407 -0.406
600 - 640	325.046	0.198	57.463	0.470	0.177	+0.427 -0.426
640 - 680	205.727	0.248	37.282	0.583	0.181	+0.529 -0.527
680 - 720	133.674	0.308	24.859	0.714	0.186	+0.646 -0.643
720 - 760	87.911	0.380	16.560	0.875	0.188	+0.791 -0.786
760 - 800	58.657	0.465	11.056	1.071	0.188	+0.968 -0.961
800 - 850	38.106	0.516	7.318	1.178	0.192	+1.063 -1.054
850 - 900	23.587	0.656	4.600	1.485	0.195	+1.339 -1.326
900 - 950	15.130	0.819	2.896	1.872	0.191	+1.694 -1.672
950 - 1000	9.696	1.023	1.812	2.366	0.187	+2.151 -2.116
1000 - 1060	6.026	1.185	1.186	2.670	0.197	+2.414 -2.371
1060 - 1120	3.668	1.518	0.716	3.436	0.195	+3.118 -3.046
1120 - 1180	2.327	1.906	0.437	4.398	0.188	+4.024 -3.903
1180 - 1250	1.419	2.260	0.265	5.227	0.187	+4.798 -4.627
1250 - 1320	0.853	2.915	0.165	6.623	0.194	+6.080 -5.811
1320 - 1390	0.477	3.898	0.080	9.492	0.169	+8.951 -8.355
1390 - 1460	0.263	5.249	0.042	13.131	0.160	+12.619 -11.449
1460 - 1530	0.192	6.143	0.029	15.811	0.151	+15.437 -13.698
1530 - 1600	0.104	8.362	0.021	18.570	0.203	+17.571 -15.536
1600 - 1680	0.060	10.314	0.009	26.726	0.149	+27.132 -22.170

A.2 Individual Sources of Jet Energy Correction Uncertainties

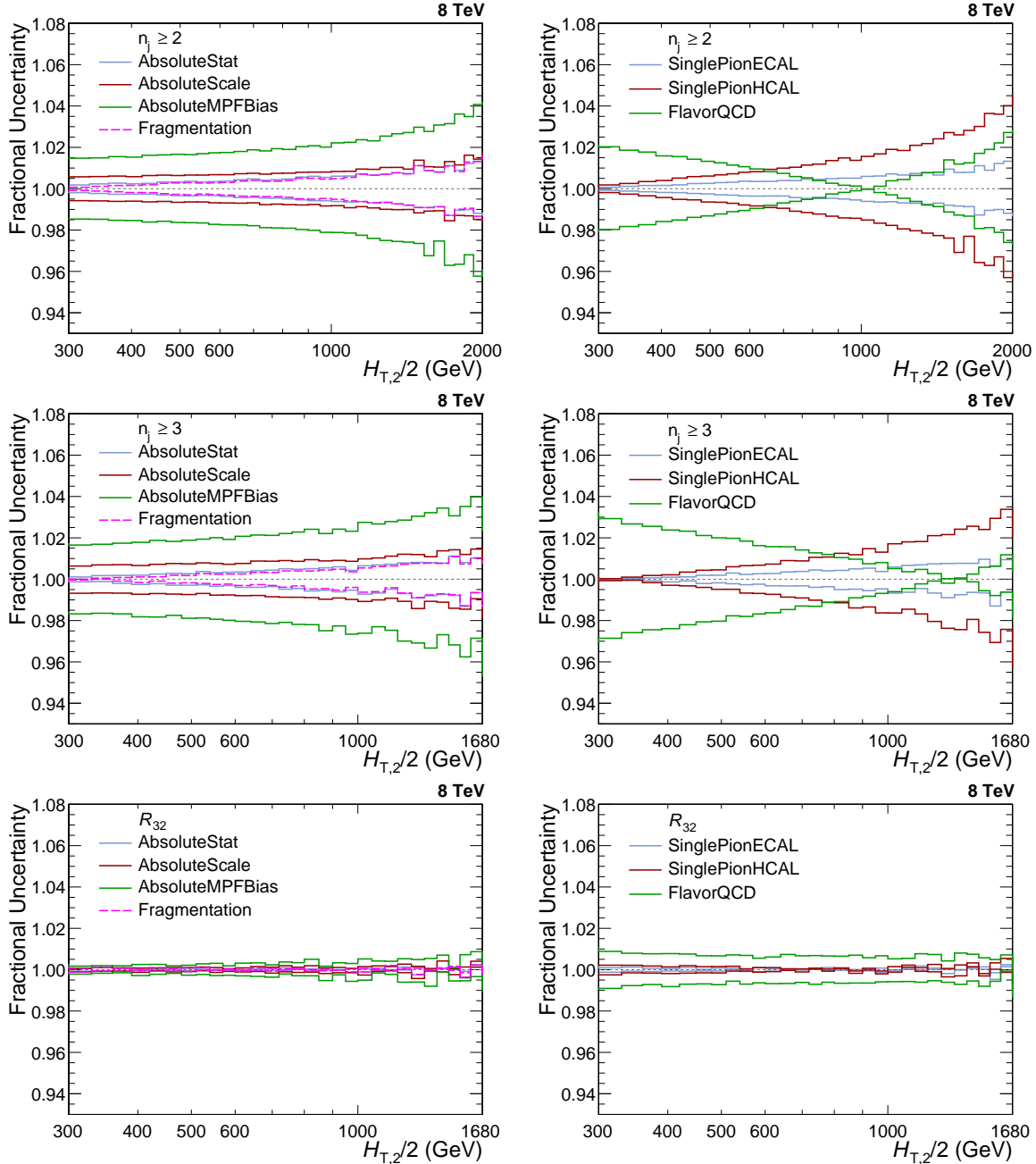


Figure A.1: The fractional jet energy correction (JEC) uncertainties from individual sources are shown for inclusive 2-jet (top) and 3-jet events cross-sections (middle); and cross-section ratio R_{32} (bottom). On left, JEC uncertainties are evaluated from AbsoluteStat (blue), AbsoluteScale (red), AbsoluteMPFBias (green) and Fragmentation (pink) sources whereas on right, these are evaluated from SinglePionECAL (blue), SinglePionHCAL (red) and FlavorQCD (green) sources.

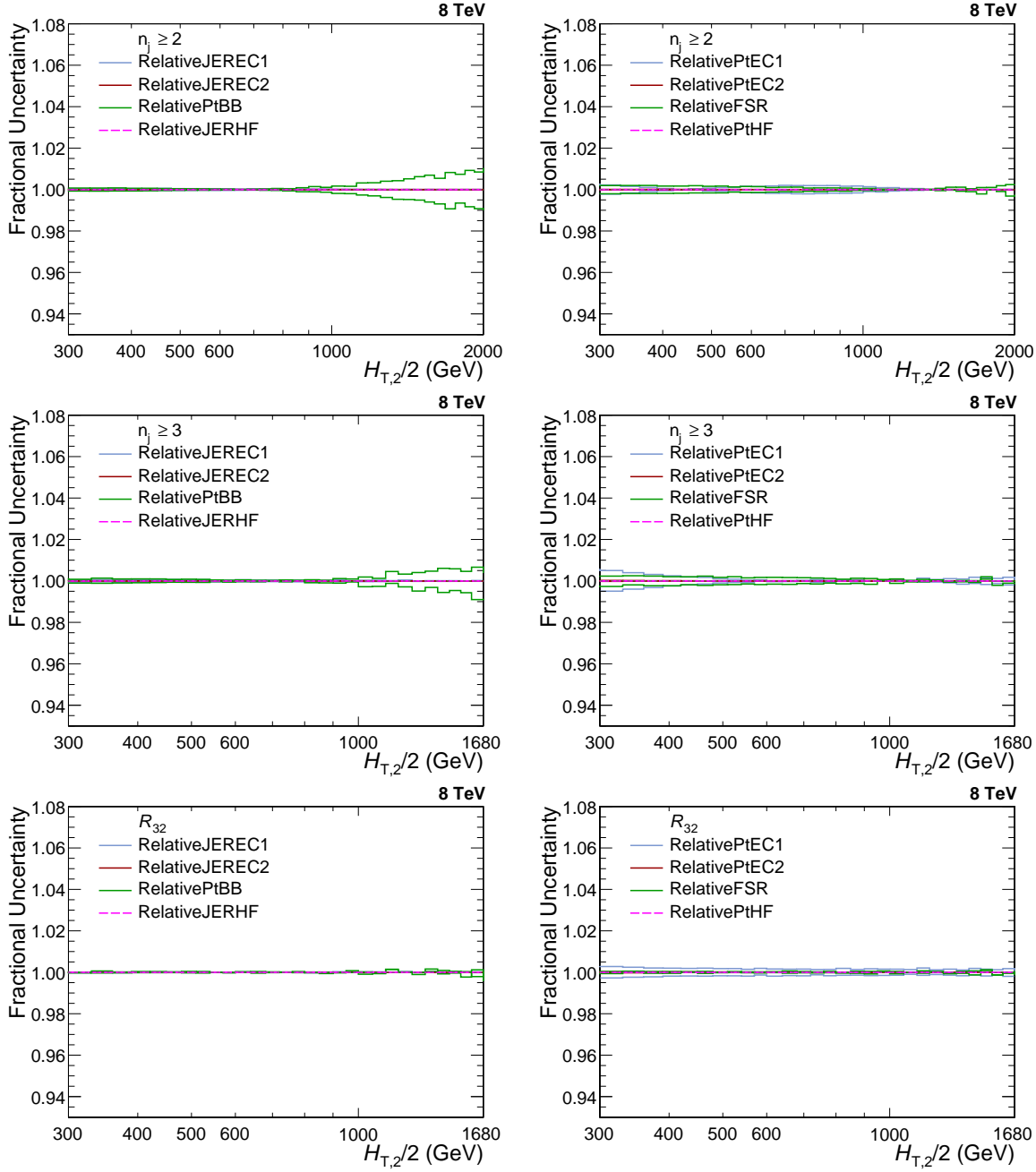


Figure A.2: The fractional jet energy correction (JEC) uncertainties from individual sources are shown for inclusive 2-jet (top) and 3-jet events cross-sections (middle); and cross-section ratio R_{32} (bottom). On left, JEC uncertainties are evaluated from RelativeJEREC1 (blue), RelativeJEREC2 (red), RelativePtBB (green) and RelativeJERHF (pink) sources whereas on right, these are evaluated from RelativePtEC1 (blue), RelativePtEC2 (red), RelativePFSR (green) and RelativePtHF (pink) sources.

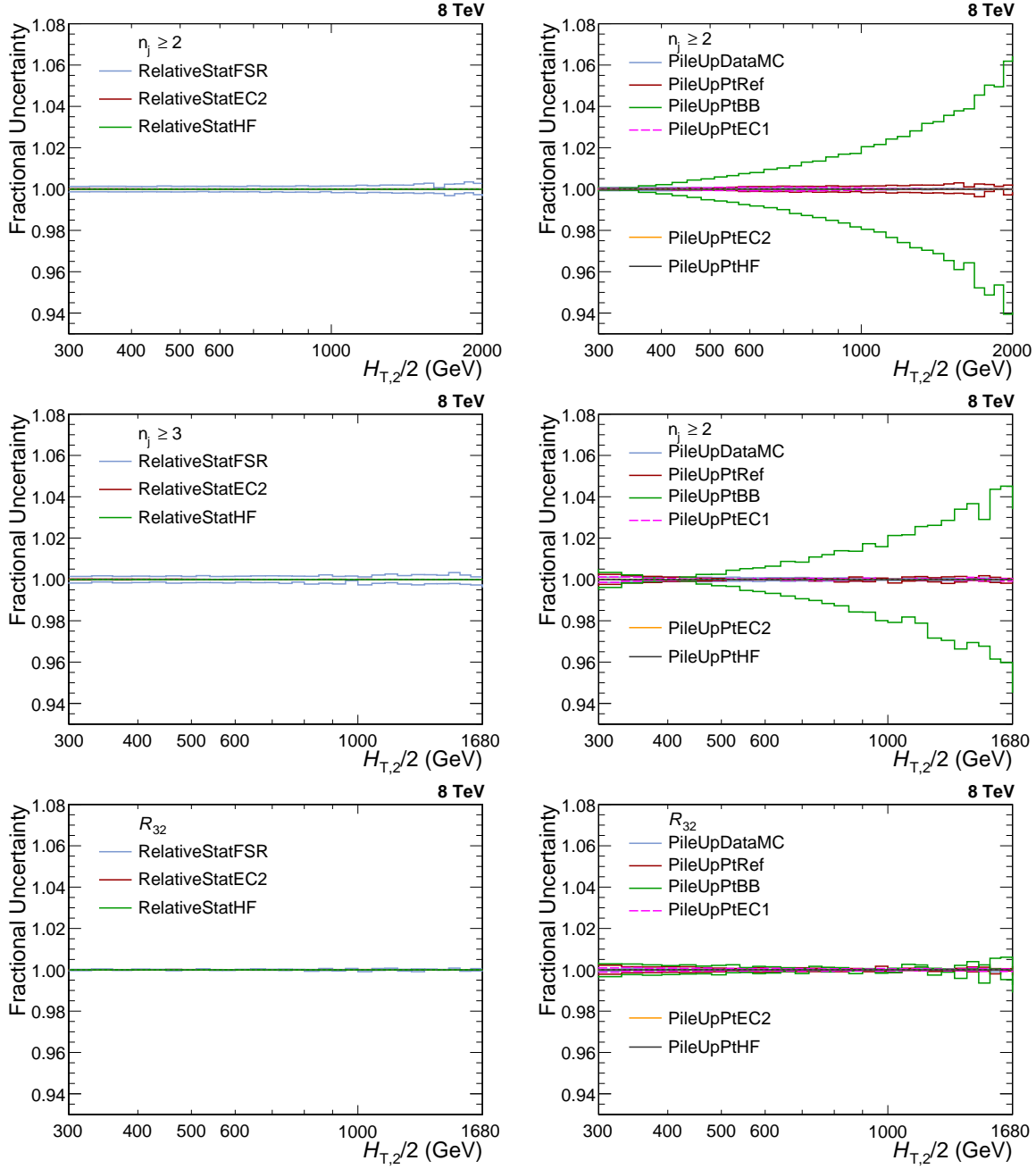


Figure A.3: The fractional jet energy correction (JEC) uncertainties from individual sources are shown for inclusive 2-jet (top) and 3-jet events cross-sections (middle); and cross-section ratio R_{32} (bottom). On left, JEC uncertainties are evaluated from RelativeStatFSR (blue), RelativeStatEC2 (red) and RelativeStatHF (green) sources whereas on right, these are evaluated from PileUpDataMC (blue), PileUpPtRef (red), PileUpPtBB (green), PileUpPtEC1 (pink), PileUpPtEC2 (orange) and PileUpPtHF (black) sources.

A.3 Experimental Uncertainties

Table A.2: Experimental uncertainties (in %), from all sources as well as the total uncertainty, affecting the cross-section measurement in each bin of $H_{T,2}/2$ for inclusive 2-jet events.

Bin	Statistical	JEC	Unfolding	Lumi	Residual	Total
300 - 330	0.242	+2.612 -2.565	+0.948 -0.928	2.6	1.0	+3.942 -3.906
330 - 360	0.258	+2.507 -2.473	+0.976 -0.969	2.6	1.0	+3.882 -3.858
360 - 390	0.202	+2.504 -2.465	+0.779 -0.783	2.6	1.0	+3.831 -3.807
390 - 420	0.193	+2.363 -2.381	+0.905 -0.904	2.6	1.0	+3.768 -3.780
420 - 450	0.084	+2.448 -2.422	+0.904 -0.895	2.6	1.0	+3.818 -3.799
450 - 480	0.096	+2.440 -2.352	+0.797 -0.795	2.6	1.0	+3.789 -3.733
480 - 510	0.107	+2.427 -2.406	+0.728 -0.715	2.6	1.0	+3.767 -3.751
510 - 540	0.128	+2.425 -2.395	+0.835 -0.862	2.6	1.0	+3.789 -3.775
540 - 570	0.154	+2.425 -2.376	+0.687 -0.674	2.6	1.0	+3.760 -3.726
570 - 600	0.180	+2.497 -2.474	+0.839 -0.827	2.6	1.0	+3.838 -3.820
600 - 640	0.209	+2.495 -2.491	+0.744 -0.743	2.6	1.0	+3.819 -3.816
640 - 680	0.264	+2.582 -2.545	+0.912 -0.912	2.6	1.0	+3.915 -3.891
680 - 720	0.320	+2.691 -2.574	+0.763 -0.756	2.6	1.0	+3.961 -3.880
720 - 760	0.387	+2.690 -2.755	+0.705 -0.712	2.6	1.0	+3.955 -4.001
760 - 800	0.465	+2.858 -2.846	+0.859 -0.846	2.6	1.0	+4.109 -4.098
800 - 850	0.548	+2.889 -2.913	+0.783 -0.787	2.6	1.0	+4.126 -4.143
850 - 900	0.698	+3.145 -3.102	+0.961 -0.958	2.6	1.0	+4.366 -4.334
900 - 950	0.847	+3.298 -3.233	+0.828 -0.829	2.6	1.0	+4.476 -4.429
950 - 1000	1.041	+3.291 -3.330	+0.895 -0.872	2.6	1.0	+4.525 -4.549
1000 - 1060	1.268	+3.598 -3.569	+0.945 -0.956	2.6	1.0	+4.817 -4.798
1060 - 1120	1.611	+3.759 -3.756	+0.970 -0.967	2.6	1.0	+5.043 -5.040
1120 - 1180	1.985	+4.154 -4.053	+1.089 -1.080	2.6	1.0	+5.490 -5.413
1180 - 1250	2.406	+4.251 -4.313	+1.062 -1.070	2.6	1.0	+5.722 -5.770
1250 - 1320	3.101	+4.696 -4.624	+1.151 -1.144	2.6	1.0	+6.384 -6.330
1320 - 1390	4.157	+4.934 -4.979	+1.343 -1.341	2.6	1.0	+7.155 -7.186
1390 - 1460	5.270	+5.148 -5.104	+1.185 -1.177	2.6	1.0	+7.965 -7.936
1460 - 1530	6.360	+5.890 -5.652	+1.405 -1.406	2.6	1.0	+9.213 -9.063
1530 - 1600	8.183	+5.924 -6.311	+1.598 -1.590	2.6	1.0	+10.601 -10.821
1600 - 1680	10.630	+5.969 -5.655	+1.607 -1.592	2.6	1.0	+12.608 -12.461
1680 - 1760	13.864	+7.245 -7.603	+1.821 -1.839	2.6	1.0	+15.993 -16.161
1760 - 1840	18.192	+7.781 -7.820	+1.902 -1.906	2.6	1.0	+20.071 -20.087
1840 - 1920	22.612	+7.647 -7.537	+1.588 -1.590	2.6	1.0	+24.085 -24.050
1920 - 2000	29.530	+9.199 -9.469	+1.511 -1.505	2.6	1.0	+31.092 -31.172

Table A.3: Experimental uncertainties (in %), from all sources as well as the total uncertainty, affecting the cross-section measurement in each bin of $H_{T,2}/2$ for inclusive 3-jet events.

Bin	Statistical	JEC	Unfolding	Lumi	Residual	Total
300 - 330	0.796	+3.503 -3.475	+0.564 -0.552	2.6	1.0	+4.581 -4.558
330 - 360	0.781	+3.303 -3.186	+0.640 -0.633	2.6	1.0	+4.437 -4.350
360 - 390	0.583	+3.221 -3.094	+0.490 -0.496	2.6	1.0	+4.326 -4.233
390 - 420	0.531	+3.092 -3.149	+0.584 -0.584	2.6	1.0	+4.236 -4.278
420 - 450	0.224	+3.125 -2.996	+0.604 -0.592	2.6	1.0	+4.236 -4.140
450 - 480	0.248	+2.984 -2.890	+0.531 -0.528	2.6	1.0	+4.124 -4.056
480 - 510	0.269	+2.937 -2.963	+0.511 -0.512	2.6	1.0	+4.089 -4.108
510 - 540	0.318	+3.021 -2.797	+0.592 -0.612	2.6	1.0	+4.164 -4.007
540 - 570	0.375	+2.999 -2.935	+0.506 -0.500	2.6	1.0	+4.141 -4.094
570 - 600	0.434	+2.824 -2.906	+0.646 -0.620	2.6	1.0	+4.042 -4.096
600 - 640	0.497	+2.952 -2.956	+0.598 -0.604	2.6	1.0	+4.133 -4.136
640 - 680	0.617	+3.111 -3.001	+0.777 -0.786	2.6	1.0	+4.292 -4.215
680 - 720	0.739	+3.067 -2.984	+0.642 -0.611	2.6	1.0	+4.257 -4.194
720 - 760	0.895	+3.185 -3.111	+0.595 -0.607	2.6	1.0	+4.366 -4.313
760 - 800	1.068	+3.231 -3.166	+0.763 -0.774	2.6	1.0	+4.464 -4.419
800 - 850	1.250	+3.427 -3.295	+0.674 -0.687	2.6	1.0	+4.639 -4.544
850 - 900	1.578	+3.364 -3.540	+0.903 -0.898	2.6	1.0	+4.731 -4.857
900 - 950	1.961	+3.594 -3.524	+0.792 -0.793	2.6	1.0	+5.015 -4.965
950 - 1000	2.420	+3.603 -3.783	+0.846 -0.843	2.6	1.0	+5.226 -5.351
1000 - 1060	2.844	+4.164 -4.116	+0.916 -0.940	2.6	1.0	+5.834 -5.803
1060 - 1120	3.647	+4.038 -3.815	+0.963 -0.957	2.6	1.0	+6.188 -6.044
1120 - 1180	4.607	+4.278 -4.183	+1.084 -1.087	2.6	1.0	+6.961 -6.904
1180 - 1250	5.532	+4.894 -4.771	+1.074 -1.069	2.6	1.0	+7.967 -7.891
1250 - 1320	7.141	+5.144 -5.273	+1.222 -1.217	2.6	1.0	+9.312 -9.383
1320 - 1390	10.207	+5.542 -5.642	+1.414 -1.428	2.6	1.0	+12.027 -12.076
1390 - 1460	13.831	+5.630 -5.265	+1.257 -1.256	2.6	1.0	+15.242 -15.111
1460 - 1530	15.578	+5.576 -5.491	+1.546 -1.551	2.6	1.0	+16.850 -16.822
1530 - 1600	18.729	+6.409 -7.019	+1.718 -1.716	2.6	1.0	+20.063 -20.266
1600 - 1680	26.465	+7.017 -6.255	+1.775 -1.765	2.6	1.0	+27.578 -27.393

Table A.4: Experimental uncertainties (in %), from all sources as well as the total uncertainty, affecting the measurement of cross-section ratio R_{32} , in each bin of $H_{T,2}/2$.

Bin	Statistical	JEC	Unfolding	Total
300 - 330	0.741	+1.059 -1.097	+0.754 -0.751	+1.496 -1.522
330 - 360	0.587	+0.954 -0.923	+0.685 -0.689	+1.313 -1.292
360 - 390	0.519	+0.902 -0.855	+0.594 -0.593	+1.199 -1.163
390 - 420	0.236	+0.907 -0.952	+0.439 -0.438	+1.035 -1.074
420 - 450	0.192	+0.900 -0.835	+0.360 -0.361	+0.988 -0.930
450 - 480	0.209	+0.788 -0.802	+0.307 -0.308	+0.872 -0.884
480 - 510	0.245	+0.795 -0.867	+0.254 -0.235	+0.870 -0.931
510 - 540	0.287	+0.852 -0.682	+0.264 -0.268	+0.937 -0.787
540 - 570	0.326	+0.807 -0.803	+0.193 -0.189	+0.891 -0.887
570 - 600	0.397	+0.656 -0.774	+0.199 -0.219	+0.792 -0.898
600 - 640	0.447	+0.763 -0.797	+0.150 -0.154	+0.897 -0.926
640 - 680	0.573	+0.861 -0.781	+0.153 -0.140	+1.045 -0.979
680 - 720	0.663	+0.766 -0.787	+0.147 -0.164	+1.024 -1.042
720 - 760	0.774	+0.842 -0.769	+0.118 -0.118	+1.149 -1.097
760 - 800	0.970	+0.800 -0.729	+0.115 -0.096	+1.263 -1.218
800 - 850	1.116	+0.873 -0.775	+0.115 -0.104	+1.422 -1.363
850 - 900	1.436	+0.770 -0.896	+0.069 -0.069	+1.631 -1.694
900 - 950	1.716	+0.704 -0.752	+0.050 -0.051	+1.855 -1.874
950 - 1000	2.156	+0.824 -0.897	+0.089 -0.045	+2.310 -2.336
1000 - 1060	2.554	+0.812 -0.870	+0.045 -0.040	+2.680 -2.698
1060 - 1120	3.244	+0.792 -0.658	+0.018 -0.027	+3.339 -3.310
1120 - 1180	4.121	+0.985 -0.757	+0.025 -0.043	+4.237 -4.191
1180 - 1250	4.990	+1.031 -0.848	+0.023 -0.041	+5.095 -5.062
1250 - 1320	6.456	+0.750 -1.087	+0.079 -0.079	+6.500 -6.548
1320 - 1390	8.990	+1.112 -1.144	+0.080 -0.099	+9.059 -9.063
1390 - 1460	12.699	+1.157 -0.815	+0.076 -0.078	+12.751 -12.725
1460 - 1530	13.926	+0.768 -1.235	+0.143 -0.145	+13.948 -13.981
1530 - 1600	16.903	+1.050 -1.258	+0.120 -0.127	+16.936 -16.950
1600 - 1680	28.070	+1.471 -0.859	+0.178 -0.177	+28.109 -28.084

A.4 Theoretical Uncertainties

Table A.5: Theoretical uncertainties (in %) calculating using CT10-NLO PDF set from all sources as well as the total uncertainty, affecting the cross-section measurement in each bin of $H_{T,2}/2$ for inclusive 2-jet events.

Bin	Scale	PDF	NP	Total
300 - 330	+0.942 -6.149	+3.566 -3.090	0.825	+3.780 -6.931
330 - 360	+1.035 -6.289	+3.906 -3.342	0.736	+4.107 -7.159
360 - 390	+1.159 -6.438	+4.232 -3.573	0.696	+4.442 -7.396
390 - 420	+1.220 -6.536	+4.551 -3.794	0.723	+4.767 -7.592
420 - 450	+1.326 -6.660	+4.857 -3.997	0.745	+5.089 -7.802
450 - 480	+1.421 -6.776	+5.153 -4.186	0.765	+5.399 -8.001
480 - 510	+1.512 -6.888	+5.444 -4.365	0.782	+5.704 -8.192
510 - 540	+1.566 -6.967	+5.721 -4.527	0.797	+5.984 -8.347
540 - 570	+1.666 -7.082	+6.000 -4.682	0.810	+6.279 -8.528
570 - 600	+1.731 -7.172	+6.269 -4.825	0.822	+6.555 -8.683
600 - 640	+1.805 -7.271	+6.597 -4.979	0.833	+6.890 -8.852
640 - 680	+1.930 -7.416	+6.978 -5.143	0.845	+7.289 -9.064
680 - 720	+2.007 -7.527	+7.364 -5.295	0.856	+7.680 -9.243
720 - 760	+2.113 -7.663	+7.749 -5.437	0.865	+8.078 -9.436
760 - 800	+2.196 -7.781	+8.140 -5.569	0.873	+8.476 -9.609
800 - 850	+2.323 -7.945	+8.573 -5.706	0.881	+8.926 -9.822
850 - 900	+2.389 -8.062	+9.082 -5.863	0.889	+9.433 -10.008
900 - 950	+2.499 -8.227	+9.600 -6.018	0.896	+9.961 -10.232
950 - 1000	+2.631 -8.402	+10.134 -6.166	0.902	+10.509 -10.460
1000 - 1060	+2.738 -8.569	+10.747 -6.343	0.908	+11.127 -10.700
1060 - 1120	+2.853 -8.751	+11.431 -6.526	0.914	+11.817 -10.955
1120 - 1180	+2.992 -8.970	+12.183 -6.727	0.919	+12.579 -11.250
1180 - 1250	+3.135 -9.194	+13.019 -6.944	0.924	+13.423 -11.558
1250 - 1320	+3.324 -9.469	+14.004 -7.189	0.929	+14.423 -11.925
1320 - 1390	+3.434 -9.677	+15.080 -7.444	0.933	+15.494 -12.244
1390 - 1460	+3.629 -9.976	+16.223 -7.700	0.937	+16.650 -12.637
1460 - 1530	+3.760 -10.224	+17.505 -7.980	0.940	+17.929 -13.004
1530 - 1600	+3.894 -10.471	+18.891 -8.258	0.943	+19.311 -13.368
1600 - 1680	+4.107 -10.813	+20.496 -8.560	0.946	+20.925 -13.824
1680 - 1760	+4.421 -11.101	+22.481 -8.905	0.949	+22.931 -14.263
1760 - 1840	+4.921 -11.461	+24.654 -9.251	0.951	+25.158 -14.760
1840 - 1920	+5.404 -11.813	+27.143 -9.607	0.953	+27.692 -15.256
1920 - 2000	+5.867 -12.154	+29.986 -9.973	0.955	+30.570 -15.751

Table A.6: Theoretical uncertainties (in %) calculating using CT10-NLO PDF set from all sources as well as the total uncertainty, affecting the cross-section measurement in each bin of $H_{T,2}/2$ for inclusive 3-jet events.

Bin	Scale	PDF	NP	Total
300 - 330	+0.539 -8.294	+5.716 -4.657	1.692	+5.986 -9.662
330 - 360	+0.550 -8.577	+5.977 -4.779	1.516	+6.191 -9.935
360 - 390	+0.599 -8.709	+6.187 -4.987	1.363	+6.363 -10.128
390 - 420	+0.719 -8.948	+6.751 -5.223	1.228	+6.900 -10.433
420 - 450	+0.799 -9.145	+7.031 -5.395	1.110	+7.162 -10.676
450 - 480	+0.847 -9.247	+7.404 -5.578	1.005	+7.520 -10.845
480 - 510	+0.847 -9.294	+7.837 -5.717	0.937	+7.938 -10.951
510 - 540	+0.922 -9.436	+8.198 -5.884	0.921	+8.301 -11.158
540 - 570	+0.974 -9.566	+8.529 -6.000	0.904	+8.632 -11.328
570 - 600	+1.086 -9.786	+8.970 -6.156	0.886	+9.079 -11.595
600 - 640	+1.107 -9.852	+9.402 -6.297	0.866	+9.506 -11.724
640 - 680	+1.278 -10.101	+10.310 -6.526	0.842	+10.423 -12.055
680 - 720	+1.384 -10.342	+9.682 -6.618	0.820	+9.815 -12.305
720 - 760	+1.415 -10.404	+11.051 -6.826	0.798	+11.170 -12.469
760 - 800	+1.547 -10.615	+11.565 -7.009	0.777	+11.694 -12.744
800 - 850	+1.679 -10.804	+12.242 -7.185	0.755	+12.379 -12.997
850 - 900	+2.085 -11.134	+13.097 -7.461	0.731	+13.282 -13.422
900 - 950	+2.475 -11.432	+13.889 -7.703	0.709	+14.125 -13.804
950 - 1000	+2.655 -11.608	+14.614 -7.915	0.688	+14.869 -14.066
1000 - 1060	+3.025 -11.926	+15.576 -8.173	0.667	+15.881 -14.473
1060 - 1120	+3.299 -12.189	+14.250 -8.441	0.645	+14.641 -14.840
1120 - 1180	+3.741 -12.584	+17.984 -8.787	0.625	+18.380 -15.361
1180 - 1250	+3.969 -12.843	+19.324 -9.127	0.625	+19.737 -15.768
1250 - 1320	+4.663 -13.452	+21.246 -9.517	0.642	+21.761 -16.490
1320 - 1390	+4.878 -13.702	+22.884 -9.899	0.657	+23.407 -16.916
1390 - 1460	+5.242 -14.095	+24.854 -10.332	0.670	+25.410 -17.489
1460 - 1530	+5.582 -14.464	+27.170 -10.733	0.682	+27.746 -18.024
1530 - 1600	+6.003 -14.907	+29.741 -11.165	0.692	+30.349 -18.637
1600 - 1680	+6.503 -15.418	+32.855 -11.617	0.702	+33.500 -19.317

Table A.7: Theoretical uncertainties (in %) calculating using CT10-NLO PDF set from all sources as well as the total uncertainty, affecting the measurement of cross-section ratio R_{32} , in each bin of $H_{T,2}/2$.

Bin	Scale	PDF	NP	Total
300 - 330	+0.038 -7.203	+2.458 -3.463	0.822	+2.592 -8.035
330 - 360	+0.027 -6.626	+2.317 -3.378	0.734	+2.431 -7.474
360 - 390	+0.024 -6.449	+2.149 -3.367	0.656	+2.247 -7.304
390 - 420	+0.084 -5.894	+2.411 -3.383	0.586	+2.482 -6.821
420 - 450	+0.113 -5.532	+2.345 -3.362	0.523	+2.405 -6.494
450 - 480	+0.109 -5.409	+2.390 -3.357	0.467	+2.438 -6.383
480 - 510	+0.073 -5.442	+2.506 -3.327	0.416	+2.541 -6.392
510 - 540	+0.107 -5.168	+2.559 -3.326	0.371	+2.588 -6.157
540 - 570	+0.112 -5.010	+2.586 -3.292	0.330	+2.609 -6.004
570 - 600	+0.163 -4.576	+2.729 -3.292	0.292	+2.750 -5.645
600 - 640	+0.146 -4.565	+2.824 -3.270	0.253	+2.839 -5.621
640 - 680	+0.198 -4.163	+3.368 -3.298	0.236	+3.382 -5.316
680 - 720	+0.155 -3.754	+2.352 -3.247	0.227	+2.368 -4.968
720 - 760	+0.196 -3.842	+3.267 -3.268	0.219	+3.280 -5.049
760 - 800	+0.126 -3.523	+3.366 -3.272	0.212	+3.375 -4.813
800 - 850	+0.110 -3.368	+3.596 -3.261	0.206	+3.604 -4.693
850 - 900	+0.048 -3.351	+3.909 -3.309	0.200	+3.915 -4.714
900 - 950	+0.116 -3.504	+4.148 -3.334	0.196	+4.154 -4.841
950 - 1000	+0.127 -3.511	+4.300 -3.335	0.192	+4.306 -4.846
1000 - 1060	+0.282 -3.683	+4.604 -3.357	0.204	+4.617 -4.988
1060 - 1120	+0.436 -3.779	+3.079 -3.375	0.224	+3.118 -5.071
1120 - 1180	+0.732 -3.982	+5.430 -3.452	0.241	+5.485 -5.276
1180 - 1250	+0.813 -4.031	+5.835 -3.511	0.258	+5.897 -5.352
1250 - 1320	+1.303 -4.414	+6.626 -3.591	0.275	+6.759 -5.697
1320 - 1390	+1.403 -4.471	+7.036 -3.659	0.290	+7.180 -5.785
1390 - 1460	+1.564 -4.590	+7.657 -3.778	0.304	+7.822 -5.953
1460 - 1530	+1.765 -4.738	+8.438 -3.853	0.316	+8.626 -6.115
1530 - 1600	+2.040 -4.972	+9.306 -3.962	0.328	+9.532 -6.366
1600 - 1680	+2.313 -5.179	+10.381 -4.075	0.339	+10.641 -6.599

Bibliography

- [1] J. Alwall, M. Herquet, F. Maltoni, O. Mattelaer, and T. Stelzer, “MadGraph 5 : Going Beyond,” *JHEP*, vol. 06, p. 128, 2011.
- [2] T. Sjostrand, S. Mrenna, and P. Z. Skands, “PYTHIA 6.4 Physics and Manual,” *JHEP*, vol. 05, p. 026, 2006.
- [3] J. Alwall *et al.*, “A Standard format for Les Houches event files,” *Comput. Phys. Commun.*, vol. 176, pp. 300–304, 2007.
- [4] C. J. Clopper and E. S. Pearson, “The use of confidence or fiducial limits illustrated in the case of the binomial,” *Biometrika*, vol. 26, no. 4, pp. 404–413, 1934.
- [5] C. Collaboration, “Jet Performance in pp Collisions at 7 TeV,” 2010.
- [6] C. Collaboration, “Jet Identification at 8 TeV.” <https://twiki.cern.ch/twiki/bin/viewauth/CMS/JetID>, 2012. (accessed on 2017-10-31).
- [7] C. Collaboration, “Jet Energy Resolution at 8 TeV.” <https://twiki.cern.ch/twiki/bin/viewauth/CMS/JetResolution>, 2012. (accessed on 2016-01-22).
- [8] C. Collaboration, “Jet Energy Resolution in CMS at $\sqrt{s}=7$ TeV,” 2011.
- [9] G. D’Agostini, “A Multidimensional unfolding method based on Bayes’ theorem,” *Nucl. Instrum. Meth.*, vol. A362, pp. 487–498, 1995.

-
- [10] G. D’Agostini, “Improved iterative Bayesian unfolding,” 2010.
- [11] T. Adye, “Unfolding algorithms and tests using RooUnfold,” in *Proceedings, PHYSTAT 2011 Workshop on Statistical Issues Related to Discovery Claims in Search Experiments and Unfolding, CERN, Geneva, Switzerland 17-20 January 2011*, (Geneva), pp. 313–318, CERN, CERN, 2011.
- [12] S. Chatrchyan *et al.*, “Measurement of the Inclusive Jet Cross Section in pp Collisions at $\sqrt{s} = 7$ TeV,” *Phys. Rev. Lett.*, vol. 107, p. 132001, 2011.
- [13] V. Khachatryan *et al.*, “Jet energy scale and resolution in the CMS experiment in pp collisions at 8 TeV,” *JINST*, vol. 12, no. 02, p. P02014, 2017.
- [14] C. Collaboration, “Jet energy scale uncertainty sources.” <https://twiki.cern.ch/twiki/bin/viewauth/CMS/JECUncertaintySources>, 2012. (accessed on 2017-10-31).
- [15] C. Collaboration, “CMS Luminosity Based on Pixel Cluster Counting - Summer 2013 Update,” 2013.
- [16] S. Chatrchyan *et al.*, “Measurements of differential jet cross sections in proton-proton collisions at $\sqrt{s} = 7$ TeV with the CMS detector,” *Phys. Rev.*, vol. D87, no. 11, p. 112002, 2013. [Erratum: *Phys. Rev.* D87, no. 11, 119902 (2013)].
- [17] V. Khachatryan *et al.*, “Measurement and QCD analysis of double-differential inclusive jet cross sections in pp collisions at $\sqrt{s} = 8$ TeV and cross section ratios to 2.76 and 7 TeV,” *JHEP*, vol. 03, p. 156, 2017.
- [18] Z. Nagy, “Three jet cross-sections in hadron hadron collisions at next-to-leading order,” *Phys. Rev. Lett.*, vol. 88, p. 122003, 2002.
- [19] Z. Nagy, “Next-to-leading order calculation of three jet observables in hadron hadron collision,” *Phys. Rev.*, vol. D68, p. 094002, 2003.

-
- [20] T. Kluge, K. Rabbertz, and M. Wobisch, “FastNLO: Fast pQCD calculations for PDF fits,” in *Deep inelastic scattering. Proceedings, 14th International Workshop, DIS 2006, Tsukuba, Japan, April 20-24, 2006*, pp. 483–486, 2006.
- [21] D. Britzger, K. Rabbertz, F. Stober, and M. Wobisch, “New features in version 2 of the fastNLO project,” in *Proceedings, 20th International Workshop on Deep-Inelastic Scattering and Related Subjects (DIS 2012): Bonn, Germany, March 26-30, 2012*, pp. 217–221, 2012.
- [22] M. R. Whalley, D. Bourilkov, and R. C. Group, “The Les Houches accord PDFs (LHAPDF) and LHAGLUE,” in *HERA and the LHC: A Workshop on the implications of HERA for LHC physics. Proceedings, Part B*, pp. 575–581, 2005.
- [23] A. Buckley, J. Ferrando, S. Lloyd, K. Nordström, B. Page, M. Rüfenacht, M. Schönherr, and G. Watt, “LHAPDF6: parton density access in the LHC precision era,” *Eur. Phys. J.*, vol. C75, p. 132, 2015.
- [24] G. Aad *et al.*, “Measurement of the inclusive jet cross section in pp collisions at $\sqrt{s}=2.76$ TeV and comparison to the inclusive jet cross section at $\sqrt{s}=7$ TeV using the ATLAS detector,” *Eur. Phys. J.*, vol. C73, no. 8, p. 2509, 2013.
- [25] G. Aad *et al.*, “Measurement of the inclusive jet cross-section in proton-proton collisions at $\sqrt{s} = 7$ TeV using 4.5 fb^{-1} of data with the ATLAS detector,” *JHEP*, vol. 02, p. 153, 2015. [Erratum: JHEP09,141(2015)].
- [26] V. Khachatryan *et al.*, “Measurement of the inclusive 3-jet production differential cross section in proton–proton collisions at 7 TeV and determination of the strong coupling constant in the TeV range,” *Eur. Phys. J.*, vol. C75, no. 5, p. 186, 2015.
- [27] V. Khachatryan *et al.*, “Measurement of the inclusive jet cross section in pp collisions at $\sqrt{s} = 2.76$ TeV,” *Eur. Phys. J.*, vol. C76, no. 5, p. 265, 2016.

-
- [28] S. Alekhin, J. Blumlein, and S. Moch, “Parton Distribution Functions and Benchmark Cross Sections at NNLO,” *Phys. Rev.*, vol. D86, p. 054009, 2012.
- [29] H.-L. Lai, M. Guzzi, J. Huston, Z. Li, P. M. Nadolsky, J. Pumplin, and C. P. Yuan, “New parton distributions for collider physics,” *Phys. Rev.*, vol. D82, p. 074024, 2010.
- [30] A. D. Martin, W. J. Stirling, R. S. Thorne, and G. Watt, “Parton distributions for the LHC,” *Eur. Phys. J.*, vol. C63, pp. 189–285, 2009.
- [31] A. D. Martin, W. J. Stirling, R. S. Thorne, and G. Watt, “Uncertainties on $\alpha(S)$ in global PDF analyses and implications for predicted hadronic cross sections,” *Eur. Phys. J.*, vol. C64, pp. 653–680, 2009.
- [32] R. D. Ball *et al.*, “Parton distributions with LHC data,” *Nucl. Phys.*, vol. B867, pp. 244–289, 2013.
- [33] S. Dulat, T.-J. Hou, J. Gao, M. Guzzi, J. Huston, P. Nadolsky, J. Pumplin, C. Schmidt, D. Stump, and C. P. Yuan, “New parton distribution functions from a global analysis of quantum chromodynamics,” *Phys. Rev.*, vol. D93, no. 3, p. 033006, 2016.
- [34] H. Abramowicz *et al.*, “Combination of measurements of inclusive deep inelastic $e^\pm p$ scattering cross sections and QCD analysis of HERA data,” *Eur. Phys. J.*, vol. C75, no. 12, p. 580, 2015.
- [35] L. A. Harland-Lang, A. D. Martin, P. Motylinski, and R. S. Thorne, “Parton distributions in the LHC era: MMHT 2014 PDFs,” *Eur. Phys. J.*, vol. C75, no. 5, p. 204, 2015.
- [36] R. D. Ball *et al.*, “Parton distributions for the LHC Run II,” *JHEP*, vol. 04, p. 040, 2015.

-
- [37] M. Bahr *et al.*, “Herwig++ Physics and Manual,” *Eur. Phys. J.*, vol. C58, pp. 639–707, 2008.
- [38] P. Nason, “A New method for combining NLO QCD with shower Monte Carlo algorithms,” *JHEP*, vol. 11, p. 040, 2004.
- [39] S. Frixione, P. Nason, and C. Oleari, “Matching NLO QCD computations with Parton Shower simulations: the POWHEG method,” *JHEP*, vol. 11, p. 070, 2007.
- [40] S. Alioli, K. Hamilton, P. Nason, C. Oleari, and E. Re, “Jet pair production in POWHEG,” *JHEP*, vol. 04, p. 081, 2011.
- [41] V. Khachatryan *et al.*, “Event generator tunes obtained from underlying event and multiparton scattering measurements,” *Eur. Phys. J.*, vol. C76, no. 3, p. 155, 2016.
- [42] W. Hollik *et al.*, “Electroweak physics,” *Acta Phys. Polon.*, vol. B35, pp. 2533–2555, 2004.
- [43] S. Dittmaier, A. Huss, and C. Speckner, “Weak radiative corrections to dijet production at hadron colliders,” *JHEP*, vol. 11, p. 095, 2012.
- [44] J. Pumplin, D. R. Stump, J. Huston, H. L. Lai, P. M. Nadolsky, and W. K. Tung, “New generation of parton distributions with uncertainties from global QCD analysis,” *JHEP*, vol. 07, p. 012, 2002.
- [45] S. Chatrchyan *et al.*, “Measurement of the ratio of the inclusive 3-jet cross section to the inclusive 2-jet cross section in pp collisions at $\sqrt{s} = 7$ TeV and first determination of the strong coupling constant in the TeV range,” *Eur. Phys. J.*, vol. C73, no. 10, p. 2604, 2013.
- [46] S. Chatrchyan *et al.*, “Determination of the top-quark pole mass and strong coupling constant from the t t-bar production cross section in pp collisions at

- $\sqrt{s} = 7$ TeV,” *Phys. Lett.*, vol. B728, pp. 496–517, 2014. [Erratum: *Phys. Lett.*B738,526(2014)].
- [47] V. Khachatryan *et al.*, “Constraints on parton distribution functions and extraction of the strong coupling constant from the inclusive jet cross section in pp collisions at $\sqrt{s} = 7$ TeV,” *Eur. Phys. J.*, vol. C75, no. 6, p. 288, 2015.
- [48] G. Aad *et al.*, “Measurement of transverse energy-energy correlations in multi-jet events in pp collisions at $\sqrt{s} = 7$ TeV using the ATLAS detector and determination of the strong coupling constant $\alpha_s(m_Z)$,” *Phys. Lett.*, vol. B750, pp. 427–447, 2015.
- [49] V. M. Abazov *et al.*, “Determination of the strong coupling constant from the inclusive jet cross section in $p\bar{p}$ collisions at $\sqrt{s}=1.96$ TeV,” *Phys. Rev.*, vol. D80, p. 111107, 2009.
- [50] V. M. Abazov *et al.*, “Measurement of angular correlations of jets at $\sqrt{s} = 1.96$ TeV and determination of the strong coupling at high momentum transfers,” *Phys. Lett.*, vol. B718, pp. 56–63, 2012.
- [51] V. Andreev *et al.*, “Measurement of multijet production in ep collisions at high Q^2 and determination of the strong coupling α_s ,” *Eur. Phys. J.*, vol. C75, no. 2, p. 65, 2015.
- [52] V. Andreev *et al.*, “Measurement of Jet Production Cross Sections in Deep-inelastic ep Scattering at HERA,” *Eur. Phys. J.*, vol. C77, no. 4, p. 215, 2017.
- [53] H. Abramowicz *et al.*, “Inclusive-jet photoproduction at HERA and determination of alphas,” *Nucl. Phys.*, vol. B864, pp. 1–37, 2012.
- [54] T. Affolder *et al.*, “Measurement of the strong coupling constant from inclusive jet production at the Tevatron $p\bar{p}$ collider,” *Phys. Rev. Lett.*, vol. 88, p. 042001, 2002.

- [55] R. D. Ball, L. Del Debbio, S. Forte, A. Guffanti, J. I. Latorre, J. Rojo, and M. Ubiali, “A first unbiased global NLO determination of parton distributions and their uncertainties,” *Nucl. Phys.*, vol. B838, pp. 136–206, 2010.
- [56] K. G. Chetyrkin, J. H. Kuhn, and M. Steinhauser, “RunDec: A Mathematica package for running and decoupling of the strong coupling and quark masses,” *Comput. Phys. Commun.*, vol. 133, pp. 43–65, 2000.
- [57] B. Schmidt and M. Steinhauser, “CRunDec: a C++ package for running and decoupling of the strong coupling and quark masses,” *Comput. Phys. Commun.*, vol. 183, pp. 1845–1848, 2012.
- [58] C. Patrignani *et al.*, “Review of Particle Physics,” *Chin. Phys.*, vol. C40, no. 10, p. 100001, 2016.

*Selected
Reprints*

